SURFACE PREPARATION, PASSIVATION AND PATTERNING TECHNIQUES USED IN SILICON BASED HETEROJUNCTION SOLAR CELLS

A THESIS SUBMITTED TO
THE GRADUATE SCHOOL OF NATURAL AND APPLIED SCIENCES
OF
MIDDLE EAST TECHNICAL UNIVERSITY

BY

ERGİ DÖNERÇARK

IN PARTIAL FULFILLMENT OF THE REQUIREMENTS
FOR
THE DEGREE OF MASTER OF SCIENCE
IN
PHYSICS

JANUARY 2017

Approval of the Thesis:

SURFACE PREPARATION, PASSIVATION AND PATTERNING TECHNIQUES USED IN SILICON BASED HETEROJUNCTION SOLAR CELLS

submitted by **ERGİ DÖNERÇARK** in partial fulfillment of the requirements for the degree of **Master of Science in Physics Department, Middle East Technical University** by,

Prof. Dr. Gülbin Dural Ünver ______________
Dean, Graduate School of **Natural and Applied Sciences**

Prof. Dr. Sadi Turgut ______________
Head of Department, **Physics Dept., METU**

Prof. Dr. Raşit Turan ______________
Supervisor, **Physics Dept., METU**

Examining Committee Members

Prof. Dr. Çiğdem Erçelebi ______________
Physics Dept., METU

Prof. Dr. Raşit Turan ______________
Physics Dept., METU

Prof. Dr. Mehmet Parlak ______________
Physics Dept., METU

Assoc. Prof. Dr. Savaş Sönmezoğlu ______________
Metallurgical and Materials Eng. Dept., KMU

Asst. Prof. Dr. Ayşe Seyhan ______________
Physics Dept., ÖHU

Date: *30.01.2017*

I hereby declare that all information in this document has been obtained and presented in accordance with academic rules and ethical conduct. I also declare that, as required by these rules and conduct, I have fully cited and referenced all material and results that are not original to this work.

Name, Lastname: Ergi DÖNERÇARK

Signature:

ABSTRACT

SURFACE PREPARATION PASSIVATION AND PATTERNING TECHNIQUES USED IN SILICON BASED HETEROJUNCTION SOLAR CELLS

Dönerçark, Ergi
MS, Department of Physics
Supervisor: Prof. Dr. Raşit Turan

January 2017, 123 pages

For silicon Heterojunction (SHJ) solar cell technology features, a thin intrinsic hydrogenated amorphous silicon (i a-Si:H) layer has inserted between the crystalline silicon and doped amorphous silicon. The state of the art SHJ solar cell structure involves low temperature depositions of a-Si:H layer by means of Plasma Enhanced Chemical Vapor Deposition (PECVD) technique. Recent developments on SHJ solar cells have been focused on increasing the passivation quality of a-Si:H layer and the formation of all metal contacts on the rear side. In this thesis, the motivation is to achieve high efficiency SHJ solar cells by improving the surface passivation properties of thin a-Si:H film together with the integration of interdigitated back contact (IBC) concept.

In this study, several surface preparation techniques including wet chemical chemistry were implemented to solar cell fabrication sequence. The wet chemical processes were optimized to reach the required surface cleanness appropriate for device applications. Additionally, the effects of the pyramid edge rounding process were investigated on the optical and electrical properties of the solar cell. Then, the deposition parameters of i a-Si:H were optimized to enhance surface passivation. Furthermore, the optimum post-annealing treatment parameters were determined to

improve the sputtering induced damages. Consequently, the highest efficiency was recorded as 12.5% and 15.8% for the samples with the cell area of 4 cm^2 and 0.9 cm^2, respectively.

In addition, a novel wet chemical etching approach for emitter patterning was utilized in the fabrication of SHJ IBC solar cell. Moreover, for the emitter etching process, the optimized wet chemical chemistry and application conditions were demonstrated in term of the passivation quality of the etched areas. The passivation quality of a-Si:H/silicon nitride (SiN_X) stack layer was also investigated as a front surface passivation and antireflection layer by combining with the etching method in SHJ IBC fabrication sequence. As a result of the successful application of the optimized process parameters, the production of 18% efficient SHJ IBC solar cells was realized without any surface texturing.

Keywords: *SHJ solar cell, a-Si:H, passivation, pyramid rounding, SHJ IBC, emitter etching*

ÖZ

SİLİSYUM TABANLI HETERO-EKLEM GÜNEŞ GÖZELERİNDE KULLANILAN YÜZEY HAZIRLAMA, PASİVASYON VE PATERN OLUŞTURMA TEKNİKLERİ

Dönerçark, Ergi

Yüksek Lisans, Fizik Bölümü

Tez Yöneticisi: Prof. Dr. Raşit Turan

Ocak 2017, 123 sayfa

Silisyum tabanlı Hetero-eklem (SHJ) güneş gözesi için, ince hidrojenize amorf silisyum katmanı Kristal silisyum katmanı ile katkılı amorf sisiyum arasına (i a-Si:H) katmanı yerleştirilmiştir. En bilinen SHJ güneş gözesi yapısı, Plazma Destekli Kimyasal Buhar Biriktirme (PECVD) tekniği ile a-Si:H katmanının düşük sıcaklıkta büyütülmesini içerir. SHJ güneş gözeleri konusundaki son çalışmalar, a-Si:H katmanının pasivasyon kalitesinin artırılması ve arka kısımda metal kontakların oluşması üzerine odaklanmaktadır. Bu tezde amaç; a-Si:H katmanının yüzey pasivasyonunu artırarak ve birbirine geçmiş arka kontak (IBC) konseptini entegre ederek, yüksek verimli SHJ güneş gözesi elde etmektir.

Bu çalışmada, ıslak kimya kimyası da dahil olmak üzere çeşitli yüzey hazırlama teknikleri, güneş gözesi üretim sırasına dahil edilmiştir. Islak kimyasal işlemler, cihaz uygulamaları için gerekli olan yüzey temizliğine ulaşmak için optimize edilmiştir. Ayrıca, piramit yuvarlama işleminin, güneş gözesinin optik ve elektriksel özellikleri üzerindeki etkileri araştırılmıştır. Ardından, i a-Si:H’ın birikim parametreleri, yüzey pasivasyonunu artırmak için optimize edilmiştir. Ayrıca, püskürtme ile oluşan hasarları iyileştirmek için optimum son tavlama işlemi parametreleri belirlenmiştir. Sonuç olarak en yüksek verimlilik, sırasıyla hücre alanı 4 cm^2 ve 0.9 cm^2 olan örnekler için %12.5 ve %15.8 olarak kaydedilmiştir.

Bunlara ek olarak, emiter modeli için yeni bir ıslak kimyasal aşındırma yaklaşımı, SHJ IBC güneş gözesi imalatında kullanılmıştır. Dahası, emiter aşındırma işlemi için, optimize edilmiş ıslak kimyasal kimya ve uygulama koşulları, aşınmış alanların pasivasyon kalitesi açısından gösterildi. a-Si:H/silisyum nitrit (SiN_x) kümesinin pasivasyon kalitesi, SHJ IBC üretim sırasındaki aşındırma yöntemiyle birleştirilerek ön yüzey pasifize edici ve yansıma önleyici katman olarak da incelenmiştir. Optimize edilmiş işlem parametrelerinin başarılı bir şekilde uygulanması sonucunda, herhangi bir yüzey yapılanması olmaksızın %18 verimliliğe sahip SHJ IBC güneş gözeleri üretimi gerçekleştirilmiştir.

Anahtar Kelimeler: *SHJ güneş gözesi, a-Si:H pasivasyonu, piramit yuvarlama, SHJ IBC, emiter aşındırma*

To My Dad

ACKNOWLEDGMENTS

“A gentleman is one who puts more into the world than he takes out”

- George Bernard Shaw -

George Bernard Shaw, Irish playwright and political activist, one said, “A gentleman is one who puts more into the world than he takes out.” During my master period in GÜNAM, I have always tried to be a gentleman. I am very happy to say that I have met, worked and made collaboration with people who are more gentleman than me. The thesis would have never existed without the help of many valuable people. Firstly, I would like to express my gratitude to my advisor Professor Raşit Turan for giving the opportunity of working with him. I will always be grateful to him for endless support, guidance and allowing me enough freedom to try, make a mistake and experiment. I would like to thank Professor Mehmet Parlak for sharing experimental knowledge and his help and advises during the master.

I would like to thank two daily supervisors; Engin Özkol and Fırat Es. I would like to start with Fırat Es who was the first daily supervisor in GÜNAM. I am grateful to him for sharing theoretical and experimental knowledge and guiding me during my first year in master. My deepest gratitude goes to Engin Özkol. In these three years, we have spent too many memorable hours on operating the tool. I am grateful to you for a nice friendship and your valuable feedbacks during the construction period of the thesis. I would like to continue with thin film group. I would like to thank Zeynep Demircioğlu for her nice friendship and positiveness. She has always been helpful and kind to me with a smile. In the meantime, I am grateful to her husband Olgu Demircioğlu for friendship and supports. I would like to I would also like to thank Hisham Nasser (Haşmet) for help, sharing his ideas and nice friendship.

The biggest thanks of all go to my roommates. I would like to start with Tahir Çolakoğlu (Tahir abi). In the last year, you have become my secret supervisor. We

have shared many creative ideas and worked together in a couple of subjects. I have learned a lot of from you, both as a person and a researcher. I hope I will have an opportunity to learn more in the future. I would like to continue with Makbule Terlemezoğlu (Makbuş). I am grateful to you for your nice friendship, support and talks and more talks :) You have always been kind to me and became a sister (apla). I would like to thank Musa Kurtuluş Abak for his nice friendship, infinite energy, kindness, creativity and productivity. You are the most productive person that I have ever seen before. I would also like to thank Merve Pınar Kabukçuoğlu (from the neighbor room) for endless support during the thesis. I would like send my deepest thanks to Hande Çiftpınar for her endless support, friendship, sharing her knowledge with me and helps. I hope we will have an opportunity to reach our goals in the near future. I would also like to thank Serra Altınoluk for nice friendship during the internship in Imec.

Special thanks to GÜNAM family; Bülent Arıkan, Mona Zolfaghari Borra (yanıııı), Aydın Tankut, Mücahit Yılmaz, Emre Coşkun, Mete Günöven, Gence Bektaş, Doğuşcan Ahiboz, Yasin Ergunt, Mustafa Ünal, Gülsen Baytemir, Çiğdem Doğru, Mehmet Karaman, Salar Habibpur Sedani, Yusuf Kasap, Arezoo Hosseini, Hasan Hüseyin Güllü, Seda Kayra Güllü, Özge Bayraklı. I would like to thank all GUNAM staff including Harun Tanık, Buket Gökbakan and Tuncay Güngör for their kind attitude and our technical staff Nevzat Görmez, Tayfun Yıldız, Dursun Erdoğan and Yücel Eke for supports. I would also like to thank our little buddy “Mars”.

I would like to continue with Imec i^2 module group. I would like to express my gratitude Jozef Szlufcik and Ivan Gordon for giving the opportunity of working Imec. I would like to continue with Twan Bearda who was my daily supervisor in Imec. I am grateful to him for sharing theoretical and experimental knowledge, guidance and giving me opportunity to learn experimentally. I would also like to thank Hariharsudan Sivaramakrishnan Radhakrishnan, Menglei Xu Ivan Sharlandziev, Geert Schoofs, Valerie Depauw, Kris Van Nieuwenhuysen. Patrick Choulat, Jonathan Govaerts. I am grateful for the support by European project CHEETAH.

A thousand thanks go to my buddies Şenol Girgin, his wife Fatma Girgin, Murat Akyol, his kind wife Zeynep Akyol, Alim Burak Çelik, Burak Çalışkan Ali Çiçekçi, Ümit Faruk Yenici for being always there whenever I need. It is not possible to forget you. I would like to express my gratitude to the person I love, Dilara Sunal. You made me forget about the issues and made me happy in any case, any time. Thank you for your great effort and patient. My last words go to my family including my "Prenses". I am grateful to them for continuous support, love, guidance and help. I would like to express my special gratitude to my Dad for his endless support, guidance, friendship ("yoldaş") and patient. Dad, you will always be with us and I dedicate the thesis to you.

TABLE OF CONTENTS

ABSTRACT v

ÖZ vii

ACKNOWLEDGMENTS x

TABLE OF CONTENTS xiii

LIST OF TABLES xvi

TABLE OF FIGURES xvii

NOMENCLATURE xxi

CHAPTERS

1.INTRODUCTION 1

1.1. History and Current Status of Photovoltaics 2

1.2. Solar Irradiance 6

1.3. Working Principle of Solar Cell 7

1.3.1. Formation of p-n junction 8

1.3.2. Light Absorption 9

1.3.3. Basic Solar Cell Parameters 11

1.4. Heterojunction with Intrinsic Thin Layer Solar Cells 16

2.FUNDAMENTALS OF SILICON HETEROJUNCTION SOLAR CELLS 19

2.1. Band Diagram 19

2.1.1. Carier Transport Mechanism 20

2.2. Surface Preparation 22

2.2.1. Radio Corporation of America Clean 22

2.2.2. Surface Texturing 23

2.2.3. Pyramid Rounding by Wet Chemical Etching 26
2.3. Amorphous Silicon 27
2.3.1. Density of States 28
2.3.2. Interface Trap Density 29
2.3.3. Deposition of Amorphous Silicon 31
2.3.4. Doping of Amorphous Silicon 33
2.3.5. Staebler - Wronski Effect 33
2.4. Recombination 34
2.4.1. Shockley-Read-Hall Recombination 35
2.3.2. Radiative Recombination 39
2.4.3. Auger Recombination 40
2.5. Silicon Heterojunction Solar Cell 41
2.5.1. Structure of an SHJ Solar Cell 41
2.5.2. Structure of Silicon Heterojunction IBC Solar Cell 42
2.6. Metal Contacts 44
3.EXPERIMENTAL 47
3.1. Fabrication Procedure for SHJ Solar Cell 47
3.1.1. Texturing 48
3.1.2. Standard Surface Cleaning 49
3.1.3. Pyramid Rounding Process 50
3.1.4. GÜNER Cluster System 51
3.1.5. CCP Chambers 53
3.1.6. Sputtering 55
3.1.7. Metallization 56
3.1.8. Thermal Treatment 57

3.1.8. Characterization Techniques 58
3.2. Experimental Procedure for SHJ IBC Solar Cells.. 62
3.2.1. Surface Preparation.. 63
3.2.2 Front Surface Passivation 64
3.2.3. Emitter Patterning... 64
3.2.4. Metallization.. 65
3.2.5. Characterization.. 65
4.RESULTS & DISCUSSION.. 69
4.1. Silicon Heterojunction Solar Cell Process Optimization 69
4.1.1. Wet Chemical Cleaning.. 71
4.1.2. Pyramid Rounding 73
4.1.3. Hydrogen Termination of Surface Dangling Bonds............................ 78
4.1.4. Optimization of Intrinsic a-Si:H Layer.. 79
4.1.5. Optimization of Post-annealing Treatment.. 84
4.2. Silicon Heterojunction IBC Solar Cell 94
4.2.1. Front Surface Passivation 95
4.2.2. Rear side passivation 98
5.CONCLUSION.. 111
REFERENCES.. 115
APPENDICES
APPENDIX A: BAND DIAGRAM 123

LIST OF TABLES

TABLES

Table 1: Reactions involved during HF/HNO_3 treatment 27
Table 2: Reactions occur during HF/ H_2O_2 treatment 44
Table 3: Optimized deposition parameters of n+ a-S:H layer 70
Table 4: I-V measurement results of solar cell with and without RCA clean 72
Table 5: Suns-V_{oc} results of solar cell with and without RCA clean 73
Table 6: Results for various etching time 76
Table 7: Suns-V_{OC} results of 60s etched sample 77
Table 8: Results for various HF: HCl treatment time 78
Table 9: Average results with and without rounding step 79
Table 10: Results for deposition power at 1 Torr 81
Table 11: Results for deposition power at 0.6 Torr 82
Table 12: Results for 15W and 0.3Torr 82
Table 13: Resistivty results for RTA treatment 86
Table 14: Annealing effect on resistivity AZO growth by various power 86
Table 15: Device results after annealing 88
Table 16: Solar cell results with respect to post-annealing duration at 210°C 91
Table 17: Suns-VOC results for two efficient solar cells 92
Table 18: Lifetime results 96
Table 19: Results for post-annealing and ageing studies 98
Table 20: Results for ageing study 102
Table 21: Reuslts for various concentration of BOE 103
Table 22: Comparision of etchants 105
Table 23: The SHJ IBC solar cell results 109

LIST OF FIGURES

FIGURES

Figure 1: Estimation of world energy demand [2] 1
Figure 2: Percentage of global annular production [9] 4
Figure 3: The best cell efficiencies [10] 4
Figure 4: Price of silicon PV cells [11] 5
Figure 5: Solar spectrum reaching the Earth surface [13] 6
Figure 6: Fundamental operating principle of solar cell 7
Figure 7: Band diagram of p-n junction 8
Figure 8: Cross-sectional view of p-n junction 9
Figure 9: Electron excitation for an indirect band gap 10
Figure 10: I-V characteristic of solar cell under illumination and dark condition 12
Figure 11: Equivalent circuit of solar cell 12
Figure 12: I-V characteristic and FF calculation 14
Figure 13: External Quantum Efficiency graph 16
Figure 14: The cell structure of Panasonic [19] 17
Figure 15: The cell structure of Kaneka Corporation [20] 18
Figure 16: Band diagram of heterojunction Si solar cell 20
Figure 17: Anisotropic etching 24
Figure 18: Schematic representation of reflection losses from flat (a) and textured (b) surface 25
Figure 19: Change in D_{it} (E) on p-type Si surfaces after RCA cleaning and oxide removal during the formation of pyramids [30] 26
Figure 20: Distribution of Si atoms (a) in crystalline and (b) amorphous form [35]. 28
Figure 21: Density of states (DOS) distribution of c-Si (a) and a-Si:H (b) 29
Figure 22: Energy band diagram of the interface between a-Si:H (n+) and c-Si 30

Figure 23: Dependence of the V_{oc} of a SHJ solar cell on the defect state density at the interface D_{it} (E). The D_{it} (E) values at the x-axis represent only the mid-gap defect density [41] 31
Figure 24: Schematic representation PECVD chamber 32
Figure 25: Transitions of SRH recombination (a) capture of electron, (b) emission of electron, (c) capture of hole, (d) emission of hole 35
Figure 26: Schematic of radiative recombination 39
Figure 27: Schematic of the Auger recombination 40
Figure 28: Structure of a Heterojunction Silicon Solar Cell 42
Figure 29: Demonstration of SHJ IBC solar cell 43
Figure 30: Process flow of SHJ solar cell including a) wet chemical process and b) device structure 48
Figure 31: Wet chemical process sequences 49
Figure 32: The standard chemical cleaning in GÜNAM 50
Figure 33: Chemical process flow including pyramid rounding step 51
Figure 34: GÜNER System 52
Figure 35: Schematic view of GÜNER System 52
Figure 36: Schematic view of CCP chambers 54
Figure 37: Schematic view of the sputtering chamber 55
Figure 38: Thermal evaporation system 56
Figure 39: AS-Micro RTA System 57
Figure 40: Light intensity and VOC as a function of time 58
Figure 41: Double diode representation of Suns-VOC measurement 59
Figure 42: Schematic view of reflection set-up in GÜNAM 61
Figure 43: Schematic view of QE set-up in GÜNAM 61
Figure 44: Fabrication process flow for SHJ IBC solar cell (a) and device structure (b) 63
Figure 45: Schematic representation of BT imaging system 66
Figure 46: The structure of the SHJ solar cell 69
Figure 47: The front view of fabricated single side SHJ solar cell 70
Figure 48: J-V graph of the efficient solar cell with RCA clean 72

Figure 49: Reflection results of etched samples 74
Figure 50: SEM images a) without etching b) 30s etched c) 80s etched and d) 120s etched textured wafer 75
Figure 51: The variation on (a) V_{OC} and (b) J_{SC} with respect to etching time 77
Figure 52: J-V curve of the best cell 79
Figure 53: Experimental flow for SHJ solar cell 80
Figure 54: J-V graph of various deposition conditions 83
Figure 55: V_{OC} results for various deposition power and pressure 83
Figure 56: Device structure of post-annealing experiments (a) on only AZO layer (b) on SHJ solar cell 85
Figure 57: The resistivty values for various post-annealing treatment 87
Figure 58: (a) V_{OC}, (b) J_{SC}, (c) FF, (d) ɲ, (e) R_S, (f) R_{SH} variation with respect to annealing temperature 89
Figure 59: J-V curves for different annealing temperature 90
Figure 60: J-V curves of various annealing duration 91
Figure 61: EQE result of the efficient solar cell 92
Figure 62: J-V curve of the best SHJ solar cell fabricated in GÜNAM Laboratories 93
Figure 63: Fabrication sequence and device structure in Imec 94
Figure 64: Passivated samples with (a) i a-Si:H layer and (b) i a-Si:H/SiN_X 95
Figure 65: Calibrated PL images after (a) i a-Si:H deposition and (b) SiNx deposition 96
Figure 66: Effective lifetime results 97
Figure 67: Experimental sequence and device structure 99
Figure 68: Correlations between BOE and etch rate, effective lifetime 100
Figure 69: Calibrated PL images of repassivated samples after (a) 10min (b) 15min (c) 20min (d) 25min etching 101
Figure 70: TEM resutls for (a) sample etched by BOE: H_2O_2 (b) BOE: HNO_3: H_2O 104
Figure 71: Shematic representation of process steps 105
Figure 72: PL image of etched area 106

Figure 73: After i/n+ deposition on the etched samples by BOE: H_2O_2 at concantration of (a) 1:5 and (b) 1:10..106
Figure 74: The effective lifetime results of BOE: H202 for various concentrations107
Figure 75: Fabrication flow of SHJ IBC solar cell..108
Figure 76: Calibrated PL images after (a) front and rear side passivation and (b) re-passivation..108
Figure 77: The efficient solar cell J-V graph 109
Figure 78: Band diagram for SHJ solar cell on p type c-Si substrate 123

NOMENCLATURE

a-Si:H	Hydrogenated amorphous silicon
AM1.5	Air Mass 1.5
Al	Aluminum
ARC	Antireflection coating
BSF	Back surface field
CB	Conduction band
c-Si	Crystalline silicon
Cz	Czochralski
CVD	Chemical Vapor Deposition
E	Energy
E_G	Energy band gap
Epifoils	Epitaxially grown silicon foils
FF	Fill factor
HF	Hydrofluoric acid
ICP	Inductively Coupled Plasma
I_{SC}	Short circuit current
J	Current density
J_{mpp}	Current density at maximum power point
J_0	Dark saturation current density
J_{SC}	Short circuit current density
KOH	Potassium hydroxide
N_D	Doping concentration
PECVD	Plasma enhanced chemical vapor deposition
P_{mpp}	Power density at maximum power point
R	Reflectance
R_S	Series resistance
R_{SH}	Shunt resistance

SEM	Scanning Electron Microscope
SiN_x	Silicon nitride
SiO_2	Silicon dioxide
T	Transmittance
TEM	Transmission Electron Microscopy
TCO	Transparent Conductive Oxide
TMAH	Tetramethylammonium hydroxide
V	Voltage
VB	Valence band
V_{mpp}	Voltage at maximum power point
V_{oc}	Open circuit voltage

CHAPTER 1

INTRODUCTION

Dramatic increase in energy demand all over the world pushes the research to focus on alternative energy sources. World energy consumption is estimated to grow by one-third between 2013 and 2040 as illustrated in Figure 1 [1-2], which is proportional to the developments on technology, daily life standards and rapid increase in world's population. Today, 67% of total electricity generation is provided by fossil fuels, which has a significant impact on carbon dioxide emissions.

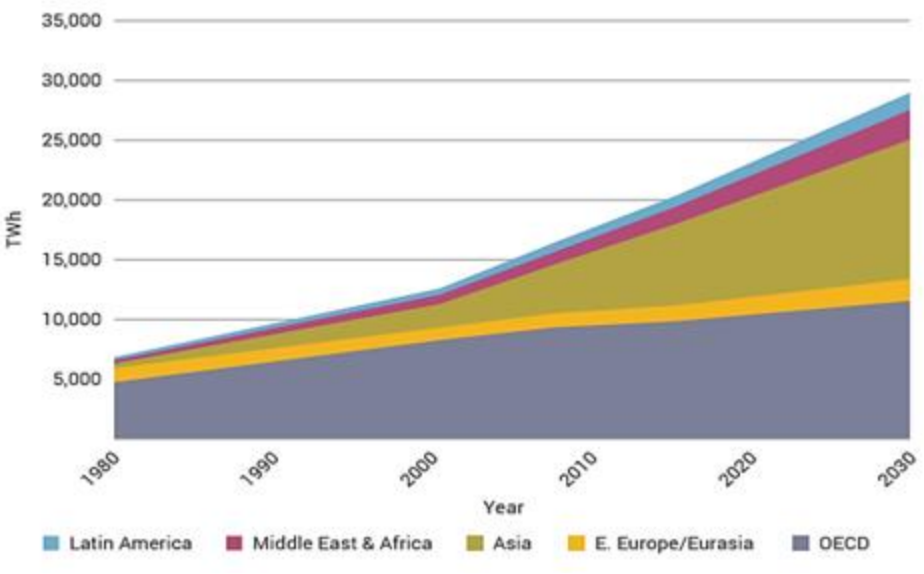

Figure 1: Estimation of world energy demand [2]

The world is almost coming to end of the non-renewable energy sources such as coal, natural gas and oil [3]. Furthermore, carbon emission from these sources has a critical impact on the greenhouse effect and global warming. With respect to World Energy Outlook published in 2009, it was predicted that nuclear electricity generation capacity would be increased around 60% in the next 20 years [2]. Despite this scenario; on 11th March 2011, the world has faced with incredibly heartbroken disaster, which is called Fukushima Catastrophe. An earthquake on the coast of Japan with a magnitude of 9.0 on the Richter scale caused a tsunami. The tsunami has destroyed the nuclear power plant in Fukushima. Because of the radioactive contamination around Fukushima, decades might be needed to make Fukushima habitable, again.

To supply energy demand of the world, nuclear power is one of the powerful candidates; however, after the Fukushima catastrophe, people has felt a strong disinclination about nuclear power. After this catastrophe, the German government has announced a plan to shut down all nuclear power plants in the next 11 years. The aim of this plan is to have 35% of the total energy consumption of Germany from renewable energy sources until 2022, instead of nuclear energy [4].

As a result of concerns about the future of energy generation, renewable energy researches have been increasing drastically. Today, sustainable and clean energy sources (such as wind, hydro, geothermal and solar) have become the main focus of energy generation. Photovoltaic (PV) solar energy provides a good opportunity to shape the future of the world with a potential of unlimited energy.

1.1. History and Current Status of Photovoltaics

Solar energy originates in radiations emitting from the Sun that can be divided into two: charged particles and electromagnetic radiations. Charged particles mostly consist of electrons and protons with energies typically between 1.5 keV to 10 keV. Electromagnetic radiation that comes from the sun exists with various wavelengths including radio waves, infrared visible waves, ultraviolet, X-rays and Gamma rays.

From this spectrum, only a couple of electromagnetic waves could reach the surface of the Earth (visible spectrum, radio waves and a short-range of infrared waves). On the other hand, most of the charged particles coming from the sun cannot reach the surface of the Earth because of the magnetosphere [5]. The amount of energy reaches the surface of the earth is about $1kW/m^2$ and it is dependent on the latitude, altitude and weather conditions.

Photovoltaic devices convert solar energy to electricity, directly. The discovery of photovoltaic effect by Becquerel in 1839 is accepted as the starting point of PV technology. Forty years later from this crucial observation, in 1876, the first PV devices were constructed by William Adams and Richard Day by using selenium with heated platinum contacts [6]. Later, the relationship between PV properties of metal-semiconductor surfaces and existence of energy barrier was described by Goldman and Brodsky in 1914. The theory behind the metal-semiconductor energy barrier layer was found by W. Schottky and his colleagues in 1930's [7].

In 1950's, the developments in silicon electronics led to finding a way for enhanced photovoltaic properties by p-n junction. The first silicon solar cell was reported with an efficiency of 6% by Chapin, Fuller, and Pearson in 1954. In the same year, the first cadmium sulphide p-n junction was reported with an efficiency of 6% [8].

In 1970's, as a consequence of the oil dependent energy crisis, alternative energy sources were gained great interest including PV energy. In those years, excluding space applications, the general trend was to find alternative materials for producing photovoltaic devices more cheaply and to increase the efficiency values to higher levels via using tandem and multiple band gap designs. In the late 1990's, PV production expanded at a rate of 15 -20% per annum [6].

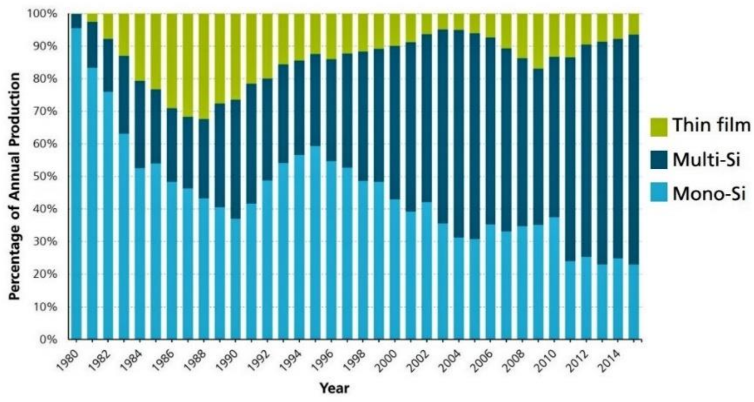

Figure 2: Percentage of global annular production [9]

Figure 2 shows the percentage of global annular production. The general technology trend is focused on crystalline Silicon (c-Si) based solar cells. Reduction in the cost of raw materials led to a new application area on the photovoltaic devices. In Figure 3, the best research-cell efficiencies are shown in a well-known chart and it includes all kinds of photovoltaic devices such as multi-junction, single junction, thin film solar as well as emerging PV technologies like dye-sensitized and organic solar cells.

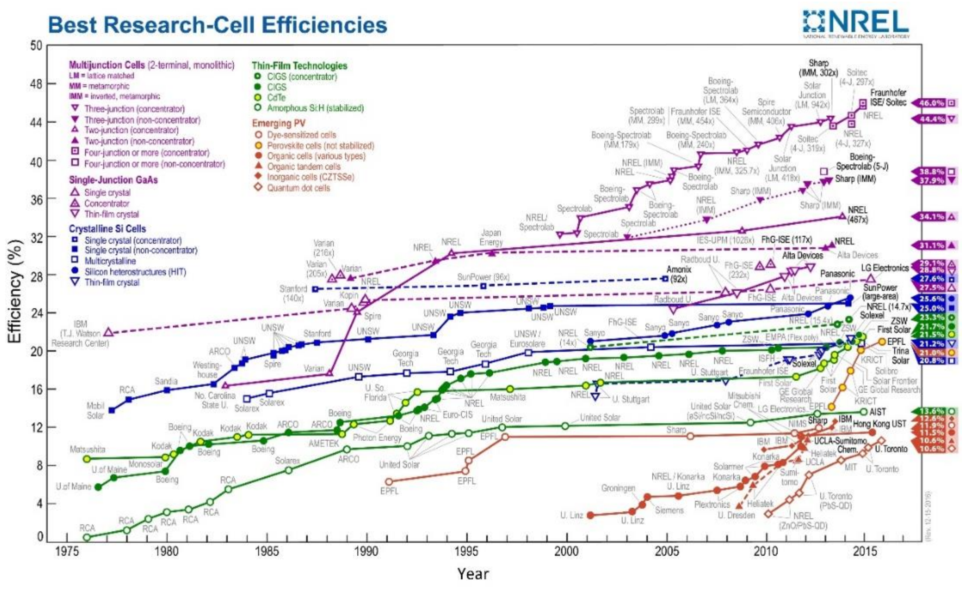

Figure 3: The best cell efficiencies [10]

Silicon solar cells are dominant in PV market because of two main reasons; (i) silicon is one of the most abundant materials on earth's crust and (ii) the production cost of Si solar cell has been decreasing due to improvement on manufacturing techniques. In Figure 4, the price reduction trend of c-Si solar cells is shown with respect to years.

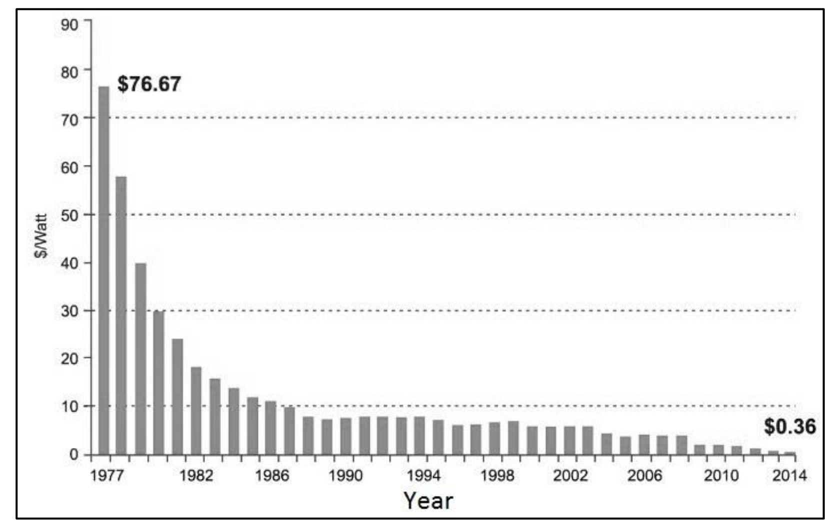

Figure 4: Price of silicon PV cells [11]

c-Si solar cell technology is encompassed by p-type c-Si wafer due to historical background and developments. On the other hand, the latest results on c-Si technology show that the highest efficiencies are reported on n-type c-Si wafers that are Interdigitated Back Contact (IBC) by SunPower and Heterojunction with an Intrinsic Thin layer (HIT) by Panasonic [12] HIT solar cell gives better performance in terms of high open circuit voltage, efficiency, low temperature processes and low temperature coefficients.

1.2. Solar Irradiance

The power per unit area received from the Sun is called solar irradiance. On the surface of the Sun, solar irradiance approximately equal to the spectrum of the black body at 5760K [6]. The solar radiation reaches the surface of the Earth is about 1360 W/m^2. While incident light passing through the layers of Earth's atmosphere, some wavelengths could not reach to the surface because of absorption and scattering. This loss is arising from the absorptive properties of water molecules and CO_2.

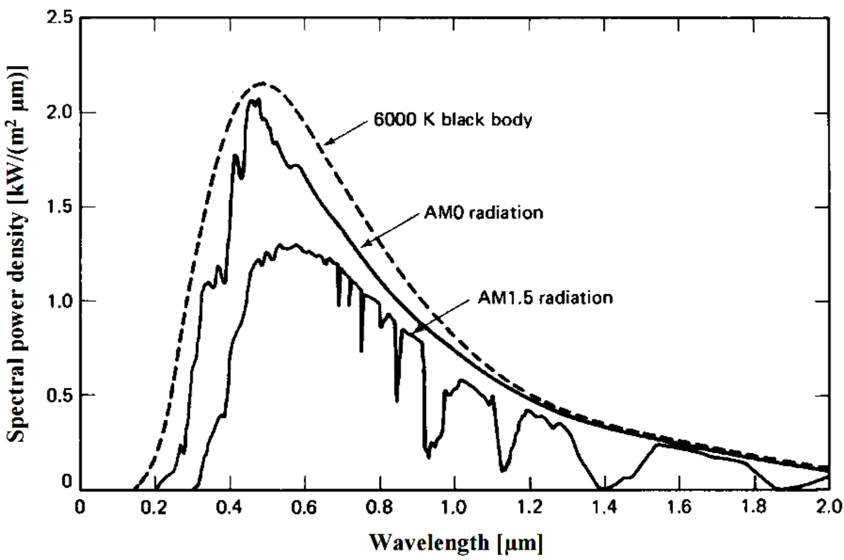

Figure 5: Solar spectrum reaching the Earth surface [13]

The reduction in power of light is quantified by the Air Mass (A.M.) factor as illustrated in Figure 5. It is defined as follows;

$$AM = \frac{optical\ path\ length\ to\ Sun}{optical\ path\ length\ if\ Sun\ directly\ overhead} = \frac{1}{cos(\theta)} \qquad \text{(Eq. 1.1)}$$

The angle “θ” defines the zenith angle. From above formula, AM 0 defines the radiation just outside the atmosphere. When the Sun is directly overhead (θ=0), the Air Mass is 1. AM 1.5 corresponds to the angle 48.2° between the position of Sun and vertical axis.

1.3. Working Principle of Solar Cell

A solar cell is basically electronic device acting like a diode. It converts sunlight directly to electricity and produces both a current and a voltage. Most solar cells are based on semiconductor p-n junctions. The fundamental operating principle of a SHJ type cell is illustrated in Figure 6 and is as following:

- Absorption of the sunlight by solar cell,
- Generation of electron-hole pair,
- Separation of an electron-hole pair and collecting charge carriers through the metal contacts.

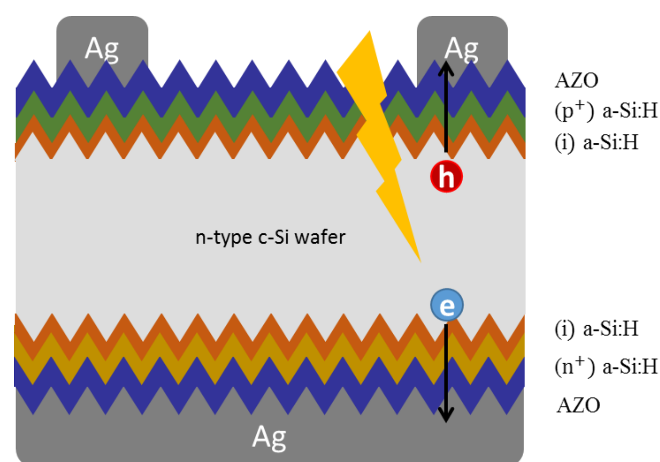

Figure 6: Fundamental operating principle of solar cell

1.3.1. Formation of p-n junction

A p-n junction is formed by physical contact of n-type and p-type material. Conduction and valance bands of each side will bend in vicinity of the junction and the net current will be zero in thermal equilibrium. The band diagram of the p-n junction is demonstrated in Figure 7.

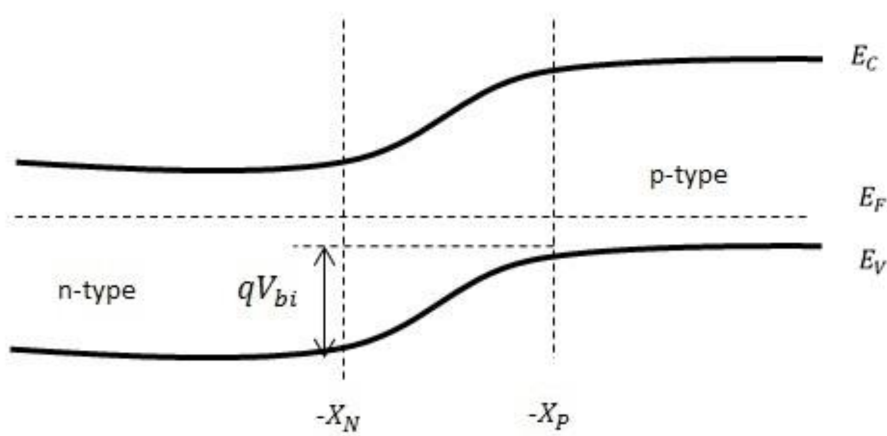

Figure 7: Band diagram of p-n junction

Due to the difference in charge carrier concentration between p-type and n-type regions, diffusion of electrons from n-side to p-side and that of holes from p-side to n-side occurs which results in positively and negatively charged region. Depletion region (or space charge region) is an area where charge transition occurs between n- and p- type regions as illustrated in Figure 8. Remaining region of each side of the semiconductor is called as quasi-neutral region [14].

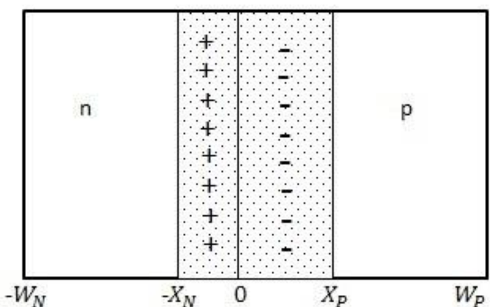

Figure 8: Cross-sectional view of p-n junction

An induced electrical field at the depletion region leads to drift of minority carriers through the junction which is resulted in increased collection probability of charge carriers.

1.3.2. Light Absorption

The incident photon coming to the surface of solar cell interacts with material in three possible ways; (i) reflected from the surface of material, (ii) absorbed by the material or (iii) transmitted through the material by losing energy. Incident photon energy should be equal or higher then band gap energy of the material to generate current. In other words, the minimum energy needed to make electron transition from valance band to conduction band is equal to band gap energy. For direct band gap materials, both energy and momentum are conserved. Absorption coefficient (α) is directly proportional to band gap energy and incident photon [14].

For indirect band gap materials, to conserve momentum, phonon emission or absorption takes a role on the absorption of incident light.

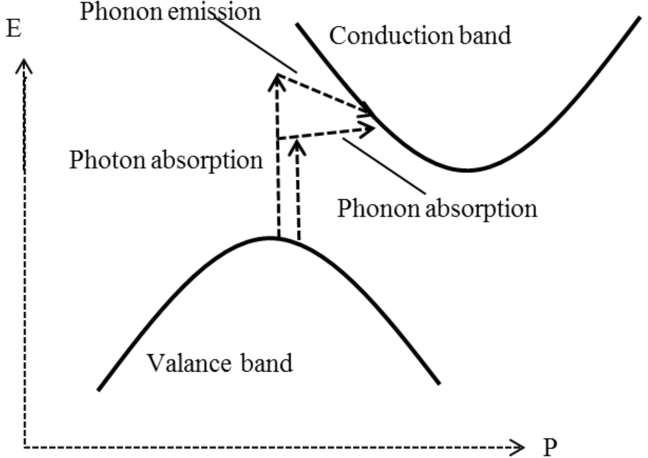

Figure 9: Electron excitation for an indirect band gap

As illustrated in Figure 9, to conserve momentum, either phonon is absorbed or is emitted. The absorption coefficient depends on not only incident photon and band gap energy but also the availability of phonons. Furthermore, absorption depth (photon traveling distance in medium) is inversely proportional to absorption coefficient (α^{-1}). The absorption coefficient of material is deterministic on generation rate of electron and hole pairs. In addition to absorption coefficient of material, reflection from the surface of solar cell, incident photon flux and the shadowing losses due to the metallization have effect on generation rate. The generation rate of electron and hole pairs is calculated following equation;

$$G(x) = (1 - s)\int_{\lambda}(1 - r(\lambda))f(\lambda)\alpha(\lambda)e^{-\alpha x}d\lambda \ , \qquad \text{(Eq. 1.2)}$$

where s is grid shadow, r is reflectance, f is photon flux.

1.3.3. Basic Solar Cell Parameters

The current - voltage behavior of a solar cell can be modeled by the ideal diode equation (Eq. 1.2) under dark condition.

$$I = I_0\left(e^{qv/kT} - 1\right),\qquad \text{(Eq. 1.3)}$$

In Eq. 1.3, I is the net current, I_0 is reverse saturation current determined by material quality, q is the electron charge (eV), k is the Boltzmann's constant (8.617×10^{-5} eV/K) and T is the temperature (K) of a solar cell. Under illuminated condition of a solar cell, the current will be generated by incident light represented by;

$$I = I_0\left(e^{\frac{qv}{kT}} - 1\right) - I_{ill},\qquad \text{(Eq. 1.4)}$$

where I_{ill} refers to the current generated under illumination. In order to characterize solar cells, the I-V curve is conventionally shown in 1st quadrant and then the current represented by;

$$I = I_{ill} - I_0\left(e^{\frac{qv}{kT}} - 1\right),\qquad \text{(Eq. 1.5)}$$

The incident light has an effect on the current (I)-voltage (V) curve in the fourth quadrant as shown in Figure 10.

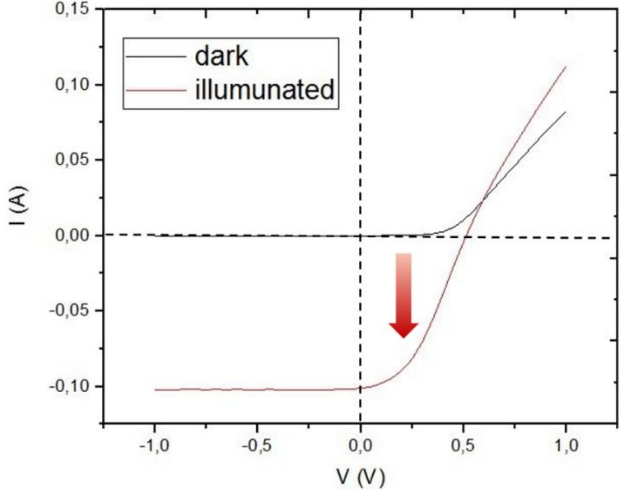

Figure 10: I-V characteristic of solar cell under illumination and dark condition

Short-circuit current ($\boldsymbol{I_{SC}}$) is the maximum current at zero voltage condition. In the ideal case, $I_{SC} = I_{ill}$. Short-circuit current is dependent on;

- Surface area of solar cell (but it is usually expressed as short circuit current density (J_{SC}) with eliminating the effect of area),
- Intensity of light and the incident light spectrum,
- Optical properties of material,
- The collection probability of electrons and holes.

Open-circuit voltage ($\boldsymbol{V_{oc}}$) is the maximum voltage that could be produced by solar cell at zero current. The equivalent circuit model of solar cell is shown in Figure 11.

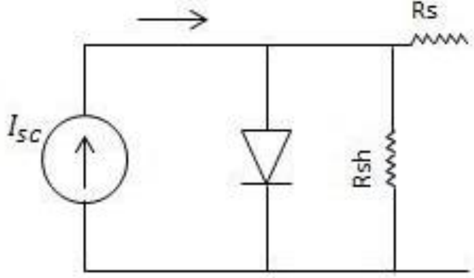

Figure 11: Equivalent circuit of solar cell

The open circuit voltage for ideal solar cell can be defined as;

$$V_{OC} = \frac{kT}{q} \ln\left(\frac{I_{SC}+I_0}{I_0}\right) \quad , \qquad \text{(Eq. 1.6)}$$

where I_0 is dark saturation current. V_{oc} changes logarithmically with respect to sunlight. The dark saturation current depends on recombination through the bulk and on the surface which means that value of V_{oc} is proportional to the quality of material. Furthermore, the dark saturation current decreases as the band gap energy increases which leads an increase on the open circuit values. In other words, the band gap energy of the material has a deterministic effect on V_{OC}.

The open circuit voltage can be also defined by carrier concentration as following equation;

$$V_{OC} = \frac{kT}{q} \ln\left(\frac{(N_A+\Delta n)\Delta n}{n_i^2}\right) \quad , \qquad \text{(Eq. 1.7)}$$

where N_A is doping concentration, Δn is excess carrier concentration and n_i is intrinsic carrier concentration. Implied V_{OC} term is determined from carrier concentration from Eq. 1.7. The implied V_{OC} is commonly calculated from effective lifetime measurements.

Fill factor (FF) is the ratio of maximum power to product of total V_{oc} and I_{SC} as the following equation;

$$FF = \frac{V_{mp} \cdot I_{mp}}{V_{oc} \cdot I_{sc}} = \frac{P_{mp}}{P_T} \quad , \qquad \text{(Eq. 1.8)}$$

P_T is the theoretical power value of a solar cell. For the ideal solar cell, FF should be equal to 1. It could be also calculated by the ratio of areas covered by the blue rectangle that refers (P_{mp}) to the red rectangle (P_T) shown in Figure 12. Fill factor also defines the squareness of I-V characteristic of solar cell.

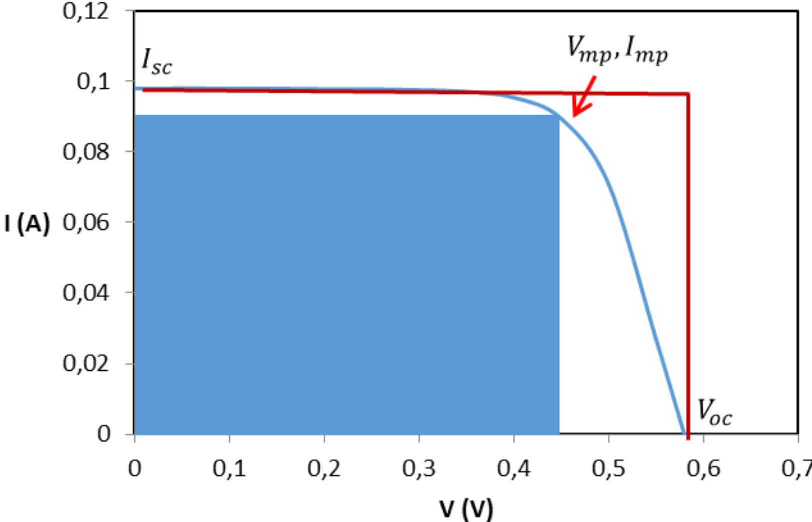

Figure 12: I-V characteristic and FF calculation

Efficiency (η) is the ratio of power generated by solar cell compared to incident light power density as the following equation;

$$\eta = \frac{P_{mp}}{P_{in}} = \frac{FF.V_{oc}.I_{sc}}{P_{in}} \quad , \qquad \text{(Eq. 1.9)}$$

Incident light power density (P_{in}) is determined by not only incident light spectrum, but also altitude and latitude of the measurement point and angle of incident light. Particular illumination conditions are defined for solar cell characterizations. The Air Mass 1.5 Spectrum is The Standard Test Condition which has an incident light power density of $1000W.m^{-2}$ at room temperature.

In solar cells, generated power is dissipated through parasitic resistance. In Figure 11, the equivalent circuit is shown in single diode model including series (R_s) and shunt (R_{sh}) resistances.

The main reason of ***series resistance (R_S)*** is metal-semiconductor interfaces, current flow transverse in solar cell and metal itself. The series resistance is defined in Eq. 1.10. To attain higher conversion efficiencies, series resistance should be minimized.

$$R_S = (\frac{dV}{dI})_{V=Voc} \qquad \text{(Eq. 1.10)}$$

On the other hand, the ***shunt resistance (R_{SH})*** is mainly caused by defects through manufacturing of Si wafers or production defects in c-Si solar cells. Shunt resistance refers to alternative current paths that lead to undesired leakage. It is formulated in Eq. 1.11 as;

$$R_{SH} = (\frac{dV}{dI})_{V=0} \ , \qquad \text{(Eq. 1.11)}$$

For the ideal solar cell, parasitic resistance should be $R_S = 0 \ and \ R_{SH} = \infty$.

Quantum Efficiency (QE) is simply the ratio of converted and collected charges to a number of incident photons. The integration of the QE over the solar spectrum results in the amount of current generated by the solar cell. For the ideal solar cell, the QE is defined as "1" and it means that all incident photons are converted and collected as electrons as shown in Figure 13. For a solar cell, two types of the QE are considered;

External Quantum Efficiency (EQE) is the ratio of collected charges carriers to a number of incident photons. Therefore, all reflection and transmission losses are taken into account.

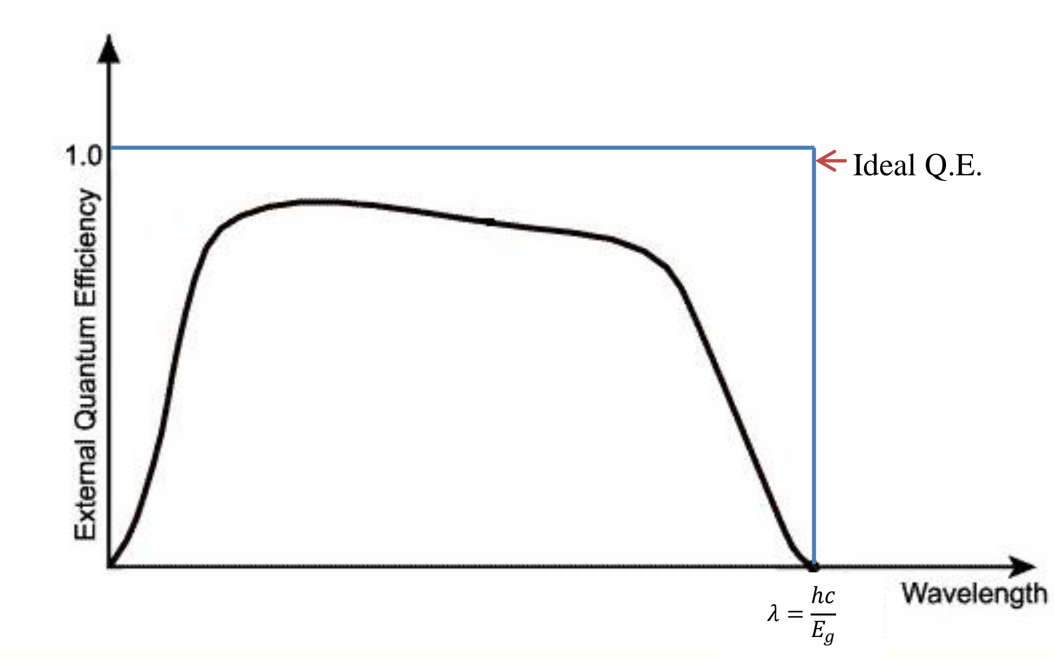

Figure 13: External Quantum Efficiency graph

Internal Quantum Efficiency (IQE) is the ratio of collected charges carriers to the number of absorbed photons. Hence, the losses coming through reflection and transmission are eliminated.

$$EQE = \frac{electron/s}{photons/s} \quad \text{(Eq. 1.12)}$$

$$IQE = \frac{electron/s}{absorbed\ photons/s} \quad \text{(Eq. 1.13)}$$

1.4. Heterojunction with Intrinsic Thin Layer Solar Cells

The researches on amorphous hydrogenated silicon (a-Si:H) and c-Si heterojunction interface were started in 1983 by observation on the excellent passivation quality of a-Si on the c-Si surfaces. The first heterojunction solar cell was fabricated in 1983 by Hamakawa [15-16]. Sanyo was the pioneer of the c-Si

heterojunction solar cells. In 1992, the potential of a-Si:H technology and heterojunction solar cell structure were demonstrated by Sanyo. The serial production of heterojunction with intrinsic thin layer was achieved by Sanyo with module efficiency 14.4% in 1997, and the solar cell structure denominated as the brand name HIT [17-18]. In 2012, the brand name of Sanyo's solar modules has changed from "Sanyo" to "Panasonic". Nowadays, Panasonic is the market leader of the HIT solar cells. In 2013, Panasonic has achieved the world's record conversion efficiency as 24.7% in cell area 143.7 cm^2 on a thin c-Si substrate (~100µm) with the solar cell structure shown in Figure 14 [19].

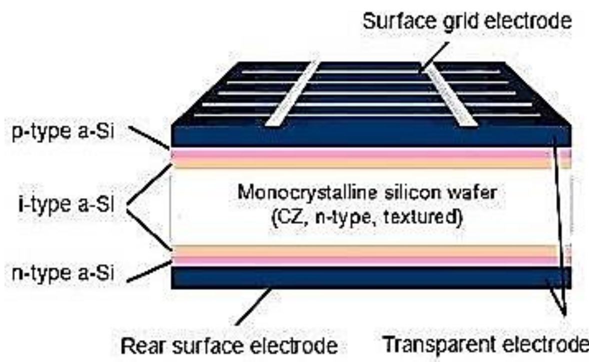

Figure 14: The cell structure of Panasonic [19]

Panasonic was reported a new world's record with 25.6% conversion efficiency for its HIT solar cell in 2014 with the help of reduction recombination and optical losses by using interdigitated back contacts and minimizing resistance losses. However, in September 2016, Kaneka Corporation has achieved the world's highest conversion efficiency as 26.33% in a practical size (180 cm^2) HIT solar cell as shown in Figure 15 [20].

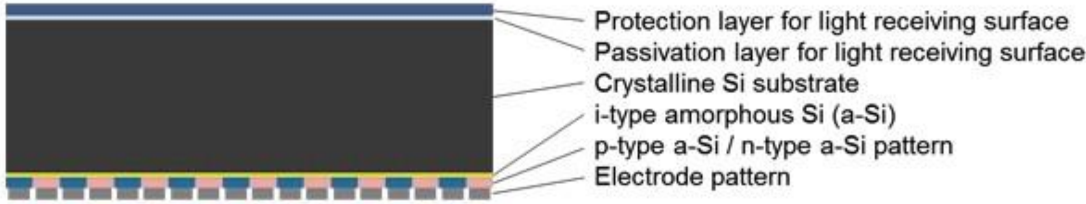

Figure 15: The cell structure of Kaneka Corporation [20]

The key point behind the success of silicon heterojunction (SHJ) solar cells belongs to the behavior of intrinsic thin a-Si:H layer that leads excellent surface passivation resulting in high open-circuit voltages. The advantages of SHJ solar cell structure from the perspective of processing steps could be listed as;

- Low process temperature (<200 ºC) prevents degradation of bulk quality.
- Low thermal budget.
- Simplified process steps compared to conventional c-Si solar cells.
- Developments on thin c-Si substrates (~100µm).

Apart from Sanyo and Kaneka, several groups and industrial companies have reported above 22% efficiency on SHJ solar cell with interdigitated back contact (IBC) structure [21]. The recent interest has risen on IBC structure. In consequence of having both contacts at the rear surface of the solar cell, reflection and shadowing losses due to the front was eliminated.

CHAPTER 2

FUNDAMENTALS OF SILICON HETEROJUNCTION SOLAR CELLS

Fabrication sequence of a typical SHJ solar cell can be investigated under two main process steps; (i) surface preparation including wet chemical treatments and (ii) device fabrication. The surface preparation starts with the chemical surface cleaning and texturing of c-Si wafers. The wet chemical cleaning procedures have a great influence on solar cell parameters. In order to get ultraclean surfaces, a couple of standard wet chemical cleaning methods have been performed by several research groups all over the world [22]. The device fabrication process includes the sequential deposition of a-Si:H layers, the growth of Transparent Conducting Oxide (TCO) thin films on the cleaned wafer surface, which is followed by the metallization process for the formation of metal contacts.

2.1. Band Diagram

SHJ solar cells are formed by matching materials with different band gaps. The optical band gap energy of a-Si:H layer is accepted around 1.80 eV where Si has band gap energy of 1.12 eV. Due to the difference between the band gap energies, the mismatch takes place on the conduction and valence band edge levels as shown in Figure 16.

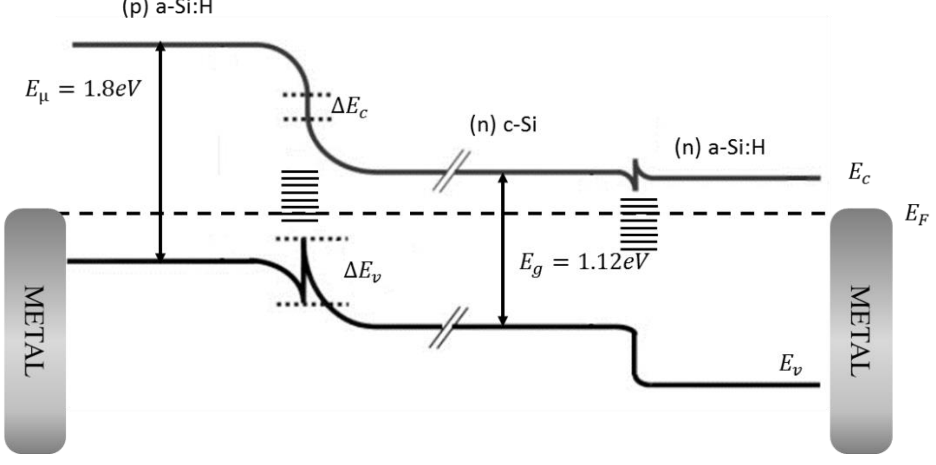

Figure 16: Band diagram of heterojunction Si solar cell

In Figure 16, the band diagram is illustrated for the widely used SHJ solar cell structure on n type c-Si substrate. The band diagram of the SHJ solar cell on p type c-Si is described and explained in Appendix A. The barrier formed for the holes at a-Si:H (p region) and c-Si interface with the height of ΔEv is called as spike. Holes are accumulated at the spike and drifted either by tunneling through the barrier via trap-assisted tunneling or by thermionic emission. Furthermore, secondary barrier is formed for electrons at the conduction band of other interface.

2.1.1. Carier Transport Mechanism

In a solar cell, charge carriers are electrons and holes which move freely in a lattice. If there is no external electric field, electrons and holes will move in a random direction depending on their thermal energies. When an electric field is applied, bands will be inclined, thus, carriers move along a specific direction. Under the effect of electric field, the random velocity of carrier will be superposed as the net velocity which is called *drift velocity* [14]. Drift velocity is directly proportional to the applied electric field ($\vec{E} = |\nabla\emptyset|$). The drift velocity ($\vec{v}_d$) is found by the following equitation;

$$|\overrightarrow{v_d}| = |\mu E| = |\mu \nabla \emptyset| \ , \quad \text{(Eq. 2. 1)}$$

where μ is the mobility and the drift current densities for electrons and holes are calculated by the following equations;

$$\vec{J}_p^{drift} = qp\vec{v}_{d,p} = q\mu_p pE \quad \text{(Eq. 2.2)}$$

$$\vec{J}_n^{drift} = qn\vec{v}_{d,n} = q\mu_n nE \quad \text{(Eq. 2.3)}$$

In the condition without external field acting, electrons and holes will move randomly, however; they tend to move from higher concentration region to lower concentration region. The velocity based on movements of carriers with respect to gradient differences on concentration is called *diffusion velocity* [14]. Diffusion currents of electrons and holes are calculated by the following equations;

$$\vec{J}_p^{diff} = -qD_P \nabla p \ , \quad \text{(Eq. 2.4)}$$

$$\vec{J}_n^{diff} = qD_n \nabla n \ , \quad \text{(Eq. 2.5)}$$

where D_P is the hole diffusion coefficient and D_n is the electron coefficient. Total current can be defined as a sum of drift and diffusion current for holes and electrons as defined in the following equation;

$$J_{tot} = \vec{J}_p^{diff} + \vec{J}_n^{diff} + \vec{J}_p^{drift} + \vec{J}_n^{drift} \qquad \text{(Eq. 2.6)}$$

The diffusion current is become dominant on the current at high forward bias for heterojunction structures as occur in p/n homojunction structures. Despite the drift and diffusion currents, several tunneling mechanism could be describe for heterojunction structure. The first mechanism is tunneling through barriers (spikes) shown in the band diagram. The other mechanism is mutlitunneling by capture and emission process. The mechanism indicates that the charge carrier is captured through defects and the charge carrier tunnels through defects until it reaches conduction band or recombines to valance band. This mechanism is called multitunneling capture and emission [30].

2.2. Surface Preparation

2.2.1. Radio Corporation of America Clean

Developed by Werner Kern in 1965, the Radio Corporation of America (RCA) cleaning is accepted as the preliminary surface preparation step for Si wafer before fabricating solar cell [23-24]. The cleaning procedure includes the removal of organic and metallic residues from the surface. For this purpose, two distinct chemical cleaning recipes were developed in RCA which were named as RCA-1 (or Standard Clean 1) and RCA-2 (or Standard Clean 2).

RCA-1 Clean

RCA-1 (SC-1) clean is used to remove organic residues from Si surface. The chemical reaction is based on oxidation with hydrogen peroxide (H_2O_2) – ammonium hydroxide (NH_4OH) – deionized water (H_2O) mixture whose temperature is kept at 70ºC. It oxidizes the surface and leaves with a thin oxide (< 2nm) on top of the surface [25]. In order to attain an impurity free Si surface, the thin oxide layer should be removed by a diluted hydrofluoric acid (HF) solution resulting in a hydrogenated surface.

RCA-2 Clean

RCA-2 (SC-2) clean is used to remove metal ions from Si surface. The chemical reaction is based on oxidation with hydrochloric acid (HCl) – hydrogen peroxide (H2O2) – deionized water (H2O) mixture having temperature of around 70ºC [23]. RCA-2 clean has similar wet chemical behavior with RCA-1.

Piranha Clean

Piranha Clean is also known as Sulfuric-Peroxide Mixture (SPM), is one of the strongest cleaning method for organic residues from Si surface though not effective on metal ions. It is also commonly used to strip photoresists. The chemical reaction is exothermic and temperature of the solution rises up to 100–130ºC. The solution is prepared by using sulfuric acid (H2SO4) – hydrogen peroxide (H2O2) [25]. Similar to RCA clean, it leaves behind a surface coated with a thin oxide layer at the end of the reaction.

2.2.2. Surface Texturing

Surface texturing is needed to increase the absorption probability of photons through an improved light trapping within Si during the fabrication of efficient Si solar cells. Due to band gap energy of Si (1.12eV), photons coming with less energy than 1.12eV, which corresponds to the wavelength of ~ 1100nm, can not absorbed by Si. In other words, it is not possible to generate of e^-- h^+ pairs for incident photons with

energy lower than 1.12eV. In addition to absorption losses, reflection losses also result in a significant reduction in the cell performance. The reflection loss at 700nm wavelength is around 40% for flat Si surfaces [26]. To minimize both reflection and absorption losses, either thicker Si wafer should be used or surface of the wafer should be textured in a way that optical path length of the incident photon is increased. In the former case, the increased wafer thickness means that the distance traveled by generated carriers is going to be increased before being recombined. This leads to a decrease in the collection probability of charge carriers. Furthermore, production cost is also raised if an increased wafer thickness is used in solar cell fabrication. For this reason, the most reasonable solution to this problem is to optimize the optical path length of the incident light by texturing the surface appropriately. The surface texturing is generally realized by the wet chemical etching of Si. With the help of texturing; incident light will interact more than one time with the surface which is positioned at a certain angle with respect to the incident light. Thus, the light would be trapped within the surface of the wafer. As a result, physically thin optically thick wafers would be obtained. Anisotropic etching using alkaline solutions is widely applied to form pyramids with random sizes and distribution on the surface which is the most common way of light trapping for solar cells. Depending on the crystallographic orientation, the etch rate of KOH is going to be differs due to different atomic densities at varying orientations [27]. The etching mechanism is anisotropic which leads higher etch rate along (100) than (111) direction as shown in Figure 17 and texturing is resulted in random pyramids on the surface.

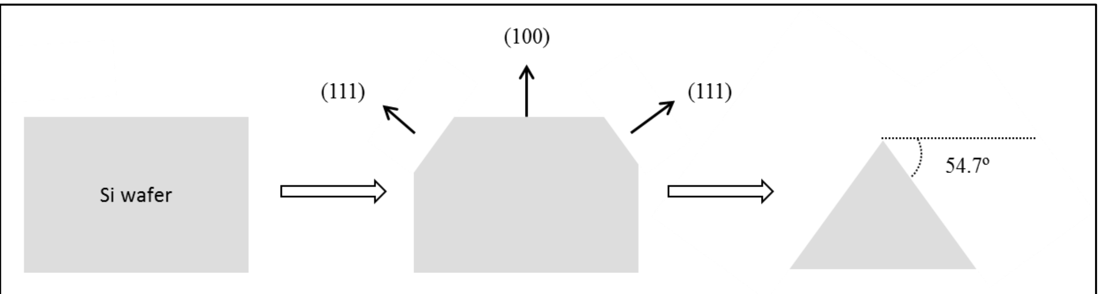

Figure 17: Anisotropic etching

The formation of random pyramids facilitate the incident light to interact with the surface more than once therefore light can be trapped as shown in Figure 18. More interaction with surface refers to increase on the optical path length of incident light with a higher probability of absorption. The heights of the randomly distributed pyramids is generally in the range of 8-10μm [28].

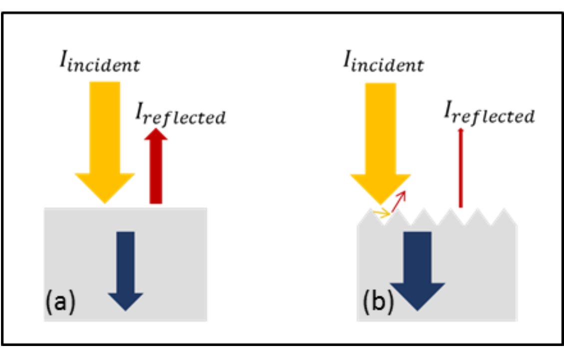

Figure 18: Schematic representation of reflection losses from flat (a) and textured (b) surface

The surface texturing enhances the optical properties of Si solar cell and it is one of the crucial steps for conventional Si solar cell production. On the other hand, it leads the formation of valleys and sharp areas resulting in an increase in effective surface area [29]. In turn, textured surfaces suffer from some drawbacks especially in quality of electrical passivation made by growing a-Si:H layer due to increase in the density of impurities and the crystallographic defects with larger surface area. As an example, the change in the interface defect density (D_{it}) measured by surface photovoltage measurement following RCA cleaning and after formation of pyramids is shown in Figure 19 [30].

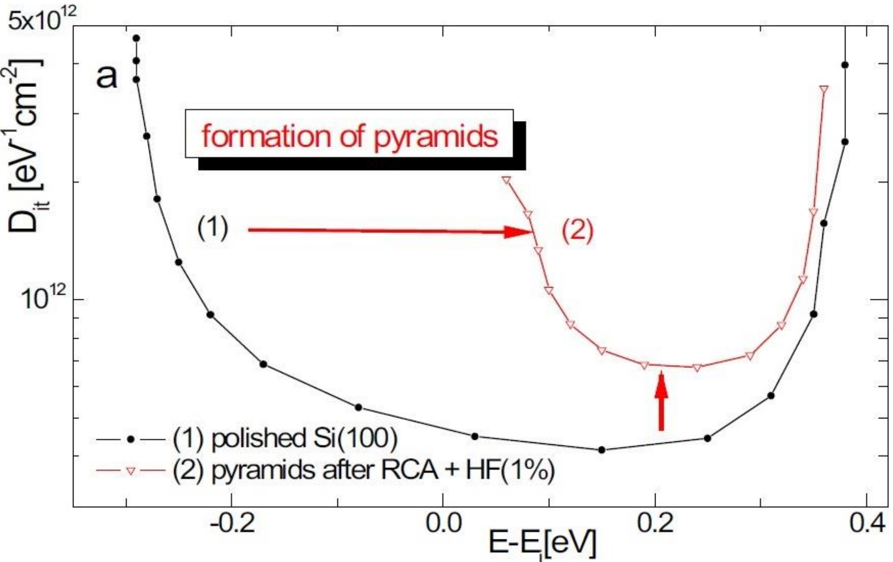

Figure 19: Change in D_{it} (E) on p-type Si surfaces after RCA cleaning and oxide removal during the formation of pyramids [30]

The sharp edges of pyramids behave as the recombination centers for SHJ solar cells which resulting in lower passivation quality because of the induced D_{it}. The lower passivation quality of the textured surfaces could be solved by either decreasing effective surface area with smaller pyramids or polishing the sharp regions of pyramids by additional wet chemical treatments [30-32].

2.2.3. Pyramid Rounding by Wet Chemical Etching

In order to enhance passivation quality of a-Si on textured surfaces, isotropic etchant could be used to round the tips of pyramids. A mixture of hydrofluoric acid (HF) and nitric acid (HNO_3) is one of the widely used solutions. The etching mechanism consists of a couple of reactions as shown in Table 1;

Table 1: Reactions involved during HF/HNO_3 treatment

NO_2 formation	$HNO_2 + HNO_3 \rightarrow 2\ NO_2 + H_2O$
Oxidation of silicon by NO_2	$2NO_2 + Si \rightarrow Si^{2+} + 2NO_2^{-}$
Formation of SiO_2	$Si^{2+} + 2\ (OH)^{-} \rightarrow SiO_2 + H_2$
Etching of SiO_2	$SiO_2 + 6\ HF \rightarrow H_2SiF_6 + 2H_2O$

In this reaction sequence, HNO_3 acts as an oxidizing agent and then the formed thin oxide layer is removed by HF. The etching mechanism of HF/HNO_3 includes electro-chemical reaction oxidization of Si surface which is defined by Gerischer mechanism [33]. Slight differences in the etch rate at areas of sharp edges causes a rounding effect and the etchant also burns out the organic residuals attached on the surface. The rounding etching process is inserted between two successive RCA cleanings [34]. At this point, overetching of pyramids leads to an unexpected increase in surface reflection. For this reason, the tradeoff between electrical gain from passivation and optical losses should be optimized to get higher solar cell performance.

2.3. Amorphous Silicon

Amorphous phase is the most disordered state of material. Si is the member of Group IV-A on the periodic table and forms four bonds. Crystalline Si (c-Si) atoms are arranged in a diamond structure. In contrast to c-Si, a-Si atoms are distributed randomly without any order in a long range as shown in Figure 20. The random and irregular distribution of Si atoms is generally resulted in unbounded valance electron which is called as dangling bonds [35].

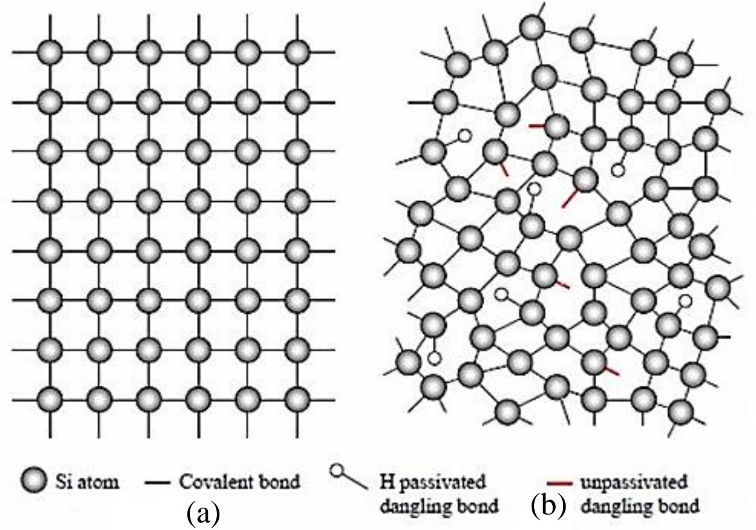

Figure 20: Distribution of Si atoms (a) in crystalline and (b) amorphous form [35]

Dangling bonds behave as recombination centers in the solar cell. In spite of that behavior, dangling bonds could be passivated by Hydrogen with forming a-Si:H layer. For this reason, hydrogen content of a-Si:H layer has a deterministic effect on passivation quality. Inside the a-Si:H layer, hydrogen content could reach up to 40%. The extent of hydrogen content strongly depends on the deposition conditions of a-Si:H layer [36]. The desired Hydrogen concentration in a-Si:H film is around 15-18% to achieve excellent surface passivation [37-38].

2.3.1. Density of States

The density of states (DOS) distribution describes the number of states available to be occupied by an electron in a system. Energy distribution of carriers and carrier concentrations are characterized by DOS distribution. According to semiconductor basic, the valance and conduction bands are continuous throughout the material where electrons in the conduction band and holes in the valance band can move freely. In Figure 21, DOS distributions of c-Si and a-Si are shown respectively.

The irregular structure of a-Si:H results in localization of density states in energy gap. Furthermore, the extent of irregularity is quantified by the degree of localization [39].

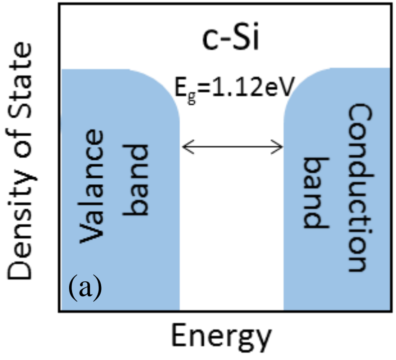

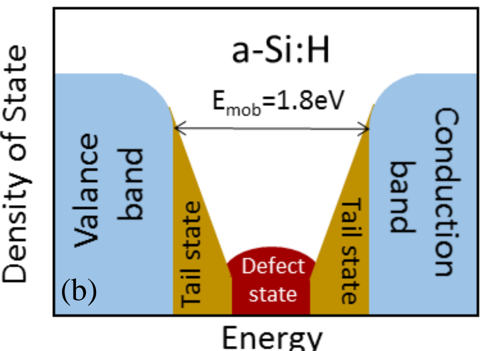

Figure 21: Density of states (DOS) distribution of c-Si (a) and a-Si:H (b)

Due to the defect states of a-Si:H, it is not possible to define a forbidden energy band gap as in c-Si. For this reason, the mobility band gap is defined as the energy differences between tail states (mobility edges) of conduction and valance bands as shown in Figure 21 (b). In other words, the mobility gap can be defined as energy gap between the starting points of sharp decrease in tail states. The mobility gap of a-Si:H is estimated as 1.8 eV which is larger than the energy band gap of c-Si ($E_g = 1.12eV$).

2.3.2. Interface Trap Density

On the surface of the c-Si substrate, the localized energy states exist in the forbidden energy band gap which is called interface trap energy states, due to misalignment through the crystalline lattice structure. The interface trap states are originated from the lattice relaxation on the surface, the impurity atoms inserted to the crystalline lattice, reconstruction, dangling bonds on the surface and the layer covered on the surface of c-Si. The density of interface traps has a significant effect on the electrical and chemical properties in the Si surface and its vicinity.

Due to the high density of free charge carriers in silicon, the interface trap states leads to a space charge region (Q_{sc}) formed within a few atomic layer above the surface. At the interface, the charged surface states form a charged area called interface charges (Q_{it}) as demonstrated in Figure 22. The space charge region is formed under the condition where interface and space charges are equal to each other $Q_{it} = Q_{sc}$ in thermal equilibrium [40].

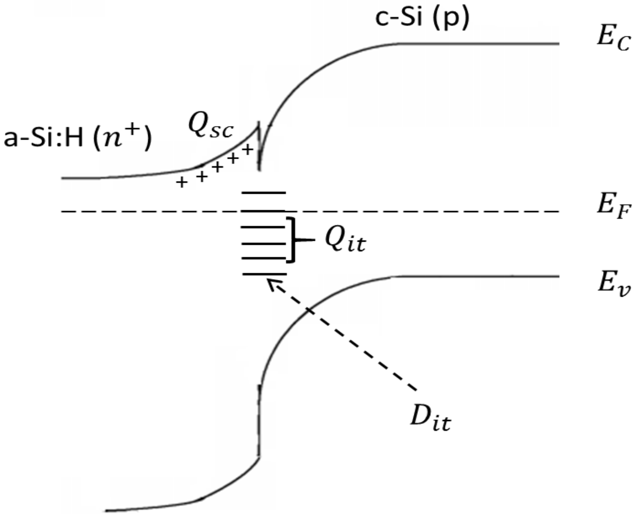

Figure 22: Energy band diagram of the interface between a-Si:H (n+) and c-Si

The density of interface traps (D_{it}) is formulated by the following equation;

$$D_{it}(E) = -\frac{1}{e}\frac{\partial Q_{it}}{\partial E}, \quad \text{(Eq. 2.7)}$$

where the unit of D_{it} is $cm^{-2}eV^{-1}$.

The D_{it} located at the interface between a-Si:H and c-Si has a significant effect on SHJ solar cell performance. Due to the high defect density at the interface (for

values above 10^{11} $cm^{-2}eV^{-1}$), V_{oc} value starts to decrease with respect to increase on the D_{it} as shown in Figure 23, where the behavior at the interface between a-Si:H and c-Si is simulated for various D_{it} values [41].

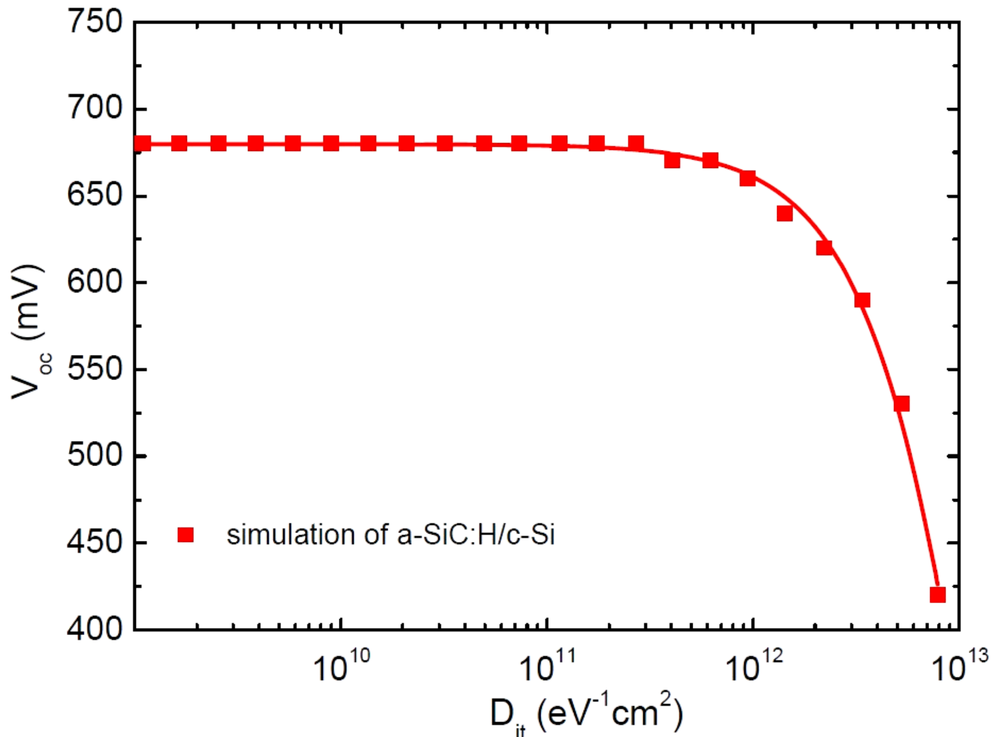

Figure 23: Dependence of the V_{oc} of a SHJ solar cell on the defect state density at the interface D_{it} (E). The D_{it} (E) values at the x-axis represent only the mid-gap defect density [41]

2.3.3. Deposition of Amorphous Silicon

Several deposition techniques are used for the fabrication of a-Si:H layer. The most commonly used technique for fabrication of SHJ solar cell is Plasma Enhanced Chemical Vapor Deposition (PECVD). Plasma is an ionized gas, described as the fourth state of matter. In a typical PECVD system, plasma of reactant process gasses is generated between parallel electrodes (anode and cathode) by using RF, DC or VHF power source. The plasma includes reactive radicals, ions, molecules, neutral atoms

and other excited species. These energized atoms and molecules interact with the substrate surface and the reaction product is deposited as a thin film on the substrate [42]. The PECVD chamber is schematically illustrated in Figure 24. The technique allows deposition of variety types of films on the substrate at a relatively low temperature. The lower deposition temperature in PECVD is one of the major advantages of industrial solar cell production with cost efficiency.

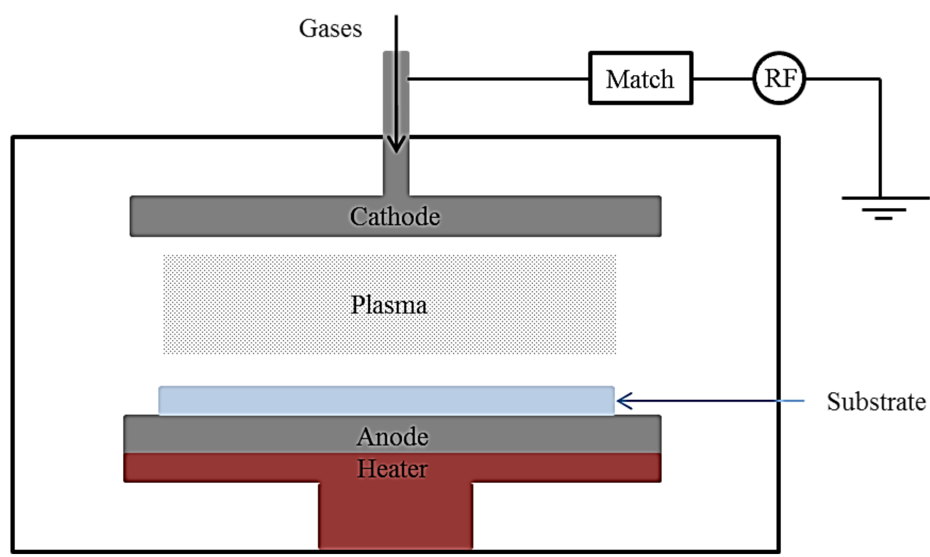

Figure 24: Schematic representation PECVD chamber

For a-Si:H layer deposition, silane (SiH_4) gas is used as the source of silicon and the capacitive coupling between cathode and anode excites SiH_4 gas into the plasma by RF power source, which initiates the deposition on the substrate [36,43]. The ratio of dilution SiH_4 gas and the temperature of substrate are decisive on passivation quality of the deposited a-Si:H layer.

2.3.4. Doping of Amorphous Silicon

To form a p-n junction and change the electrical properties of the semiconductor, the material should be doped intentionally with impurities. For the conventional c-Si solar cell, Group III-A and V-A elements are using as dopants. The impurity atoms take the place of Si atoms inside the crystalline structure with the energy supplied by high process temperature (>800 ºC) [44].

In 1975, LeComber and Spear discovered the ability of doping and controlling electrical conductivity of a-Si:H by using phosphine (PH_3) and diborane (B_2H_6) [45]. However, doping of a-Si was observed to be less efficient compared to that of c-Si. In 1982, the phenomenon behind the lower doping efficiency was explained by Street with the autocompensation model [46]. In that model, it was concluded that due to self-inhibiting nature of doping a-Si, the maximum doping is limited and the doping of a-Si leads an increase in the density of defect resulted in low charge carrier lifetime [47].

2.3.5. Staebler - Wronski Effect

In 1977, Staebler and Wronski discovered the increase in the defect density of a-Si:H after exposing the samples to light, called Staebler-Wronski effect (SWE). They observed a loss analysis for the conversion efficiency of a-Si solar cell with p-i-n (pin) structure over time. However, the SWE can be reversed by heating a-Si:H samples above 150 ºC [48]. Due to SWE, the conversion efficiency of pin solar cells can be degraded up to 30% in the first six months, which is the major disadvantage of a-Si:H solar cells.

2.4. Recombination

When a solar cell is exposed to light, electrons are excited by incident photon to conduction band and they tend to loss their energy and fall back into the valance band again. When an electron in the conduction band is combined with a hole in valance band, the resultant energy is released in various ways. This combination of a conduction band electron with a valance band hole is called as *recombination*. The excess energy does not contribute to energy production of the cell. The rate of recombination is the limiting factor of charge carrier lifetime before being collected. For that reason, recombination is one of the critical characteristics and has a significant effect on the efficiency of solar cell. The relation between recombination rate (R in $cm^{-3}s^{-1}$) and the lifetime (τ in s) as the following equation;

$$R \equiv \frac{\Delta n}{\tau}, \qquad \text{(Eq. 2.8)}$$

where Δn represents excess carrier density (cm^{-3}). For SHJ solar cell, due to discontinuity in the lattice structure between bulk Si and a-Si, a high concentration of dangling bonds exists at the interface where it behaves as a recombination center. The recombination at the interface is called surface recombination (U) and defined as;

$$U \equiv S.\Delta n_s, \qquad \text{(Eq. 2.9)}$$

where S is the surface recombination velocity ($cm.s^{-1}$) and Δn_s is the excess carrier density at the surface. To qualify the surface passivation, generally surface recombination velocity or the effective lifetime (τ_{eff}) is preferred. The effective lifetime is as the following;

$$\frac{1}{\tau_{eff}} = \frac{1}{\tau_{bulk}} + \frac{2S}{W} \quad \text{(Eq.2.10)}$$

Where W is the thickness of the wafer and τ_{bulk} refers the bulk lifetime [6].

Main types of recombination mechanisms are; *Shockley-Read-Hall (SRH), radiative* and *Auger recombination*.

2.4.1. Shockley-Read-Hall Recombination

The Shockley-Read-Hall (SRH) recombination, is the recombination through the defects, involving four various interaction of an electron in the conduction band with a hole in the valance band via trap energy states in the forbidden energy gap. The possible interaction paths are shown in Figure 25.

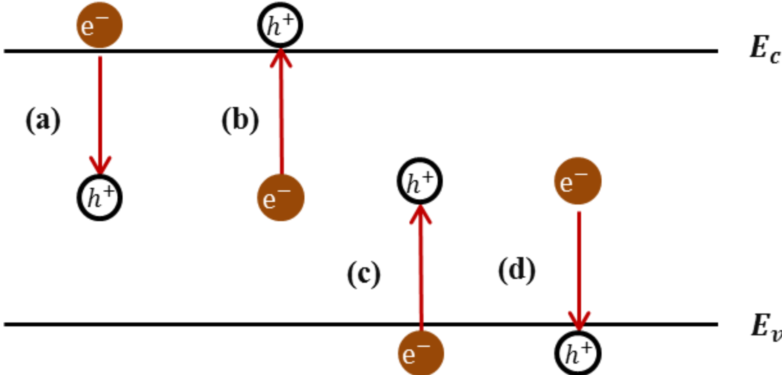

Figure 25: Transitions of SRH recombination (a) capture of electron, (b) emission of electron, (c) capture of hole, (d) emission of hole

For electron transition from conduction band to trap energy state (Figure 25 - a), the rate of electron capture (R_{cn}) is determined by electron density n the conduction band and the density of empty trap states within the bandgap as the following equation;

$$R_{cn} = n.v_{th}.\sigma_n.N_t.(1 - f(E_t)) \qquad \text{(Eq. 2.11)}$$

where n represents the density of an electron in the conduction band, v_{th} is the thermal velocity σ_n is the capture cross-section for electron N_t is the trap state density and $f(E_t)$ represents the Fermi-Dirac distribution of trap energy states. The Fermi-Dirac distribution is defined as the following equation;

$$f(E) = \frac{1}{1+e^{(E-E_F)/kT}} \qquad \text{(Eq. 2.12)}$$

On the other hand $(1 - f(E_t))$ represents the probability of the empty trap states which could be occupied by an electron [49].

In the case of electron emission (Figure 25 – b), the rate of electron emission (R_{en}) is proportional to the number of trap energy states filled by electron as the following equation;

$$R_{en} = e_n.N_t.f(E_t)\,, \qquad \text{(Eq. 2.13)}$$

where the emission coefficient of electron is represented as e_n [49].

The rate of hole capture (R_{cp}) and hole emission (R_{ep}) could be written with an identical approach as the following equations;

$$R_{cp} = p.v_{th}.\sigma_p.N_t.f(E_t), \qquad \text{(Eq. 2.14)}$$

$$R_{ep} = e_p.N_t.(1 - f(E_t)), \qquad \text{(Eq. 2.15)}$$

Above equations, σ_p is the capture cross-section for a hole and e_p is the emission coefficient of a hole [49].

In thermal equilibrium condition, the rate of electron emission to the conduction band and the electron capture from conduction band should be equal to each other.

$$R_{cn} = R_{en} , \qquad \text{(Eq. 2.16)}$$

$$n.v_{th}.\sigma_n.N_t.\left(1 - f(E_t)\right) = e_n.N_t.f(E_t) , \qquad \text{(Eq. 2.17)}$$

From the combination of Fermi-Dirac distribution function with Eq. 2.11, the emission coefficient of electron (e_n) becomes;

$$e_n = n.v_{th}.N_c.\exp(\tfrac{E_t - E_c}{kT}) \qquad \text{(Eq. 2.18)}$$

Using a similar approach, the emission coefficient of hole could be derived as the following equation;

$$e_p = p.v_{th}.N_v.\exp(\tfrac{E_v - E_t}{kT}) \qquad \text{(Eq. 2.19)}$$

Under the non-equilibrium steady-state condition, the net rate of captured electron from the conduction band must be equal to the net rate of holes captured from the valance band with assuming that the emission coefficients are equal under thermal equilibrium condition. Under this assumption, the rate of SRH recombination can be derived as the following equation;

$$R_{SRH} = \frac{\sigma_n.\sigma_p.N_t.(np-n_i^2)}{\sigma_n(n+n')+\sigma_p(p+p')}, \qquad \text{(Eq. 2.20)}$$

where

$$n' = N_c.\exp(\frac{E_t-E_c}{kT}) \quad \& \quad p' = N_v.\exp(\frac{E_v-E_t}{kT}) \qquad \text{(Eq. 2.21)}$$

From the definition of lifetime, due to SRH recombination, the minority carrier lifetime of holes in n-type material and the minority carrier lifetime of electrons in p-type material could be found by;

$$\tau_{SRH,p} = \frac{\Delta p}{R_{SRH}} = \frac{1}{N_t.\sigma_p} \qquad \text{(Eq. 2.22)}$$

$$\tau_{SRH,n} = \frac{\Delta n}{R_{SRH}} = \frac{1}{N_t.\sigma_n} \qquad \text{(Eq. 2.23)}$$

Due to the defective nature of a-Si:H layer, the defect through recombination mechanism (SRH) is dominant on SHJ solar cells.

2.3.2. Radiative Recombination

Radiative recombination known as band-to-band recombination, is the sequence that the excited electron on conduction band falls back to valance band and then recombines with a hole. The resulting energy is emitted as a photon with an equal energy to band gap as schematically demonstrated in Figure 26. The probability of radiative recombination is higher for direct band gap materials where it is less probable for an indirect band gap such as Si. For this reason, the effect of the radiative recombination could be neglected for a material having indirect band gap [50].

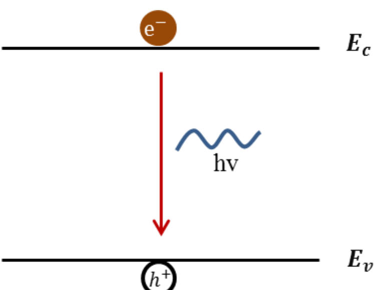

Figure 26: Schematic of radiative recombination

The radiative recombination rate is proportional to excess carrier density as formulated in the following equation;

$$R_{radiative} = B(np - n_i^2), \quad \text{(Eq. 2.24)}$$

where B is the radiative recombination coefficient. For silicon, B is equal to 2.1x10^{-15} where it is several magnitudes of order lower compared to direct band gap materials.

2.4.3. Auger Recombination

The Auger recombination occurs with the interaction of three charge carriers. In contrast to radiative recombination, the excess energy is transferred to other charge carriers as schematically shown in Figure 27.

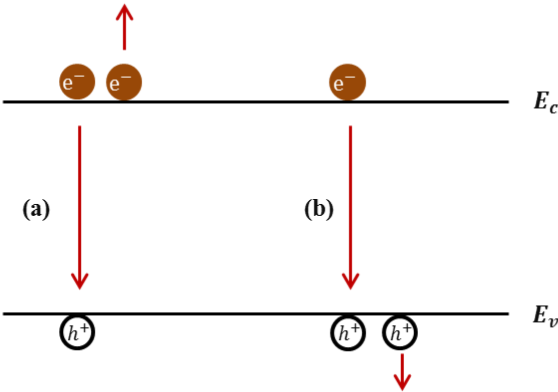

Figure 27: Schematic of the Auger recombination

During the Auger recombination, excess energy is either transferred to electron or hole and the excited third charge carrier releases the gained energy to the lattice by generating phonons and comes back to its original energy state. The rate of Auger recombination is expressed as in the following equation;

$$R_{Auger} = (C_n n + C_p p)(pn - n_i^2) \quad \text{(Eq. 2.25)}$$

where C_n *and* C_p are Auger coefficients for electrons and holes respectively.

The Auger recombination is strongly related with the injection level such that the dominant recombination becomes the Auger recombination for higher injection levels.

Effective Lifetime refers the total effect of all kind of recombination on the bulk and surface of silicon which is described as the following equation;

$$\frac{1}{\tau_{eff}} = \frac{1}{\tau_{bulk}} + \frac{1}{\tau_{s}} = \frac{1}{\tau_{radiative}} + \frac{1}{\tau_{SRH}} + \frac{1}{\tau_{Auger}} + \frac{1}{\tau_{s}} \qquad \text{(Eq. 2.26)}$$

where the bulk lifetime is linked with SRH, radiative and Auger recombination.

2.5. Silicon Heterojunction Solar Cell

In SHJ solar cell technologies, the substrate of the cell is c-Si wafer and it is responsible for carrier transport and absorption of the light. The p-n junction is formed by doped a-Si:H layer with intrinsic a-Si:H layer which leads to a high surface passivation quality.

2.5.1. Structure of an SHJ Solar Cell

The silicon heterojunction solar cell is obtained by depositing intrinsic a-Si:H layers on double side of the textured silicon wafer for passivation and doped a-Si:H layers on top of intrinsic a-Si:H for emitter and back surface field (BSF) formation. Because of the low carrier mobility of a-Si:H, Transparent Conducting Oxide (TCO) is needed to increase the collection probability of charge carriers. Following TCO deposition, the final step is metallization process. Resulting SHJ solar cell structure can be visualized in Figure 28. The rear side of Si wafer is fully covered with metal contact to achieve maximum collection of charge carriers; on the other hand, a grid structure is formed on the front side to allow light to diffuse into the cell. Each deposition steps will be explained in details in Chapter 3.

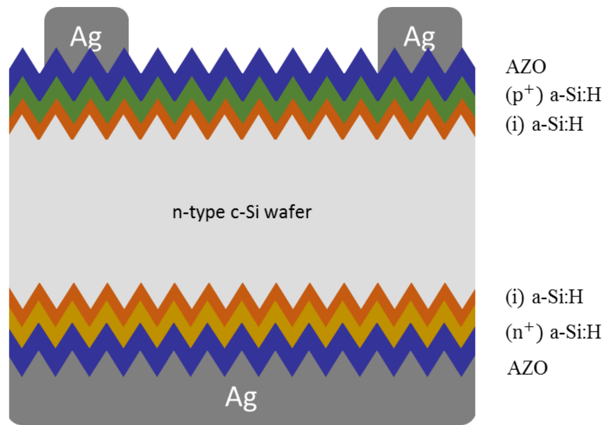

Figure 28: Structure of a Heterojunction Silicon Solar Cell

TCO's are one of the fundamental components of optoelectronic devices. The ideal TCO has metal like conducting properties with an ability of being fully transparent for a wide range of wavelength. Commonly used TCO's are Indium Thin Oxide (ITO) and Aluminum doped Zinc Oxide (AZO) for SHJ solar cell applications.

2.5.2. Structure of Silicon Heterojunction IBC Solar Cell

The novel approach for the design of the solar cells is to localize all metal contacts on the rear side of solar cell with a fully opened front surface which leads to getting more light into the cell. Therefore, emitter and back surface field should be formed on the rear side. Due to the IBC solar cell design, short-circuit current and open-circuit voltage could be improved significantly. In recent years, research groups have been working on various patterning methods for junction and rear contact formation such as utilization of shadow masks [51], lift-off method [52] and etching techniques including both wet and dry etching [53]. The simple structure of SHJ IBC solar cell is illustrated in Figure 29.

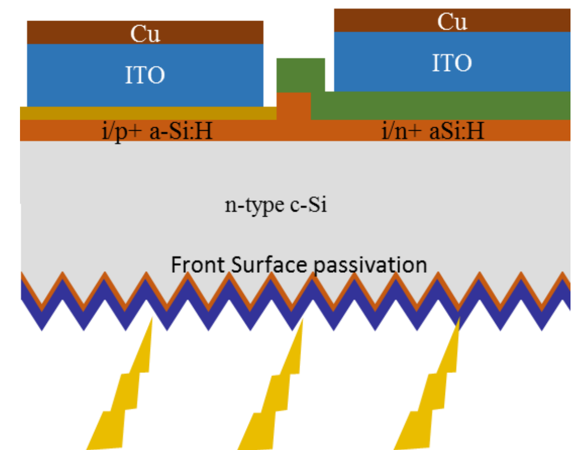

Figure 29: Demonstration of SHJ IBC solar cell

The front side of the wafer is passivated by a-Si:H and coated with a thin dielectric material to enhance absorption of incident light by reducing reflection losses and is called Anti Reflection Coating (ARC). The commonly used material for ARC is SiNx which also provides excellent passivation quality. The rear side of the wafer is passivated by a-Si:H layer. Then p-n junction is formed at rear side via emitter patterning technique. The final process is formation of metal contacts.

Patterning Technique for SHJ IBC Solar Cell

Usage of wet chemicals for etching of a-Si:H is one of the alternative technique with promising results. The method belongs to isotropic selective etching of a-Si:H layer. For this purpose, i/p+ a-Si:H region could be patterned by HF- oxidizing agent such as H_2O_2 and HNO_3 where i/n+ a-Si:H region could be patterned by a selective etchant such as Tetramethylammonium hydroxide (TMAH) [54].

The etching mechanism of HF and HNO_3 has already been explained before as a pyramid rounding step for SHJ solar cell. Addition to this feature, the similar solution could be used for emitter patterning purposes with various concentrations [33].

The etching mechanism of HF and H_2O_2 solution is as following;

Table 2: Reactions occur during HF/ H_2O_2 treatment

Oxidation of silicon	$2H_2O_2 + Si \rightarrow 2H_2O + SiO_2$
Oxide removal	$SiO_2 + 4HF \rightarrow SiF_4 + 2H_2O$
	$SiF_4 + 2HF \rightarrow H_2SiF_6$

In contrast to HF/HNO_3 etchant, the etching mechanism of HF/H_2O_2 consists of purely chemical oxidization reaction. As shown in Table 2, the oxidizing agent is H_2O_2 and formed oxide is removed by HF. The etch rate is strongly depending on doping type of a-Si:H and concentration of mixture [55-56].

TMAH is one of the chemical etchant that used for random pyramid texturing. Besides this property, it is preferred to pattern BSF (n^+ a-Si:H region) at temperatures below 30ºC. Due to its selectivity on boron doped a-Si:H layer, TMAH is used to remove n^+ a-Si:H layer and the etching stops at p^+ a-Si:H region [57].

2.6. Metal Contacts

Metal contacts are one of the noteworthy components of solar cells, where generated charge carriers are collected. The metallization of solar cells could be achieved by a couple of methods such as thermal evaporation, screen printing or sputtering. Depending on the metal and semiconductor that are contacted each other, two type of junction could be formed, (i) Ohmic contact or (ii) Schottky contact.

Ohmic Contact

The junction formed between metal and semiconductor without a potential barrier for the current flow is called Ohmic contact. In a case of forming contact with a n-type semiconductor, the work function of the semiconductor (Φ_S) must be larger than the work function of the metal (Φ_M) to have an Ohmic contact. In other cases for p-type material, $\Phi_S < \Phi_M$. Alternatively, Ohmic contact can be obtained if the underlying

substrate is heavily doped so that the current flow takes place by tunneling independently from the work functions of both sides of the junction.

Schottky Contact

Schottky contacts are formed accompanied by a potential barrier against carrier transport. The potential barrier (Schottky barrier) blocks charge carrier flow in one direction. Schottky barrier is formed if $\Phi_S < \Phi_M$ for n-type semiconductor or $\Phi_S > \Phi_M$ for p-type semiconductor. In the case of heavily doped substrate, depletion region and the Schottky barrier get narrower leading to excessive high tunneling current.

CHAPTER 3

EXPERIMENTAL

The substrate used in fabrication of SHJ solar cell is p-type Czochralski (CZ) Si wafers with a resistivity of 1-3 Ω.cm, a thickness of 200 μm and (100) orientation. The device structure of SHJ and SHJ IBC solar cell has explained in Chapter 2. In this thesis, enhanced surface passivation with pyramid rounding step and a wet etching method for emitter patterning of SHJ IBC has been studied. In Chapter 3, experimental procedures and characterization technique will be explained.

3.1. Fabrication Procedure for SHJ Solar Cell

The fabrication of SHJ solar cell begins with surface preparation including surface texturing for light trapping and surface cleaning by wet chemistry to decrease the density of interface states (D_{it}), thus to provide excellent surface passivation. The process flow of single side SHJ solar cell is illustrated in Figure 30. The general process flow could be divided into two main parts; (i) wet chemical processes and (ii) growth of a-Si:H layers and formation of metal contacts. Wet chemical processes start with random pyramid texturing step and standard surface cleaning to decrease the interface defect density follows. At this stage, pyramid rounding step will be optimized in terms of optical losses and gain in surface passivation.

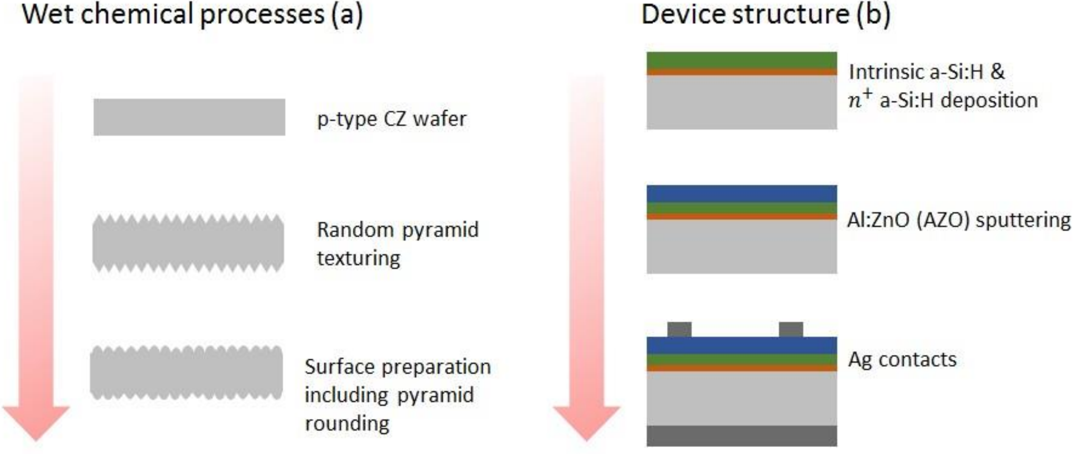

Figure 30: Process flow of SHJ solar cell including a) wet chemical process and b) device structure

Device structure for SHJ solar cell includes deposition of intrinsic (i) and n^+ a-Si stack layers by PECVD and sputtering of AZO. Final step is the formation of metal contacts on both sides of solar cell.

3.1.1. Texturing

The first process of SHJ fabrication is texturing. In GÜNAM cleanrooms, random pyramid texturing was optimized under controlled environment by using wet anisotropic chemical etchant. The optimized texturing solution contains H_2O: IPA: KOH with a respective weight distribution of 91.4%: 4.5%: 4.1%. The solution is prepared in polypropylene container. To start the reaction, the solution is heated up to 75°C and wafers are etched for 40-45 minutes [44]. The textured wafers are dipped into HF: HCl solution to remove oxide on Si wafers and neutralize residues belongings to KOH. The sequence of chemical processes is illustrated in Figure 31.

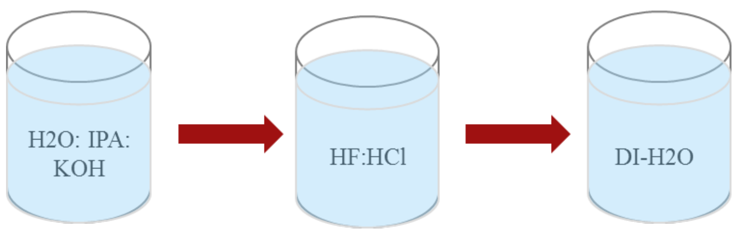

Figure 31: Wet chemical process sequences

After rinsing with DI-H_2O, wafers are dried under nitrogen gas flow which is the last step for the texturing of Si wafers.

3.1.2. Standard Surface Cleaning

Sequences of chemical cleaning processes are adopted in fabrication period of Si solar cells to get ultraclean surfaces. For this purposes, a sequence of RCA-1 (or Piranha) and RCA-2 cleaning procedure is inserted as a standard cleaning procedure in GÜNAM laboratories. RCA-1 and RCA-2 solutions are prepared in specially designed high purity quartz beakers and for each of them, magnetic stirrer is used to mix the solution and get uniform oxidization through whole cassette of wafer. The recipe of RCA-1 used in this study is NH_4OH: H_2O_2: H_2O with volume ratio of 1:1:5 parts. Firstly, NH_4OH and H_2O solution is heated up to 70ºC ± 5ºC and then H_2O_2 is added into the solution. After the chemicals are mixed with the help of magnetic stirrer, wafers are dipped for 10 minutes in the RCA-1 solution. The RCA-2 recipe is HCl: H_2O_2: H_2O volume ratio of 1:1:6 parts. Similar to RCA-1 cleaning, samples are dipped in RCA-2 solution for 10 minutes at 70ºC ± 5ºC.

Before starting cleaning sequence with RCA-1 and RCA-2 solutions, oxide removal of Si wafers is carried out with HF: HCl: H_2O solution with a volume dilution of 1:1:50. Following oxide removal, samples are rinsed under DI-H_2O flow. The process sequence is demonstrated in Figure 32. After each chemical interaction, wafers should be rinsed under DI-H_2O flow to remove chemical residues from surface. It has a crucial effect on blocking the contamination coming through each step. As

mentioned before, RCA-1 & -2 processes oxidize the surface and to remove oxide and get a clean surface HF: HCl dip is needed.

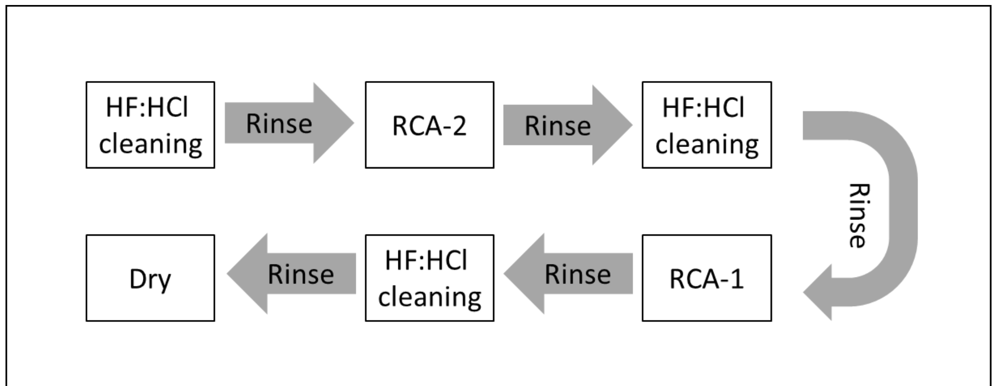

Figure 32: The standard chemical cleaning in GÜNAM

After the last HF: HCl dip, wafers are rinsed and dried under Nitrogen flow which is the final step of cleaning.

The effect of RCA-1 & -2 cleaning on SHJ solar cell results will be investigated in Chapter 4.

3.1.3. Pyramid Rounding Process

Pyramid rounding is an additional step to standard SHJ solar cell fabrication. Since the sharp parts of random pyramids behaves as recombination centers, the rounding step is an alternative way to increase passivation quality of a-Si:H layer. The etchant HF: HNO_3 is applied between two successive RCA cleanings to round randomly distributed pyramids. The process sequence is shown in Figure 33.

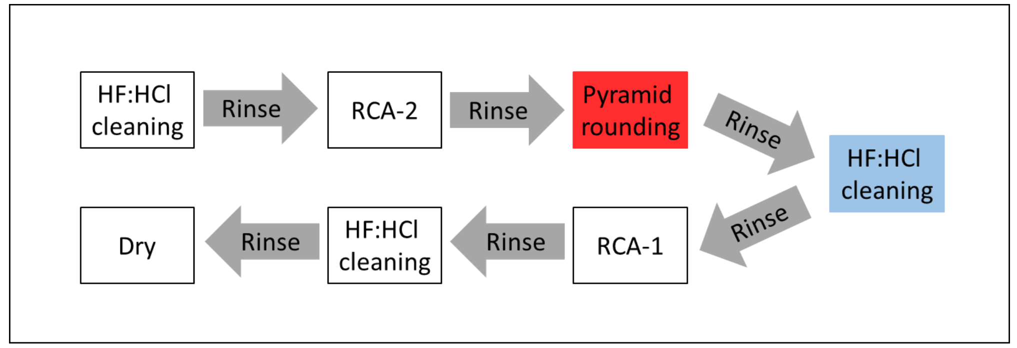

Figure 33: Chemical process flow including pyramid rounding step

The etchant is prepared in polypropylene beaker at room temperature. Various etching times were applied and examined for SHJ solar cells in terms of optical losses and enhanced passivation quality of intrinsic a-Si:H layer. From this point of view, optical losses due to rounding of pyramids should be minimized and electrical gain as a result of enhanced passivation quality should be maximized.

3.1.4. GÜNER Cluster System

GÜNER (Güneş Enerjisi) cluster system, which is produced by VakSis (Vakum Sistemleri) Company, gives opportunity to fabricate a-Si, nano-crystalline Si, micro-crystalline Si and SHJ solar cells without breaking vacuum in between successive depositions. The system is shown in Figure 34. GÜNER cluster system consists of one inductively coupled plasma (ICP) chamber, three separate capacitively coupled plasma (CCP) chambers, one sputtering chamber as schematically illustrated in Figure 35. To fabricate SHJ solar cell, CCP and sputtering chambers are used to grow a-Si:H and AZO layers respectively. The glass substrate with 25x25 cm^2 is used as a holder for c-Si wafer [58].

Figure 34: GÜNER System

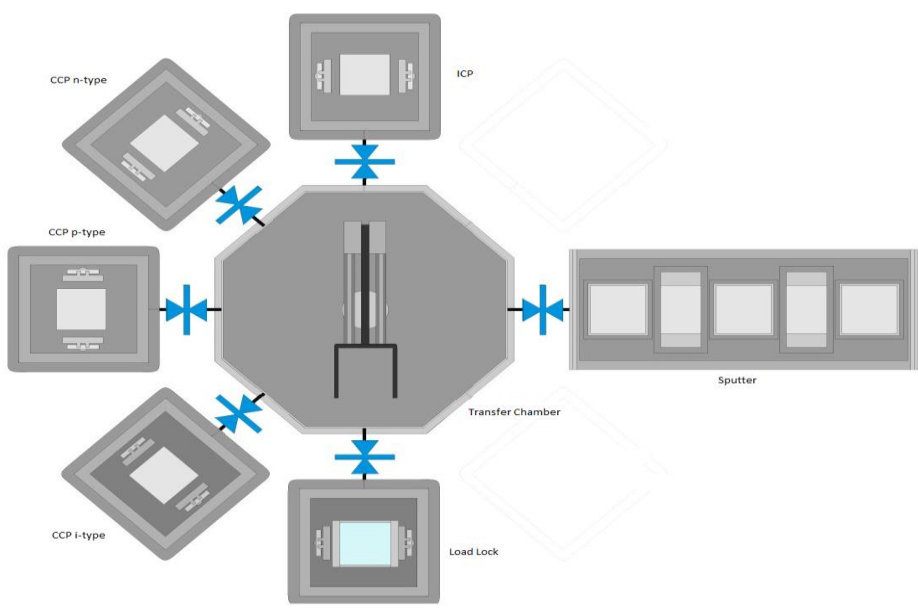

Figure 35: Schematic view of GÜNER System

The first step of device fabrication is placing wafer, which is already cleaned at the beginning of the fabrication sequence using mentioned methods, into load lock on the holder glass. The load lock chamber takes in vacuum with mechanical pumps and the pressure could reach up to 10^{-3} Torr. Except load lock chamber, all other chambers are always kept under vacuum. When the load lock pressure reaches to 10^{-3} Torr, the holder is moved to transfer chamber by a robotic arm. The transfer chamber is always kept under vacuum with 10^{-6} Torr, which is capable of transferring the holder from one chamber to another. The robotic arm could move in backward and forward directions and rotate 360° inside the transfer chamber. When the holder is placed into transfer chamber, it is ready to move to all other chambers.

In the fabrication of SHJ solar cell, CCP is generally used for deposition of a-Si:H including i, p and n a-Si:H layers.

3.1.5. CCP Chambers

CCP is one of the strongest and commonly used design for deposition of a-Si:H layers. In GÜNER cluster system, three CCP chambers are adopted for growing various kind of a-Si:H. All CCP chambers are connected to transfer chamber and have mechanical and turbo pumps. As illustrated in Figure 36, each chamber is used for deposition of a specific type of Si:H layer; either n, or p, or i a-Si:H. Using separate chambers for each layer has a great impact on blocking contamination coming through various doping agents.

The power supply used in CCP chambers is radio-frequency (RF) at 13.56MHz with a maximum power output of 600W. Between anode and cathode, plasma is formed and depending on inlet gasses, the thin film is deposited on the substrate.

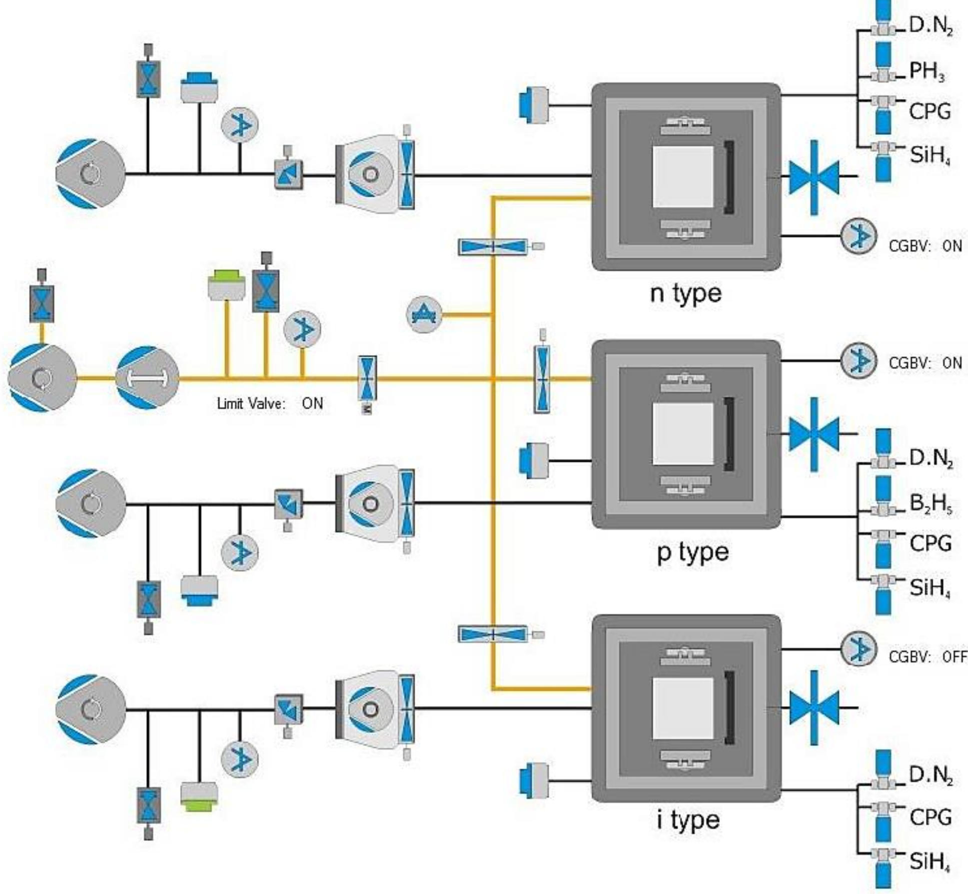

Figure 36: Schematic view of CCP chambers

The gas entrance is from the cathode side with a shower head design. The heater is located at the anode side in order to control deposition temperature. Each CCP chamber has a separate gas line. Common process gases are He, H_2, NH_3, CH_4, C_2F_6, NF_3 that are connected to all chambers due to several purposes such as plasma cleaning, dilution of the process gases and etc. In addition to these gases, SiH_4 gas inlet exists for all CCP chamber as common deposition gas. Besides that, B_2H_6 gas inlet is connected only to p-type CCP chamber whereas n-type CCP chamber has only PH3 gas inlet for doping.

During deposition, turbo gate valves are closed and the pressure is controlled by the throttle valve to reach at desired vacuum level through common line. The

process gasses are burned before releasing to atmosphere in the exhaust system which is connected to common line.

3.1.6. Sputtering

Sputtering technique is extensively used into deposition of metals, alloys and insulators. In sputtering technique, atoms from a specific target are ejected with bombarding of high energetic ions and released atoms are deposited on the surface of substrate. The sputtering chamber consists of two different targets. The first one is silver (Ag) and the other one is AZO. Between heaters, targets are located as illustrated in Figure 37. In contrast to CCP chambers, heaters are located on top of the substrate. Another robotic arm operates inside the sputtering chamber to move the substrate in lateral direction below the targets. During sputtering, lateral oscillation like movement of robotic arm below the target makes growth more uniform in terms of film thickness. The power supply is RF source at 13.56MHz with 5kW. Noble gas argon is used as the source of energetic ions to bombard the target material.

Figure 37: Schematic view of the sputtering chamber

3.1.7. Metallization

Thermal evaporation is one of the widely used Physical Vapor Deposition (PVD) techniques to form metal contacts. The system used for thermal evaporation, which is schematically shown in Figure 38, basically consists of vacuum chamber, pump, holder, power supply and resistive boat. Depending on the material to be evaporated, either a resistive filament or a boat could be used to place and heat the source material. The desired material is placed in the boat or filament. Electrical resistance heats the boat and metal melts under high vacuum. Vacuum allows melted metal vapor to rise and reach to surface of substrate without scattering or reacting with other atoms in the chamber. For thermal evaporation, desired vacuum level is typically below $4.0x10^{-4}$ Torr.

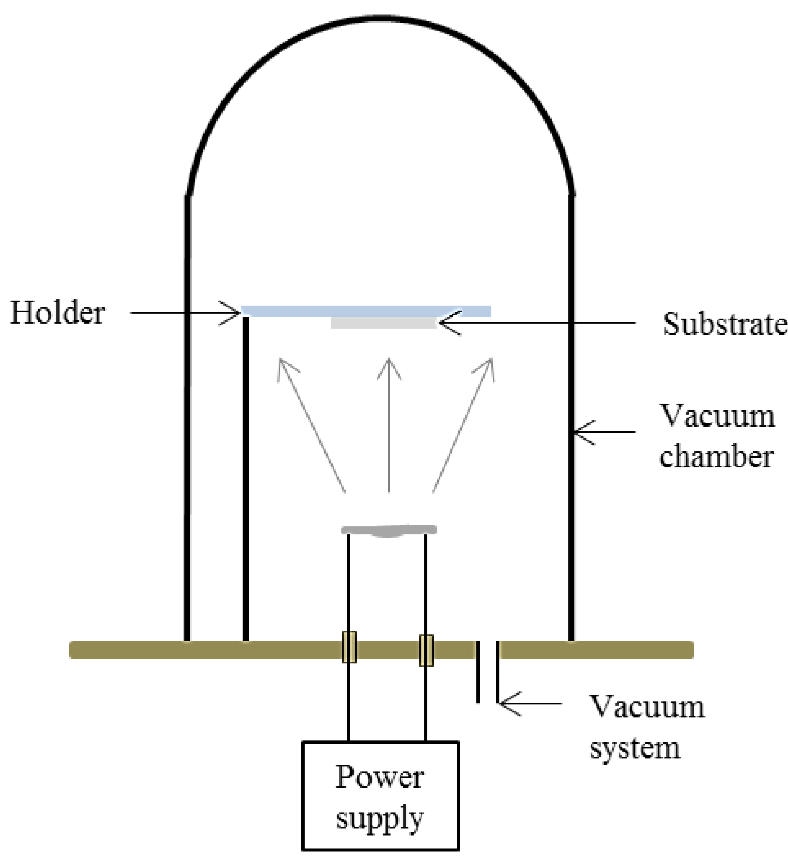

Figure 38: Thermal evaporation system

3.1.8. Thermal Treatment

For SHJ solar cells, post-annealing treatment is needed to eliminate sputter damages induced during the AZO deposition and to get favorable metal contacts. In GÜNAM clean room two annealing system is under use. The first tool used during the experiments works under atmosphere ambient and maximum temperature is 250ºC and it is produced by Nüve Laboratory and Sterilization Technologies.

The second tool is Rapid Thermal Annealing (RTA) system, which is capable of heating the substrate up to 1200°C in a several seconds. The RTA system is produced by AnnealSys. A quartz tube is installed inside the furnace. The halogen lamp, which is located around quartz tube, heats the substrate. The cooling of substrate is achieved by water flow around quartz. The system is shown in Figure 39.

Figure 39: AS-Micro RTA System

3.1.8. Characterization Techniques

3.1.8.1. I-V Measurements

To analyze and characterize the fabricated solar cells, I-V measurements is the most common method. The measurement is conducted by New Port Solar Simulator. Under illumination of A.M. 1.5, current characteristic of solar cell is measured with respect to applied voltage. The solar cell efficiency, open circuit voltage, short circuit current, fill factor, series resistance and shunt resistance could be calculated from the results of measurement.

3.1.8.2. Suns-V_{oc} Measurements

Suns- Voc measurement system produced by Sinton Instruments, is another extensively used characterization technique for solar cells and it is operating principle very similar with I-V measurements. In this technique, open circuit voltage value of solar cell is monitored under decay in illumination intensity as shown in Figure 40.

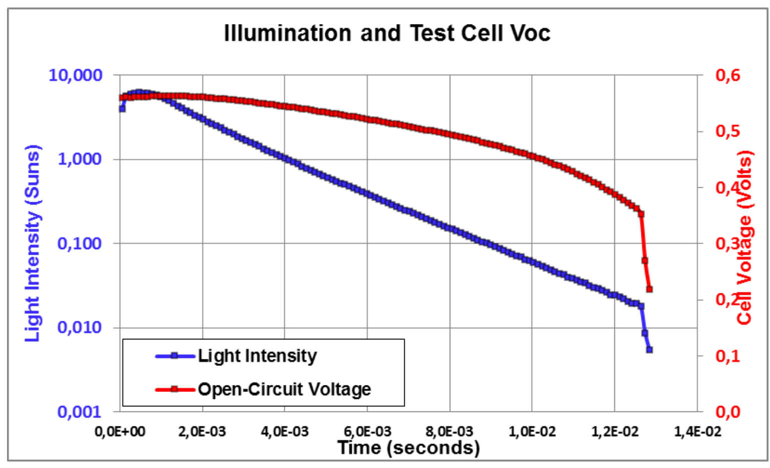

Figure 40: Light intensity and VOC as a function of time

A flash lamp is used as source of incident light. The series resistance effect is eliminated with providing I-V curve of solar cell in Suns-V_{oc} measurements. In other words, it is assumed that zero series resistance through the solar cell. The effect of series resistance is eliminated by following equation,

$$J_{imp} = J_{SC}\left(1 - \frac{I_{ill}}{I_{ill}(1sun)}\right) \quad \text{(Eq. 3.1)}$$

where $\frac{I_{ill}}{I_{ill}(1sun)}$ is the normalized light intensity, J_{imp} is the implied current density and J_{SC} is the current density which is an input value for Suns-V_{OC} measurement. Implead current density is determined for each V_{OC} value as a function of normalized density. From this relation, pseudo J-V curve can be obtained with eliminating series resistance. The equivalent circuit model of Suns – V_{OC} measurement is schematized in double diode representation of solar cell as shown in Figure 41.

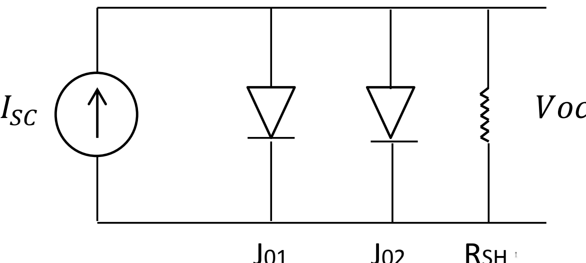

Figure 41: Double diode representation of Suns-VOC measurement

The double diode equation is modified under zero series resistance to obtain reverse saturation currents. The double diode equation is shown in the following equation;

$$J = J_{01}\left(\exp\left(\frac{(q(V-JR_S)}{n_1kT}\right)-1\right)+J_{02}(\exp\left(\frac{(q(V-JR_S)}{n_2kT}\right)-\frac{V-JR_S}{R_{SH}} \quad , \qquad \text{(Eq. 3.2)}$$

where n_1 and n_2 are the ideality factor of the shown diodes in Figure 41, respectively. In ideal case, n_1 is equal to 1 and n_2 is equal to 2. When the series resistance is eliminated, the double diode equation is modified as the following equation;

$$J_{Sun} = J_{01}\left(\exp\left(\frac{qV}{n_1kT}\right)-1\right)+J_{02}(\exp\left(\frac{qV}{n_2kT}\right)-\frac{V}{R_{SH}} \quad , \qquad \text{(Eq. 3.3)}$$

where n_1 is set to one. J_{01}, J_{02} and n_2 values are obtained by least-squares method from Suns – VOC data [59]. From this unique technique, pseudo efficiency, pseudo fill factor, n_1, n_2, reverse saturation current in bulk (J_{01}) and in depletion region (J_{02}) could be obtained. The reverse saturation current in depletion region is one of the deterministic parameters of passivation quality in SHJ solar cell.

3.1.8.3. Reflection Measurements

Reflection measurement is generally used to characterize optical performance of random pyramid texturing and anti-reflection coating. In GÜNAM laboratories, the set-up used in reflection measurements is consisted of a halogen lamp, chopper, diaphragm, lens, integrating sphere, monochromator and detector. In this set-up, the reflection could be measured in the wavelength range from 350nm to 1100nm. In order to calibrate measurements, a $BaSO_4$ disc is used with 100% reflectivity. The experimental set-up is schematized in Figure 42.

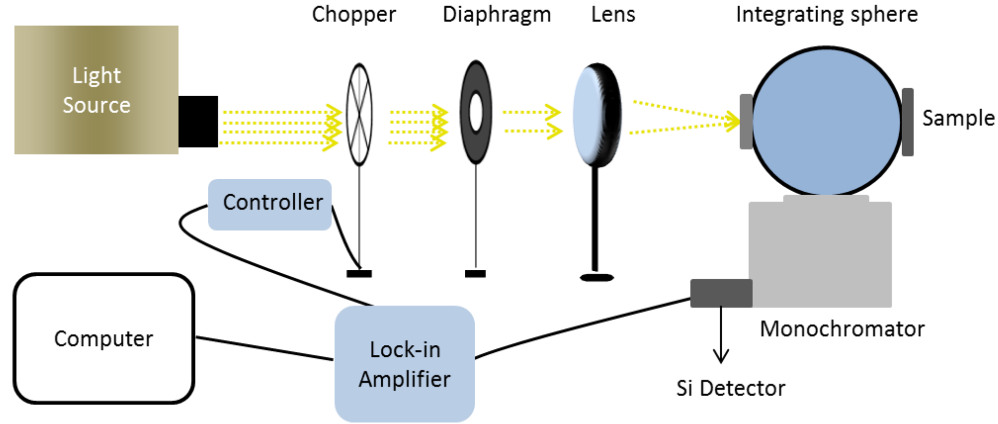

Figure 42: Schematic view of reflection set-up in GÜNAM

3.1.8.4. External Quantum Efficiency Measurements

External quantum efficiency is a technique used to get information about quality of junction and recombination mechanisms of solar cells. In this technique, the ratio of generated charge carriers to the number of incident photons is measured as a function of wavelength. In GÜNAM laboratories, the set-up used in external quantum efficiency is consisted with a halogen lamp, chopper, lens, monochromator and current amplifier. The QE set-up is schematized in Figure 43.

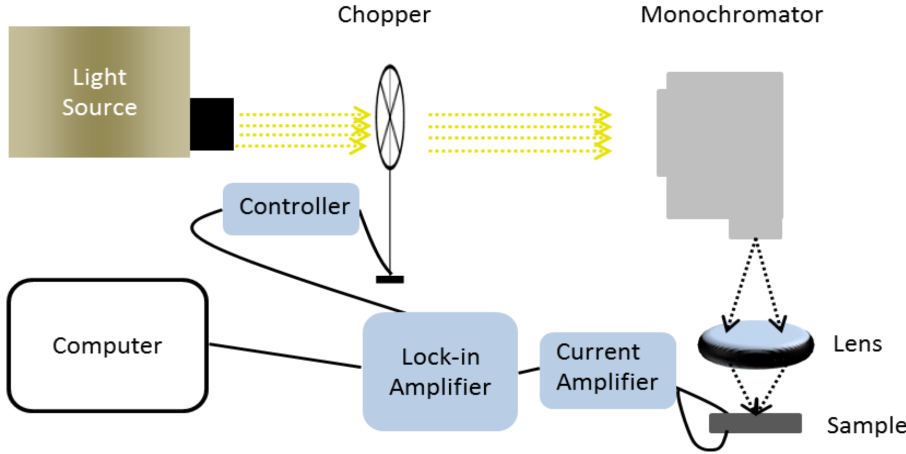

Figure 43: Schematic view of QE set-up in GÜNAM

3.1.8.5. Sheet Resistance Measurements

Sheet resistance measurements, which are done by JANDEL-RM3-AR four point probe, are carried out to determine the resistivity of AZO layers. To optimize and characterize the post-annealing effects on AZO layer, this measurement technique is used.

3.1.8.6. Scanning Electron Microscopy (SEM) Measurements

SEM measurement is crucial to understand surface morphology after random pyramid texturing and pyramid rounding steps. The SEM images are taken by QUANTA 400F Field Emission SEM in Central Laboratory at Middle East Technical University.

3.2. Experimental Procedure for SHJ IBC Solar Cells

The SHJ IBC solar cells are fabricated and characterized in IMEC PV cleanroom facilities at Belgium in i^2 module group. In this study, chemically polished 6inch n-type FZ wafers are used as substrate with 2-4ohm.cm resistivity and 200µm thickness. In IMEC's i^2 Module concept, SHJ IBC solar cells are fabricated on epitaxially grown thin foils [54]. The front surface passivation and rear side emitter formation are crucial steps which yields high efficient SHJ solar cell by improving surface passivation and optical loss with IBC concept. Instead of epifoils, n-type FZ Si wafers are used as substrate to investigate surface passivation quality and to optimize emitter patterning method. The fabrication process flow and device structure are shown in Figure 44. The fabrication starts with standard IMEC clean for surface preparation purposes. Then, the front surface is passivated by a-Si:H/SiN_x stack layer and rear side junction are formed by depositing p^+ a-Si:H layer. At this point, a wet

chemical etching method is investigated to pattern p^+ a-Si:H layer where details and optimization of emitter patterning will be explained particularly in Chapter 4. Several lithography steps and chemical etchings are applied through emitter and BSF formation.

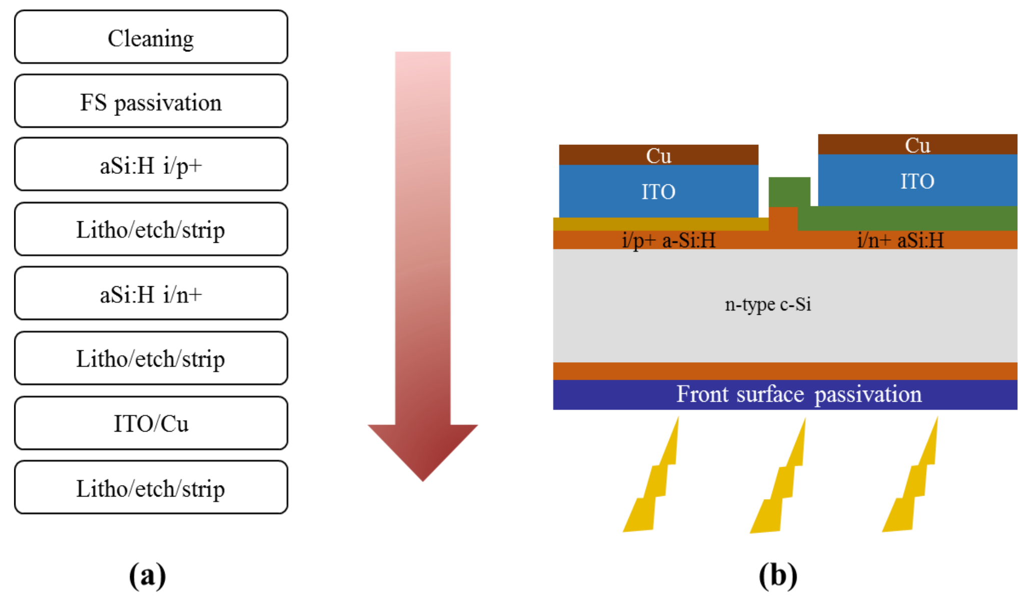

Figure 44: Fabrication process flow for SHJ IBC solar cell (a) and device structure (b)

3.2.1. Surface Preparation

Surface preparation includes successive chemical cleaning steps before applying passivation to the surface. A sequence of cleaning called “IMEC CLEAN” includes two cleaning mixture [60]. The first step is preparation of Sulfuric Peroxide Mixture (SPM) which is also known as Piranha solution. SPM consists with sulfuric acid and hydrogen peroxide (H_2SO_4: H_2O_2) with a volume ratio 4:1. After SPM treatment for 10 minutes, wafers are rinsed under DI-water to remove chemical residues. Similar with RCA-1 and RCA-2 cleanings, SPM oxidizes the surface of Si. For this reason HF: HCl: H_2O treatment with a volume ratio of 1:1:20 is needed to

remove thin oxide layer from surface of Si wafer. After rinsing under DI-water, the second cleaning mixture RCA-2 is prepared as explained before. After the last HF: HCl: H_2O treatment, wafers are rinsed and dried.

3.2.2 Front Surface Passivation

When the surface preparation is finished, Si wafers are ready for passivation procedure. In IMEC Cleanrooms, two PECVD systems with CCP reactors with RF at 13.56MHz are used for front surface passivation purposes. The working principle of these systems is almost similar with the GÜNER System. The AK1000 In-line system from Roth & Rau [61] is used for deposition of i, p^+ and n^+ a-Si:H layer depositions. The Plasmalab system 100 from Oxford Instruments [62] is used for SiN_x and i a-Si:H layer passivation. For deposition of each layer, the optimized deposition parameters are used to get high passivation and junction quality. After cleaning, various passivation layers are grown on the front surface of wafers by PECVD systems. Then, emitter is formed on the rear side of wafers where i/p^+ a-Si:H stack layer is used as emitter. At this stage, the quality of passivation is controlled by coupled lifetime tester. Emitter layer is patterned via etching of i/p+ a-Si:H layer by wet chemical etching and photolithography steps.

3.2.3. Emitter Patterning

Formation of emitter and BSF is the most decisive part for SHJ IBC solar cell. In IMEC i^2 module group, couple of approaches is used for this purpose; one is emitter patterning via either chemical etching or plasma etching, other one is lift-off approach via patterning of SiO_x or SiN_x sacrificial layer. In this thesis, emitter patterning via chemical etching is focused on due to passivation performance of etched surfaces. For this reason, a couple of etchants are used for etching of i/p^+ a-Si:H layer. After passivation of front and rear side of Si wafers, front side is protected by photoresist

and rear side (emitter side) is etched via various etchants. Then, the photoresist is stripped of and etched surface of the wafer is cleaned by RCA-1 solution at 35ºC and rinsed under DI-water flow. Before i/n^+ a-Si:H layer growth for BSF formation, the last HF:HCl:H_2O is performed to remove oxide belongs to RCA-1. Deposition of i/n^+ a-Si:H is performed in AK1000 with optimized deposition parameters in IMEC. When BSF is formed, successive chemical processes are done in a sequence as patterning via photolithography, selective etching of i/n+ a-Si:H layer and stripping of photoresist. For etching of i/n+ a-Si:H layer, Tetramethylammonium Hydroxide (TMAH) solution, which is selective etchant for p doped a-Si:H layer, is applied at room temperature with a volumetric ratio in DI-water 1:12 [57]. The patterning process of both emitter and BSF regions should be designed in a way to avoid overlapping of different regions.

3.2.4. Metallization

On top of the patterned a-Si:H layer, TCO and metal contacts are deposited. Indium Thin Oxide (ITO) layer is sputtered as the TCO layer with covering both emitter and BSF regions. Furthermore, the metal contact is deposited by e-beam evaporation of Copper (Cu). Photolithography and chemical etching of ITO and Cu is integrated into fabrication process to remove overlapping regions between emitter and BSF where overlapping regions causes leakage current due to decrease on shunt resistance.

3.2.5. Characterization

Despite the characterization techniques explained before, effective lifetime measurements is widely used to obtain information about the quality of passivation. To measure effective lifetime of a passivated Si wafer, there are techniques existing such as Quasi-Steady-State Photoconductance decay (QSSPC) [63].

A schematic representation of QSSPC set-up with calibrated lifetime imaging is shown in Figure 45. In IMEC Cleanrooms, BT Imaging set is used to get photoluminescence (PL) and calibrated lifetime PL images [64]. From this measurement, uniformity and quality of the passivation could be obtained.

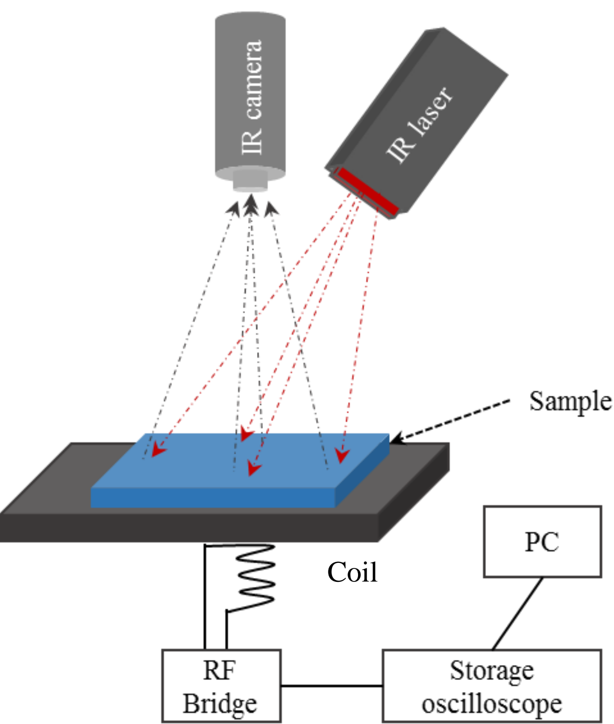

Figure 45: Schematic representation of BT imaging system

The minority carrier lifetime τ_{eff} could be generalized by analysis of QSSPC data as the following equation;

$$\tau_{eff} = \frac{\Delta n(t)}{G(t) - {}^{d\Delta n(t)}/_{dt}} \quad , \qquad \text{(Eq. 3.4)}$$

where $\Delta n(t)$ is the time dependent excess minority carrier concentration and G (t) is the generation rate of excess carrier. Furthermore, PL imaging is simply calculated by steady state technique as defined following equation;

$$\tau_{eff} = \frac{\Delta n}{G} . \qquad \text{(Eq. 3.5)}$$

CHAPTER 4

RESULTS & DISCUSSION

4.1. Silicon Heterojunction Solar Cell Process Optimization

Process steps, depositions and characterization techniques of a SHJ solar cell have already been explained in previous chapters. In this chapter, the effect of surface preparation and dependency of i a-Si:H deposition parameters on solar cell performance are investigated.

The single side SHJ solar cell structure without i a-Si:H between c-Si and n^+ a-Si:H was chosen to clarify the effect of surface cleaning and pyramid rounding process on the solar cell performance. The main ideas behind the chosen structure are to simplify process steps and to optimize the preliminary surface preparation processes. The surface preparation processes involve wet chemical surface cleaning, rounding of sharp edges and hydrogen termination of dangling bonds. The structure of single side SHJ solar cell is shown in Figure 46.

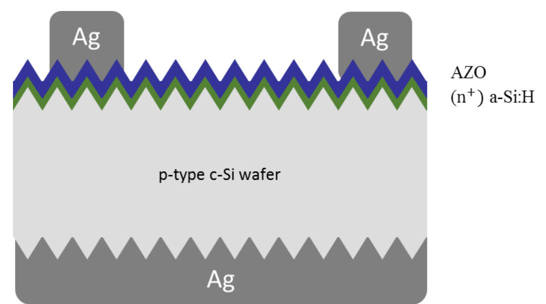

Figure 46: The structure of the SHJ solar cell

The p-type CZ Si wafers with 1-3 Ω.cm resistivity were used as the substrate of this study. Single side SHJ solar cells were fabricated on 2x2 cm^2 Si wafer. The front view of fabricated solar cell with finger-busbar configuration is shown in Figure 47.

Figure 47: The front view of fabricated single side SHJ solar cell

The optimized deposition parameters for n^+ a-Si:H layer are given in Table 3 [58]. Throughout whole study the optimized deposition parameters of n^+ a-Si:H were applied for the fabrication of SHJ solar cells. The sputtering conditions of AZO film was kept constant as RF power at 400 W, deposition pressure at 3 mTorr and Argon flow rate at 125 sccm,), which results in 80nm thick AZO layers.

Table 3: Optimized deposition parameters of n+ a-S:H layer

Deposition time (s)	F_{SiH4} (sccm)	F_{PH3} (sccm)	N_{PH3}/N_{SiH4}	Pressure (Torr)	Power (W)	Substrate Temperature (ºC)
160	200	50	0.05	1	50	180

The thickness of metal contacts was kept constant at 500nm for whole study with the help of thickness monitor placed in thermal evaporation system. The c-Si hard masks were used for the formation of front contacts. After evaporation of Ag, the fabricated solar cells were annealed under atmosphere at 180°C for 20 minutes to

minimize sputtering defects and get a good quality contact between metal and c-Si on rear side.

Before introducing results, it would be beneficial to clarify relation between surface passivation and solar cell parameters. The depletion region is located at the interface between a-Si:H layer and c-Si substrate for SHJ solar cell. For this structure, surface passivation means that passivation of dangling bonds at the interface. The surface passivation improves the effective lifetime resulting in relatively low reverse saturation current (I_0) especially at the depletion region (I_{02}). Considering the solar cell parameters, V_{OC} is strongly dependent on I_0. In other words, V_{OC} values should be increased relatively for passivated samples. On the other hand, I_{SC} value is improved relatively low for passivated samples. On this point, the passivation quality of sample could be understood from either V_{OC} value of solar cell or effective lifetime measurement.

4.1.1. Wet Chemical Cleaning

The first study conducted for SHJ solar cell was insertion of the sequence of RCA clean into available fabrication procedure. Formerly textured wafers were used as substrates for solar cells. In total 8 SHJ solar cells with an area of $4cm^2$ were fabricated, from 4 of which were exposed to RCA cleaning and combined with others in the last oxide removing step by HF: HCl (2%: 2%) cleaning. Then, n^+ a-Si:H layer with 10-15nm thickness and AZO were deposited in GÜNER cluster system. After formation of metal contacts, I-V measurements were conducted under illumination. After post-annealing of solar cell at 180°C, I-V measurements were done and results are shown in Table 4.

Table 4: I-V measurement results of solar cell with and without RCA clean

Sample	V_{oc} (mV)	J_{sc} (mA/cm^2)	FF (%)	R_S (Ω)	R_{SH} (Ω)	ɲ (%)
The best w/o RCA clean	407	24.86	38.30	2.23	17.34	4.85
Average w/o RCA clean	404	24.22	36.30	2.52	15.67	4.34
The best with RCA clean	456	24.95	44.19	1.91	33.24	6.29
Average with RCA clean	434	24.84	41.43	1.89	28.62	5.63

Results show that the main contribution on the efficiency increase is arising from increase in Voc and FF values. As mentioned earlier, the improvement in V_{OC} value is directly proportional to improved surface quality by removing impurities with the help of RCA clean. It is understood from comparison of the best results with and without RCA clean, the enhancement on efficiency is more than 1%. J-V graph of the best solar cell with RCA clean before and after annealing is shown in Figure 48.

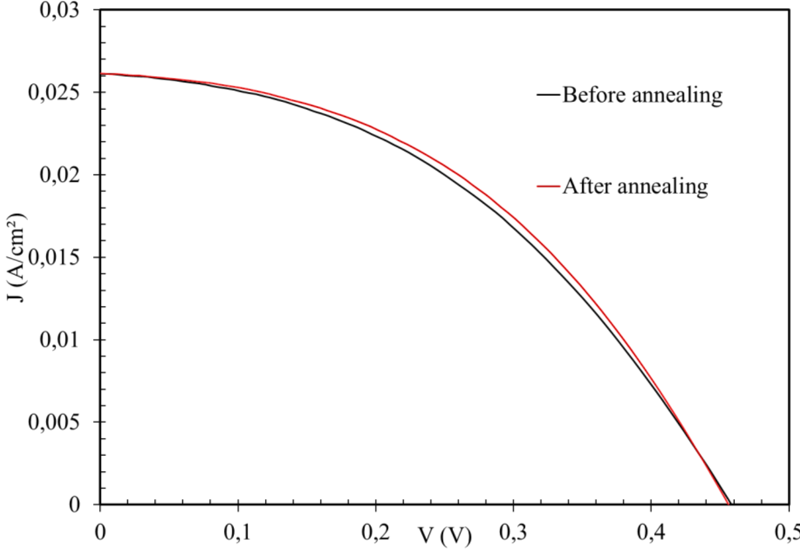

Figure 48: J-V graph of the efficient solar cell with RCA clean

It is worth mentioning that as clearly seen from Figure 48 and results, the problematic parts are passivation quality and leakage current that results in low shunt resistance and it is valid for all solar cell results. To clarify the problem exhaustively, Suns-V_{oc} measurements were conducted and results are listed in Table 5.

Table 5: Suns-V_{oc} results of solar cell with and without RCA clean

Sample	V_{oc} (mV)	J_{01} (mA/cm^2)	J_{02} (mA/cm^2)	Pseudo η (%)
The best without RCA clean	430	1.8×10^{-11}	1.0×10^{-5}	9.3
The best with RCA clean	480	6.1×10^{-11}	3.7×10^{-6}	10.8

The dominant term influencing J_0 value is J_{02} term, which refers to reverse saturation current in depletion region. For SHJ solar cells, depletion region is formed between c-Si and n^+ a-Si:H layer as explained in Chapter 2. J_{02} values strongly depend on D_{it} resulting in defects through recombination in depletion region. Suns-V_{oc} results show that to get excellent SHJ solar cell, the surface passivation quality should be increased, which will result in higher V_{oc} and lower J_{02} and will reduce recombination in depletion region. The dominant recombination basis belongs to SRH recombination. The formation of random pyramids leads to increase in interface defect density as discussed in Chapter 2. In order to improve recombination behavior of pyramids, the next step is to increase passivation quality by optimizing and adding chemical rounding of random pyramids into cell fabrication.

4.1.2. Pyramid Rounding

The pyramid rounding process is inserted between two successive RCA cleans. The optimization of rounding tips of pyramids is divided in to two subtopics; (i) optical loss analyses and (ii) passivation quality analyses. To analyze optical loss, random

textured wafers were exposed to HF: HNO_3 (1:15) mixture at room temperature for various etching time. Reflection measurements were conducted on the etched samples. The reflection results are shown in Figure 49.

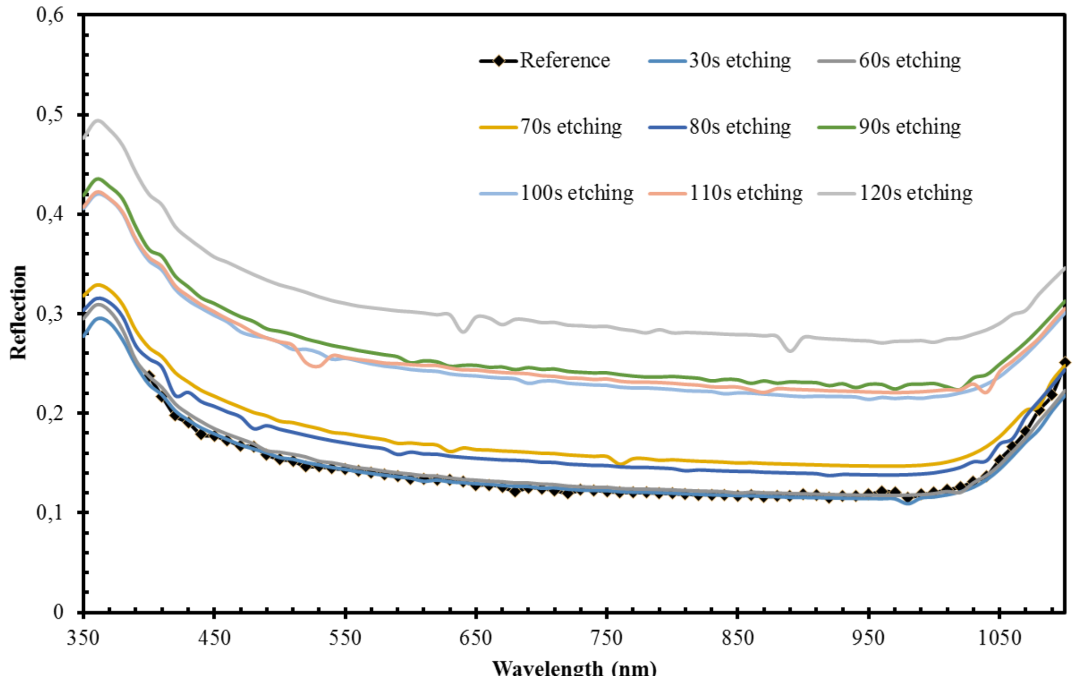

Figure 49: Reflection results of etched samples

Reflection results show that the increase on the reflection value of 80s etching is less than 2%. However, there is a sharp rise on the reflection results after 90s etching. Because of relatively significant increase in reflection, it is not suitable to do etching more than 90 seconds where the reflection is raised by more than 10%. Moreover, the pyramidal surface has roughly become almost optically flat in terms of reflection value where the flat Si surface has around 40% reflection. On the other hand, below 60s etching, the variation of reflection is less than 1%. In terms of optical loss analyses, pyramid rounding process could be adapted to solar cell fabrication for etching durations below 60 seconds. Moreover, the etch rate of the mixture is calculated as 1.5µm/min with using differences on the weight of Si wafer. Before integration of the

method, surface morphology of Si wafers was investigated by SEM images as shown in Figure 50.

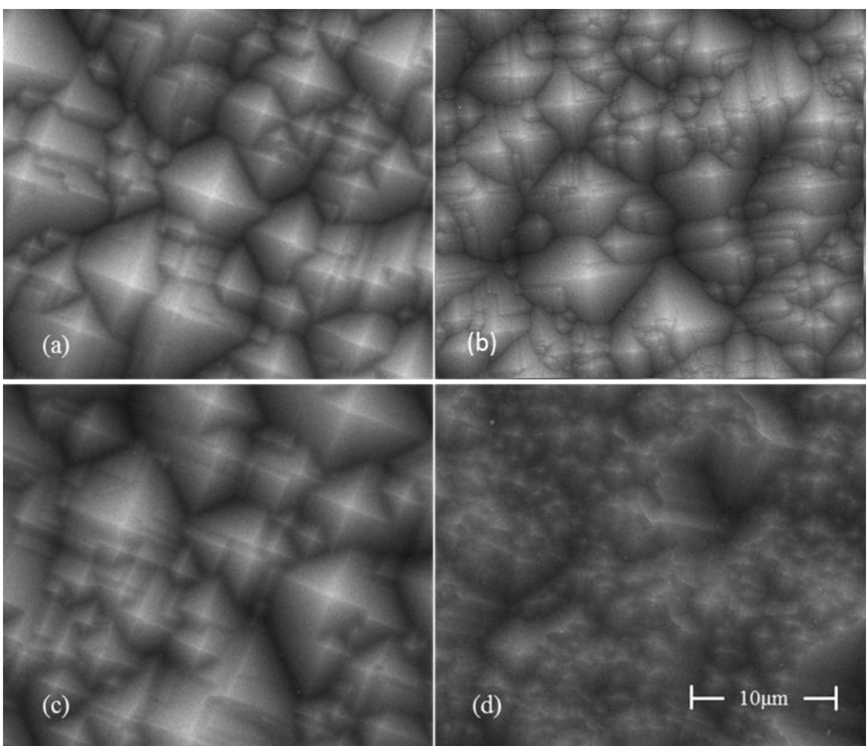

Figure 50: SEM images a) without etching b) 30s etched c) 80s etched and d) 120s etched textured wafer

In Figure 50-a, the sharp tips of random pyramids is brighter than other SEM images. At this point, the cross-section views should be taken to make more clear observation on etching. However, it is clearly seen from SEM images that 120s etched sample where most of the pyramids were etched away result in rough surface.

The next step is to identify behavior of the pyramid rounding on SHJ solar cell parameters. The V_{OC} values are strongly depended on the surface passivation quality. As sharp edges of pyramids rounded the passivation quality should be increased resulting raise in V_{OC} The pyramid rounding process was integrated in between two successive RCA cleans. SHJ solar cells were fabricated under various etching time of

pyramids including reference sample with random pyramid texturing. The solar cell results after annealing at 180°C are shown in Table 6.

Table 6: Results for various etching time

Sample / Etching time	**V_{oc} (mV)**	**J_{sc} (mA/cm^2)**	**FF (%)**	**R_S (Ω)**	**R_{SH} (Ω)**	**ɲ (%)**
Reference	498	24.61	46.43	1.25	80.72	7.81
50s etch	536	23.82	54.96	1.64	105.07	8.73
60s etch	538	22,24	58.01	1,91	530.94	9.02
80s etch	540	21.91	54.32	1.89	250.16	8.78
120s etch	545	21.82	52.98	1.90	113.35	8.59

Depending on etching time, V_{OC}, FF and R_{SH} values are increasing. The rise on the V_{OC} values indicates that the sharpness of pyramids are eliminated and thus resulting in relatively high quality passivation. Moreover, significant improvement was achieved on the shunt resistance results which refers significant enhancement on leakage current mechanisms. On the other hand, the J_{SC} values are inversely proportional to etching time as expected. Due to the rounding of pyramids, the reflection loss is increased with resulting relatively low J_{SC} values. On the efficiency results, dominant effect is enhancement on the quality of passivation which is valid for below 80s etching. However, starting from 80 seconds and longer etching times, dominant term becomes optical losses that results in lower efficiencies.

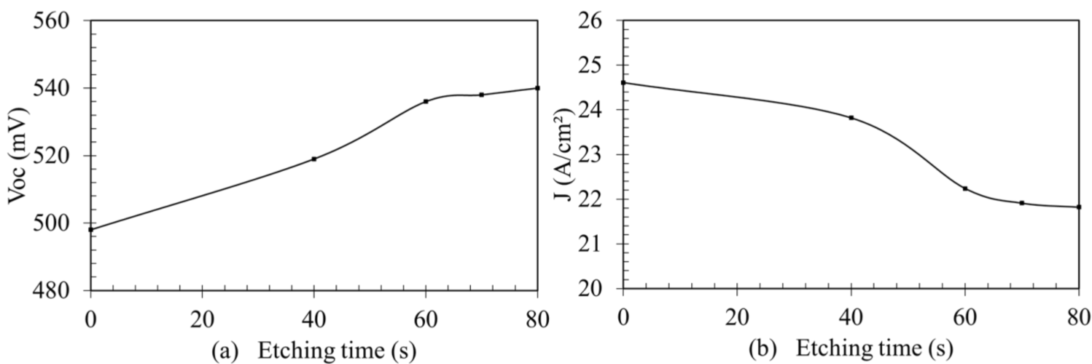

Figure 51: The variation on (a) V_{OC} and (b) J_{SC} with respect to etching time

Etching time dependence of Voc and Jsc is shown in Figure 51, respectively. The increase on the V_{OC} and shunt resistance indicates enhancement on passivation quality. To identify current losses, Suns-V_{OC} measurements were conducted and results are given in Table 7.

Table 7: Suns-V_{OC} results of 60s etched sample

Sample	V_{oc} (mV)	J_{01} (mA/cm^2)	J_{02} (mA/cm^2)	Pseudo ɲ (%)
Reference	501	5.3×10^{-12}	9.2×10^{-6}	12.16
60s etching	558	3.8×10^{-12}	8.4×10^{-7}	13.97

Results show that J_{02} value was decreased in an order of magnitude for etched sample. This indicates that surface passivation quality is enhanced due to elimination of pyramid sharpness effect and decrease on effective surface area as theoretically discussed in Chapter 2. The results show that the feasible etching time range is below 80 seconds in terms of optical loss analysis. Contrary to optical performance, passivation quality is increasing with increasing etching duration. Consequently, etching time was optimized as 60s where the highest efficiency achieved and the etching process was adapted to cell fabrication sequence with optimized parameter.

4.1.3. Hydrogen Termination of Surface Dangling Bonds

The last HF: HCl treatment is known as HF passivation. It is a widely used method to passivate Si surface through Hydrogen termination of dangling bonds. For this reason, the last HF: HCl has a significant effect on SHJ solar cell parameters [65-66]. In order to optimize HF passivation step, the volume ratio of HF: HCl diluted by DI-water was fixed at 2%: 2% and various HF: HCl treatment duration was scanned. Solar cells were produced including optimized rounding pyramid process and all other process conditions were kept constant except HF: HCl treatment time. The cell results are shown in Table 8.

Table 8: Results for various HF: HCl treatment time

HF: HCl Treatment Time	V_{oc} (mV)	J_{sc} (mA/cm^2)	FF (%)	R_S (Ω)	R_{SH} (Ω)	ɲ (%)
70s	541	29.56	50.75	1.92	87.34	9.19
80s	542	29.11	52.26	1.88	101.17	9.79
90s	543	29.13	52.48	1,65	114.82	10.60
120s	528	28.55	50.75	2.56	132.23	8.96

The effect of H-termination in the last wet chemical process is clearly seen from V_{OC} and ɲ values. The variation of ɲ values is around 1%. After this point, HF: HCl dipping time was optimized as 90s. It is injected in the standard SHJ solar cell fabrication. Then, 8 SHJ solar cells were produced where 4 of them were exposed to optimized rounding step and combined with others in the optimized HF: HCl treatment. The average results are shown in Table 9.

Table 9: Average results with and without rounding step

Sample	V_{oc} (mV)	J_{sc} (mA/cm^2)	FF (%)	R_S (Ω)	R_{SH} (Ω)	η (%)
Average w/o rounding step	482	28.44	53.42	1.52	122.34	9.45
Average with rounding step	522	27.10	57.51	1.79	278.72	10.11

The best cell efficiency was achieved by the combination of optimized parameters for pyramid rounding and HF: HCl treatment. J-V graph of the best cell is shown in Figure 52.

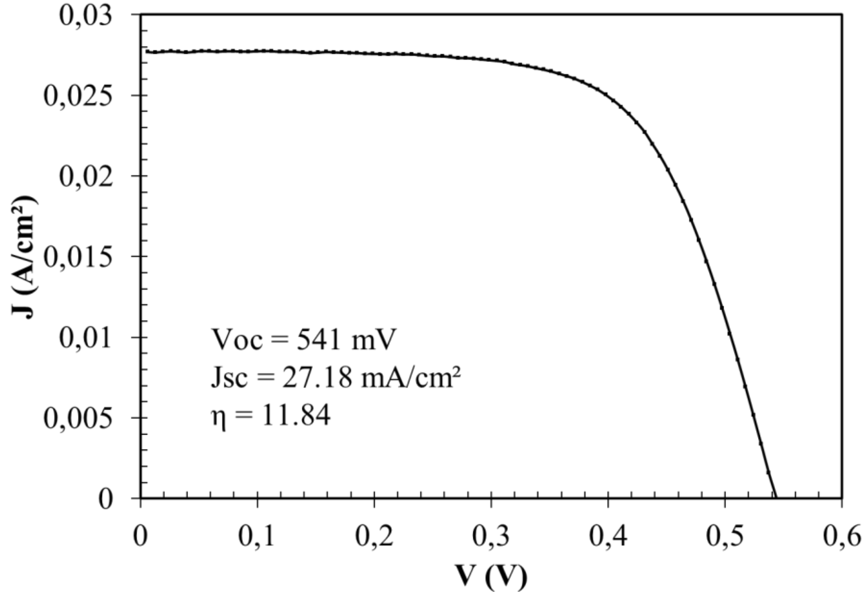

Figure 52: J-V curve of the best cell

4.1.4. Optimization of Intrinsic a-Si:H Layer

Deposition of i a-Si:H layer is one of the decisive part on the solar cell parameters due to providing excellent surface passivation quality. The lower reverse saturation current density than 4 fA/cm^2 was achieved by i a-Si:H layer passivation

[67]. The process flow and device structure are shown in Figure 53. Optimized surface preparation methods including pyramid rounding and HF: HCl steps were used in solar cell fabrication. Then, i/n$^+$ a-Si:H stack layer was growth on the c-Si substrate. SHJ solar cells were fabricated under various deposition conditions of i a-Si:H layer, where deposition parameters of n$^+$ a-Si:H and AZO were kept constant as previous study. The thickness of i a-Si:H layer is set to 7±1nm for each set of deposition.

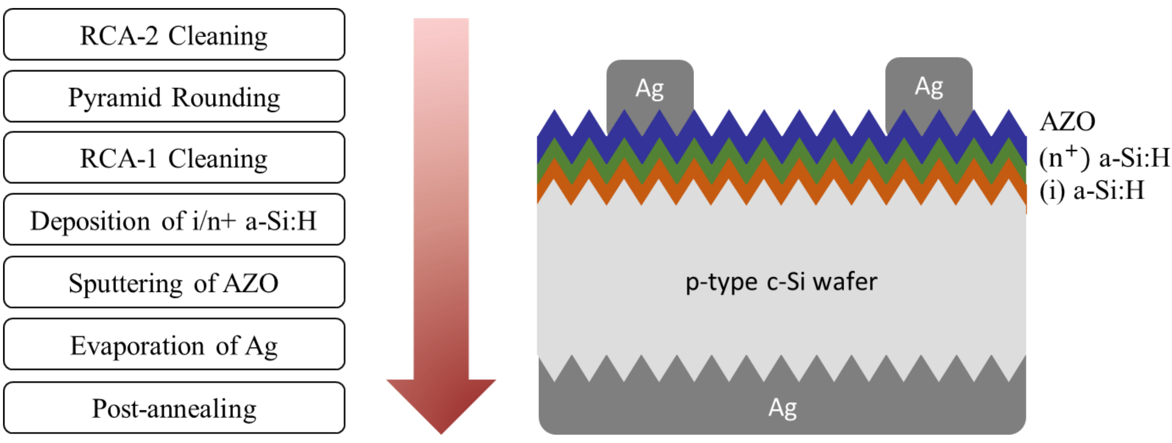

Figure 53: Experimental flow for SHJ solar cell

In order to optimize i a-Si:H layer, SiH_4 flow rate was kept constant at 350 sccm and substrate temperature at 200°C. Various deposition powers were applied between 15-100 W and deposition pressure was altered from 0.3 to 1 Torr. Moreover, the post-annealing treatment was done for each solar cell at 180°C.

In the first set, the deposition pressure was kept constant at 1 Torr and effect of various deposition powers on solar cell parameters was investigated. The results are shown in Table 10. The structure with the highest efficiency without i a-Si:H layer is named as “without i a-Si:H” and It is chosen as reference sample for the following studies.

Table 10: Results for deposition power at 1 Torr

PECVD Power	V_{oc} (mV)	J_{sc} (mA/cm^2)	FF (%)	R_S (Ω)	R_{SH} (Ω)	η (%)
Without i a-Si:H	547	28.03	61.22	1.35	576.96	11.84
15 W	481	29.82	40.62	3.56	27.10	7.28
30 W	520	29.52	56.01	1.48	164.38	10.74
50 W	499	30.24	45.40	2.32	42.08	8.65
100 W	492	28.30	54.23	1.52	123.74	9.10

Results show that the optimum deposition power for 1 Torr is 30 W with a Voc of 520mV and efficiency of 10.74%. There is a strong correlation between V_{OC} values and plasma power where higher plasma power is led to relatively low passivation quality. The reason could be correlated with plasma damage at the interface boundary. However, the shunt resistance are significantly low for the plasma power at 15 and 50W. For the results obtained deposition at 15W, the series resistance is quite high where leakage current is also high. From the results, higher defective behavior of i a-Si:H was observed as decreasing deposition plasma power below 30W and 1Torr.

In the second set, the deposition pressure was kept constant at 0.6 Torr and solar cells were fabricated under two various deposition powers. The results are shown in Table 11.

Table 11: Results for deposition power at 0.6 Torr

PECVD Power	V_{oc} (mV)	J_{sc} (mA/cm^2)	FF (%)	R_S (Ω)	R_{SH} (Ω)	η (%)
Without i a-Si:H	547	28.03	61.22	1.35	576.96	11.84
20 W	541	28.29	57.51	1.68	549.20	10.99
25 W	514	30.14	47.39	2.31	94.65	9.17

Slight gain is observed on efficiency and V_{OC} values compared previous experimental set. Moreover, the solar cell fabricated at respectively high plasma power was showed relatively low shunt and high series resistance. Moreover, the decrease in FF values was resulted lower conversion efficiency.

In the last set of depositions, the deposition pressure was kept constant at 0.3 Torr and solar cells were fabricated for deposition power at 15 W. The results are shown in Table 12.

Table 12: Results for 15W and 0.3Torr

PECVD Power	V_{oc} (mV)	J_{sc} (mA/cm^2)	FF (%)	R_S (Ω)	R_{SH} (Ω)	η (%)
Without i a-Si:H	547	28.03	61.22	1.35	576.96	11.84
15 W	522	28.88	42.36	3.70	46.01	8.01

The S-shape behavior was observed at lowest deposition pressure and plasma power. J-V curves for the samples deposited various conditions are shown in Figure 54.

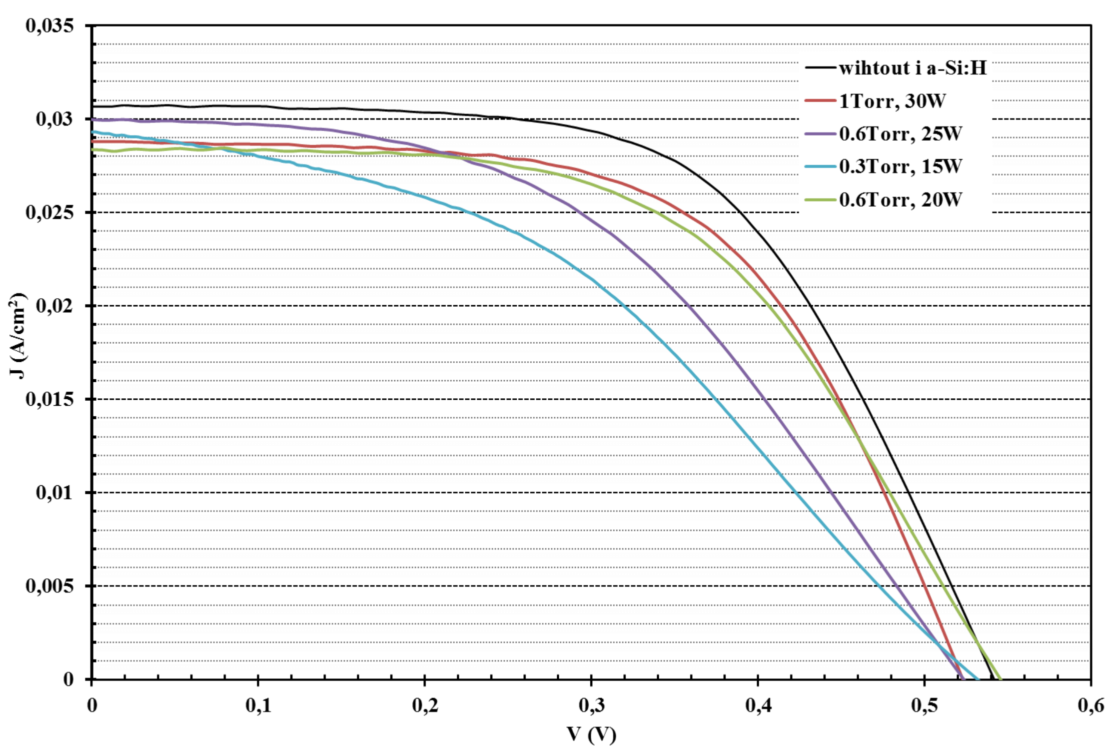

Figure 54: J-V graph of various deposition conditions

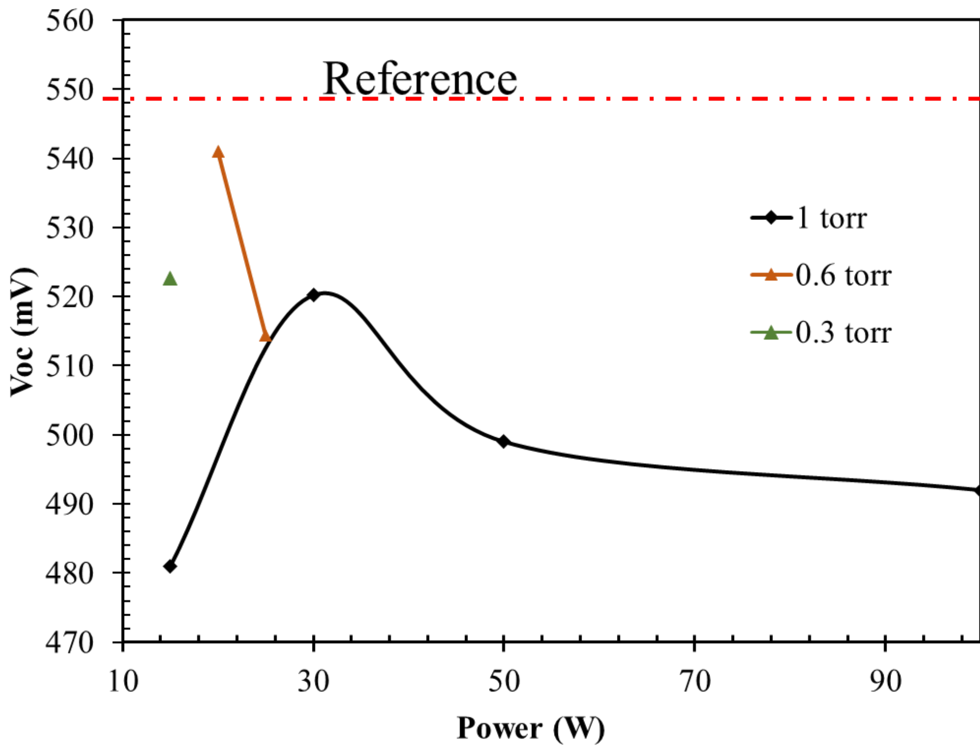

Figure 55: V_{OC} results for various deposition power and pressure

The efficiency of solar cells was decreased at a considerable amount due to decline in V_{OC} and FF values. In the last set of experiment, the decrease on FF value is directly proportional to relatively high increase in series resistance.

In general the source of series resistance belongs to metal contacts. However, if the two low power depositions are compared obtained at 1 Torr, 15 W and at 0.3 Torr 15 W, both of them have very high series resistance. It can be concluded that the lower deposition power than 20 W leads a significant increase on series resistance. To identify passivation quality of various deposition powers, the overall V_{OC} results are integrated in the graph shown in Figure 55.

The reference point refers to the highest V_{OC} value obtained from SHJ solar cells fabricated with only n+ a-Si:H layer. Any results with i a-Si:H was not exceeded the reference solar cell which means that the passivation quality of i a-Si:H was not at the desired value compared to expected V_{OC} values exceeding 740mV for excellent passivated wafers by i a-Si:H [19].

The deposition parameters of i a-Si:H layer was optimized as 0.6 Torr and 30 W at 200°C with 350 sccm SiH_4. The next step is optimization of post-annealing treatment.

4.1.5. Optimization of Post-annealing Treatment

The post-annealing is needed in order to repair sputter damages. Moreover, the thermal treatment after deposition of a-Si:H layer is known as improving passivation quality of the interface [67]. To investigate the effect of post-annealing treatment on SHJ solar cells, the experimental flow was splitted into two different device structures as shown in Figure 56.

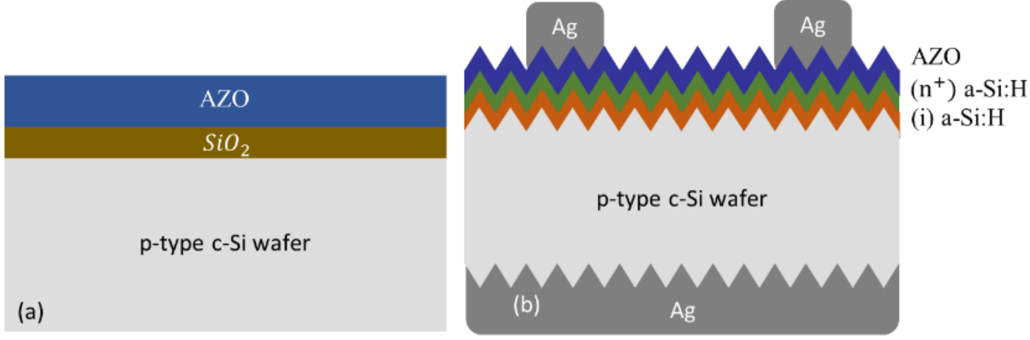

Figure 56: Device structure of post-annealing experiments (a) on only AZO layer (b) on SHJ solar cell

Relatively thick oxide layer with 80 nm thickness was used as mask layer to form potential barrier where AZO was sputtered on top of the oxide layer. Afterwards, four point probe measurements were conducted before and after post-annealing treatment. RTA system and the furnace described in Chapter 3 were used for annealing.

In the first set, AZO was sputtered at two different thicknesses (80nm, 600nm). Moreover, 5 various annealing temperatures were chosen. Before RTA treatment, four point probe measurements were conducted on 4 different points of sample and average sheet resistance and resistivity values are listed as a reference shown in Table 12. Afterwards, samples were treated in RTA system under 250 sccm N_2 flow rate with 5 min annealing duration. For all annealing temperatures, the ramp up time was 3s. Finally, the four point probe measurements were carried out on 4 different points of sample. The average resistivity and sheet resistance results are shown in Table 13.

The sharp rise on resistivity of AZO layer is observed above 300°C post-annealing treatment in RTA system. The resulting variation on resistivity value is exceeding order of magnitude for treatment done at 500°C. For this reason, the post-annealing above 300°C is not applicable for solar cells. Moreover, any improvement could not be observed on the resistivity results for all annealing temperature and thicknesses, where the resistivity of AZO decreases down to 9.81×10^{-4} Ω.cm in literature [68].

Table 13: Resistivty results for RTA treatment

Annealing temperature	**Sheet Resistance of 80nm (Ω/sq)**	**Resistivity of 80nm ($x10^{-3}$Ω.cm)**	**Sheet Resistance of 600nm**	**Resistivity of 600nm ($x10^{-3}$Ω.cm)**
Reference	148	1.18	17.56	1.05
180°C	316	2.52	17.74	1.06
200°C	356	2.84	18.59	1.11
300°C	880	7.04	34.05	2.04
400°C	1100	8.80	127.5	7.65
500°C	2180	17.4	9220	553

The second annealing set was designed on the same substrate. In this experiment set, lower annealing temperatures were aimed again by using the furnace for annealing at for 20min. In this time, the annealing ambient was atmosphere. Furthermore, the various deposition powers for AZO were also included in the post-annealing treatment study. Obtained resistivity results are listed in Table 14

Table 14: Annealing effect on resistivity AZO growth by various power

Sample	**AZO at 200W Resistivity ($x10^{-3}$Ω.cm)**	**AZO at 300W Resistivity ($x10^{-3}$Ω.cm)**	**AZO at 400W Resistivity ($x10^{-3}$Ω.cm)**
Reference	4.63	1.22	1.33
160°C	1.02	1.63	1.34
180°C	1.15	1.79	1.59
200°C	1.17	1.68	1.44
220°C	**0.98**	2.33	1.89
240°C	4.54	3.25	2.23

The resistivity of thin AZO layer is depending both deposition condition and the post-annealing temperature. The lowest resistivity value achieved in GÜNAM is $0.98x10^{-3}\Omega$.cm. The variation on resistivity value with respect to various post-annealing treatment is shown in Figure 57.

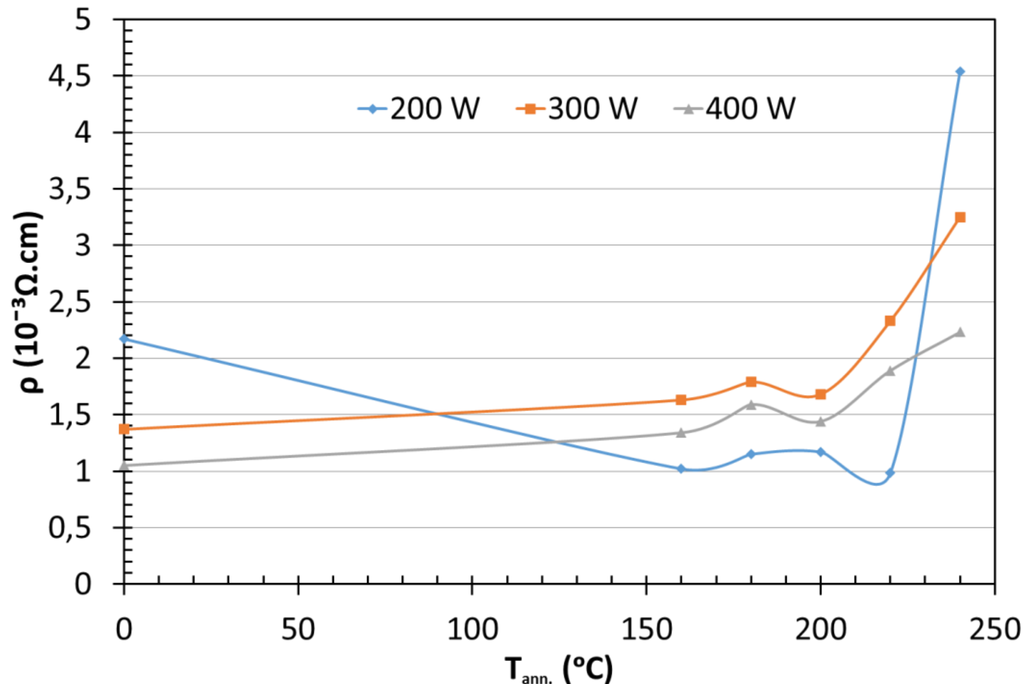

Figure 57: The resistivty values for various post-annealing treatment

Except the deposition at 200 W, layer resistivity increases with respect to annealing temperature. However, the sample deposited at 200 W unexpectedly gives better performance after post-annealing. The lowest resistivity value was achieved after annealing at 220°C for 20min. At this point, the temperature restriction for AZO film was found as 220°C and above that temperature, the film loses its conductivity resulting in undesired consequence on the corresponding cell performance.

After analyzing effects of post-annealing treatment on AZO film, the temperature range between 180°C to 250°C was adapted to fabrication process flow to

identify overall effect on SHJ solar cell. For each temperature, the annealing duration was fixed at 30 min. Corresponding device results are shown in Table 15.

Table 15: Device results after annealing

Annealing temperature	**Voc (mV)**	**Jsc (mA/cm²)**	**FF (%)**	**R_S (Ω**	**R_{SH} (Ω)**	**ɲ (%)**
180 ℃	514	29.07	44.66	3.99	88.83	8.36
200 ℃	547	29.21	51.22	2.29	124.76	**10.24**
220 ℃	557	29.03	49.93	2.31	74.58	10.10
240 ℃	540	27.79	38.45	3.98	25.22	6.66
260 ℃	534	16.67	21.87	15.23	8.93	2.44

The passivation quality of a-Si:H layer was slightly increased resulting in V_{OC} higher than 550 mV. The sharp decrease of J_{SC}, ɲ and FF values was observed above 220°C. The variation on solar cell parameters with respect to post-annealing temperature is shown in Figure 58. The maximum point of R_{SH} was observed for annealing at 200°C together with the lowest R_S. Thus, relatively higher efficiency is observed for the sample annealed at 200°C.

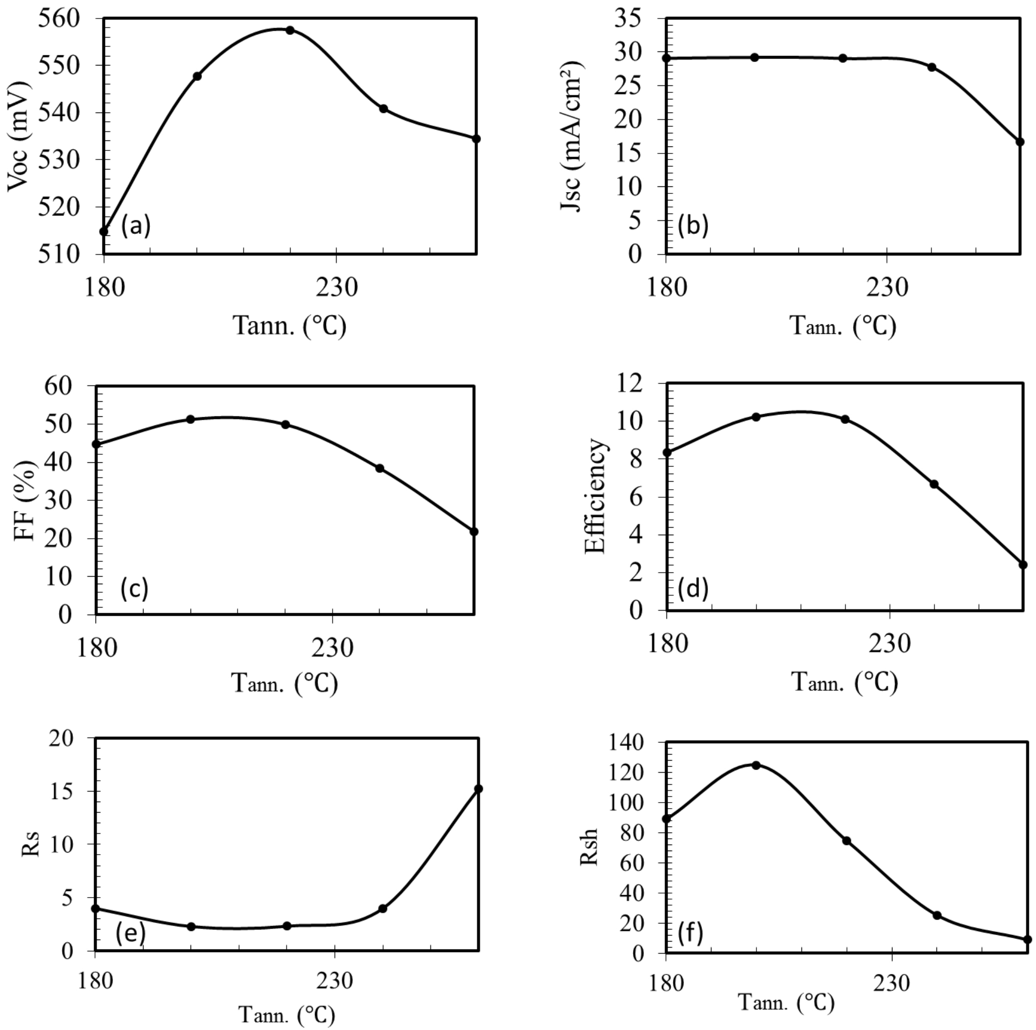

Figure 58: (a) V_{OC}, (b) J_{SC}, (c) FF, (d) ɲ, (e) R_S, (f) R_{SH} variation with respect to annealing temperature

J-V curves are shown in Figure 59. The S-shape behavior was observed for samples annealed at 180°C and 240°C. Series resistance dramatically increases as expected due to behavior of AZO layer at high annealing temperatures. Furthermore, the sample annealed at 260°C loses expected I-V behavior due to higher R_S and lower R_{SH}.

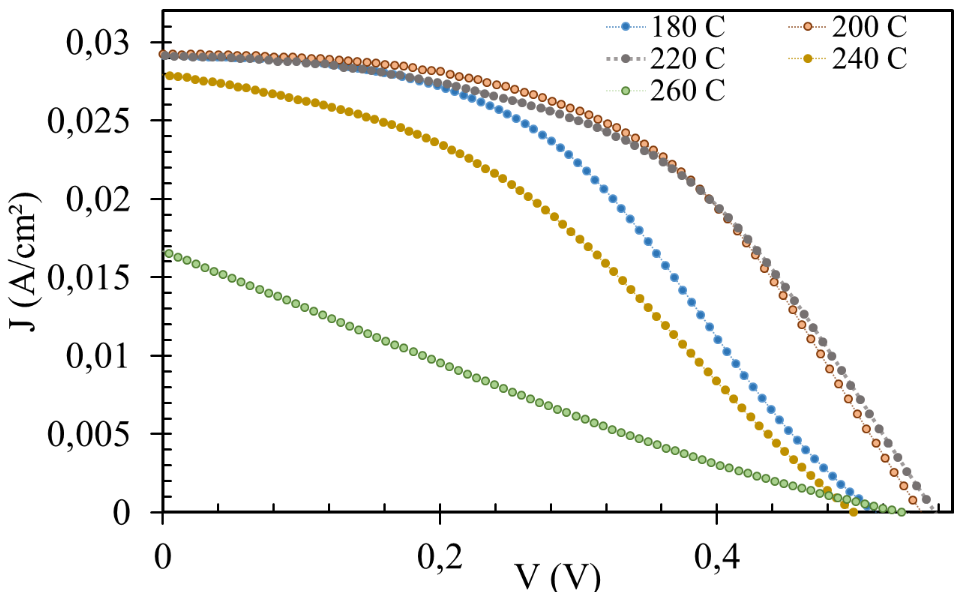

Figure 59: J-V curves for different annealing temperature

The notable influence of post-annealing treatment was observed on all solar cell parameters. The last set of experiment was designed to make more precise optimization. For this purpose, annealing temperatures were selected as 200°C and 210°C. This time, various annealing durations were applied for chosen temperature values.

The results of the last optimization set showed that the annealed samples at 210°C gave better performance. J-V curves for the samples annealed at 210°C are shown in Figure 60 and the results are listed in Table 16. In table 16 "B." refers to before annealing and "A." refers to after annealing.

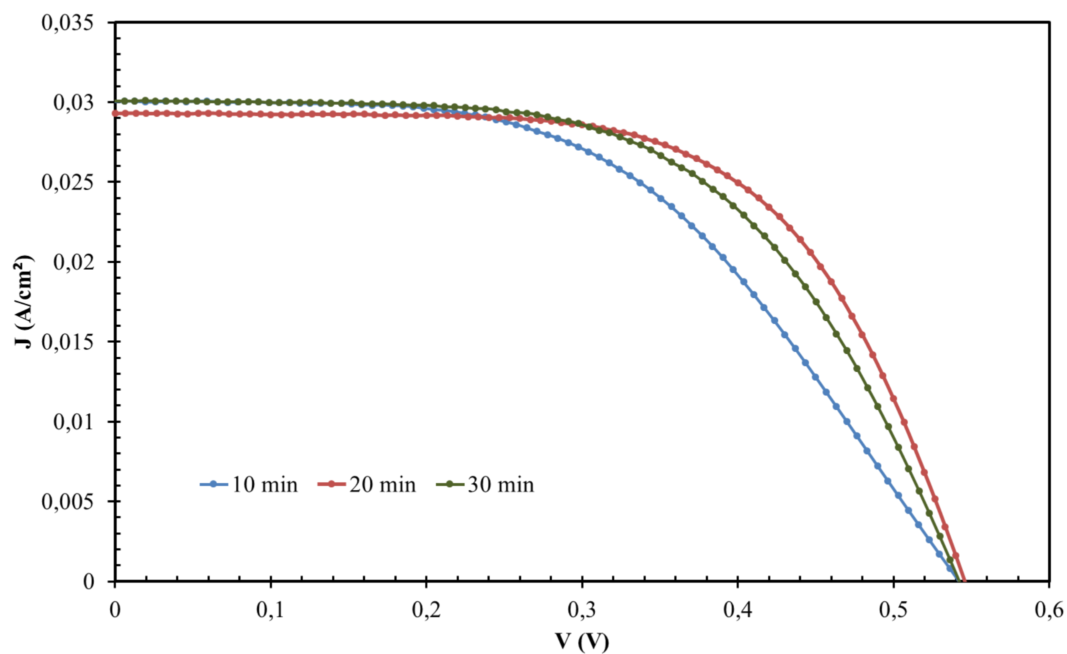

Figure 60: J-V curves of various annealing duration

Table 16: Solar cell results with respect to post-annealing duration at 210°C

Annealing Time	Voc (mV)		Jsc (mA/cm2)		FF (%)		R_S (Ω)		R_{SH} (Ω)		ɲ (%)	
	B.	**A.**	**B.**	**A.**	**B.**	**A.**	**B.**	**A.**	**B.**	**A.**	**B.**	**A.**
10 min	420	542	29.38	30.24	48.72	53.33	1.97	1.98	182	415	7.53	10.5
20 min	416	545	28.96	29.63	49.90	56.78	1.88	1.85	268	898	7.53	11.76
30 min	406	541	29.53	30.05	46.73	58.06	2.08	1.35	117	615	7.01	11.82
The best 20 min	424	546	28.53	29.28	49.25	62.51	1.93	1.10	252	1358	7.19	12.48

After the last set, the post-annealing treatment was optimized as 210°C for 20 minutes under atmosphere. EQE of the best performing cell is shown in Figure 61.

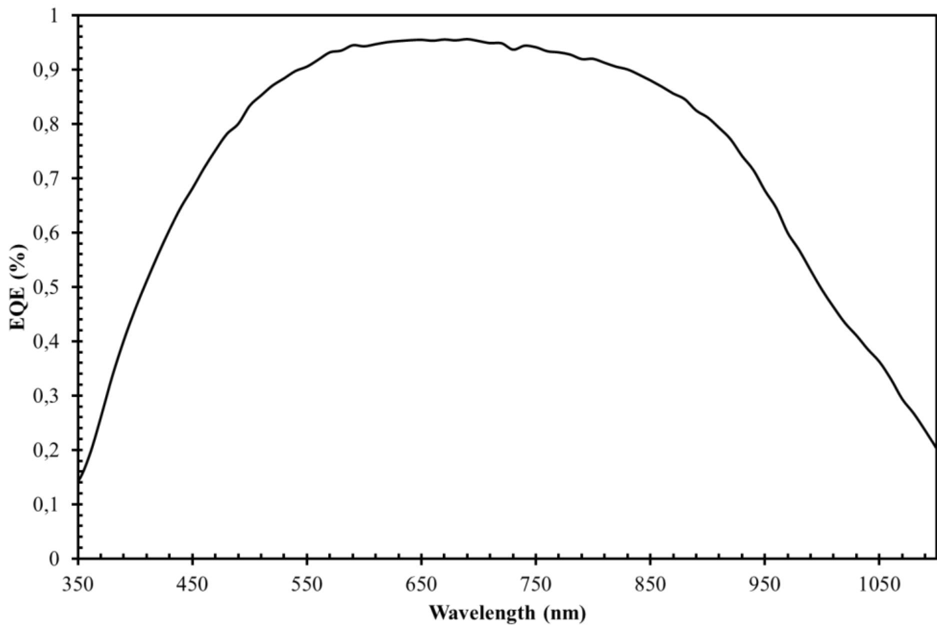

Figure 61: EQE result of the efficient solar cell

The Suns-V_{OC} results are listed in Table 17. The highest pseudo efficiency was achieved as 15.68% with 551mV V_{OC}.

Table 17: Suns-VOC results for two efficient solar cells

Sample ID	V_{oc} (mV)	J_{01} (mA/cm^2)	J_{02} (mA/cm^2)	ɲ (%)
#1	551	1.8×10^{-11}	1.0×10^{-10}	15.68
#2	550	3.4×10^{-11}	3.7×10^{-10}	15.58

The lowest J_{02} value is achieved as 1.0×10^{-10} mA/cm^2. The total improvement on reverse saturation current on depletion region achieved by the optimization of post-annealing study is almost around two order of magnitude. That shows the enhancement on passivation quality of SHJ solar cell by thermal treatment.

In Figure 62, J-V curve of the best SHJ solar cell with 0.9cm^2 effective cell area fabricated in GÜNAM is shown.

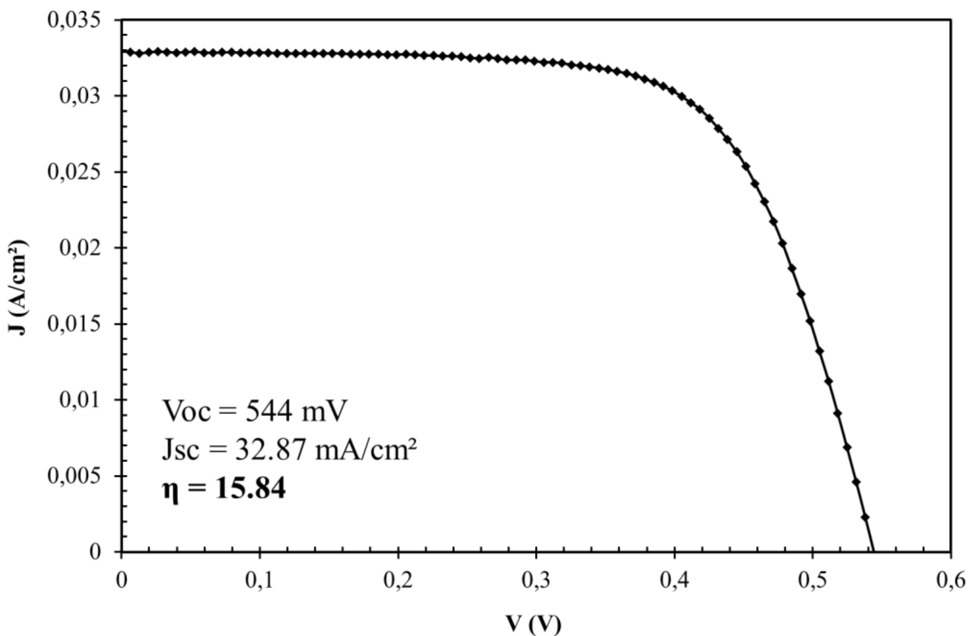

Figure 62: J-V curve of the best SHJ solar cell fabricated in GÜNAM Laboratories

After optimization of all process steps, the V_{OC} values were still lower than the reference SHJ solar cell (without i a-Si:H layer). The excellent passivation of a-Si:H layer provides V_{OC} exceeding 740mV. In this point of view, the passivation quality could be still said to be low. To enhance the passivation quality of i a-Si:H, design of the i chamber has been changed. The plasma box was constructed in the chamber to achieve more uniform heating profile through whole substrate surface resulting in more uniform i a-Si:H layer. After this modification, the effective lifetime values are exceeding 3ms with only i a-Si:H (7nm) coating on double side of FZ n-type Si wafer.

4.2. Silicon Heterojunction IBC Solar Cell

In Imec, i^2 module group is currently concentrated on SHJ IBC solar cell fabricated on thin Si monocrystalline foils (called as epifoils) [54]. Under this circumstance, the fabrication process flow was shaped to integrate thin foils. Through the study done in Imec, both 200μm thickness and 2-4ohm.cm resistivity FZ and CZ Si wafers were used. The fabrication sequence and device structure is schematically illustrated in Figure 63. The sequence starts with IMEC Clean and follows front surface passivation. At this point, applicability of a-Si:H and SiNx stack layer has been worked in terms of passivation quality where SiNx is known as one of the excellent materials for ARC purposes. Through the study, Imec standard recipe was used for deposition of i, n^+, p^+ a-Si:H and SiNx layers, where the depositions were carried out below 200ºC. PECVD system was used for the deposition of mentioned layer.

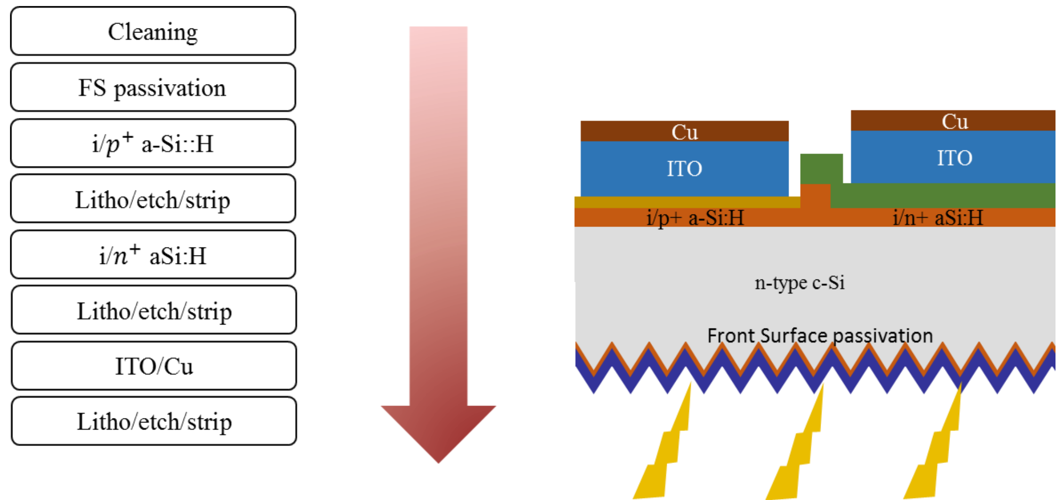

Figure 63: Fabrication sequence and device structure in Imec

After front surface passivation, the successive process step is formation of junction with p^+ a-Si:H and BFS with n^+ a-Si:H. In the formation of junction, a wet chemical etching method was introduced as an emitter pattering technique developed

in Imec. In the formation of BSF, the selective etching method was used to pattern n^+ a-Si:H layer [57]. The final process step is metallization with ITO and Cu stack.

4.2.1. Front Surface Passivation

The first study conducted in Imec was the passivation quality of i a-Si:H/SiN_X stack and the applicability of the stack layer to SHJ IBC solar cell concept. Under this scope, formerly cleaned by IMEC clean n-type CZ wafers were used. After cleanings, HF treatment was done to remove oxide layer from the surface. The a-Si:H layers were deposited by PECVD system to double sides of wafer as demonstrated in Figure 64 (a). To check the quality of passivation, the minority carrier lifetimes and calibrated PL images were measured. After that, SiNx layers were coated double sides of passivated sample as demonstrated in Figure 64 (b).

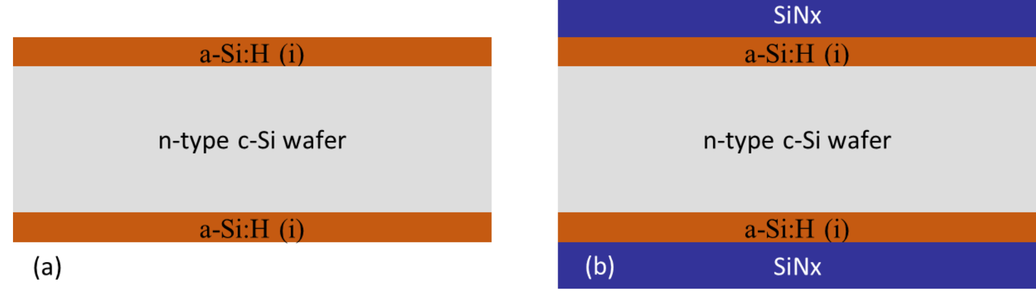

Figure 64: Passivated samples with (a) i a-Si:H layer and (b) i a-Si:H/SiN_X

The lifetime results of both i a-Si:H and i a-Si:H/SiN_X stack layer are listed in Table 18.

Table 18: Lifetime results

Sample ID	i a-Si:H layer	i a-Si:H / SiNx stack
#1	τ = 2.64 ms J_0= 4.1 fA/cm^2	τ =3.02 ms J_0= 4 fA/cm^2
#2	τ = 2.33 ms J_0= 5.7 fA/cm^2	τ = 3.53 ms J_0= 5.5 fA/cm^2
#3	τ = 4.93 ms J_0= 3.8 fA/cm^2	τ = 7.05ms J_0= 3.4 fA/cm^2

The results show that after SiNx deposition, the lifetime results are slightly increased except 3rd sample where the resulting J_0 values are still in the same range. The passivation quality of 3rd sample was increased in a respectable range. As a result of SiNx deposition, the passivation quality of i a-Si:H layer could be enhanced.

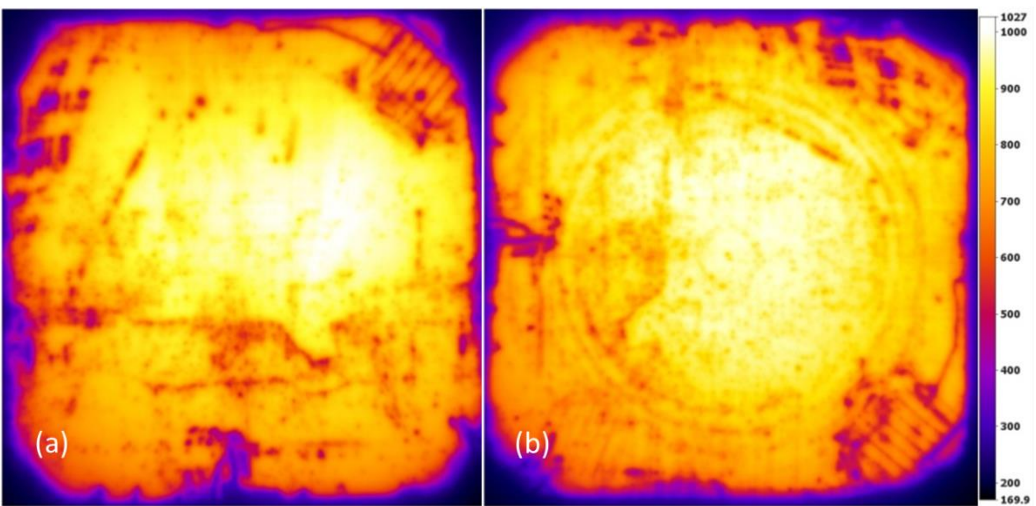

Figure 65: Calibrated PL images after (a) i a-Si:H deposition and (b) SiNx deposition

In Figure 65, calibrated PL images of i a-Si:H and i a-Si:H/SiNx stack layers (sample ID #1) are shown, respectively. On the right of the Figure 65, the calibrated lifetime scale is shown in µs. From this scale, the yellowish areas on the image gives

higher lifetime results respectively. According to the PL images, impressively uniform passivation layers and high lifetimes were achived by a-Si:H/SiNx stack layer. The effective lifetime vs minority carrier density graph of the sample 1 is shown Figure 66.

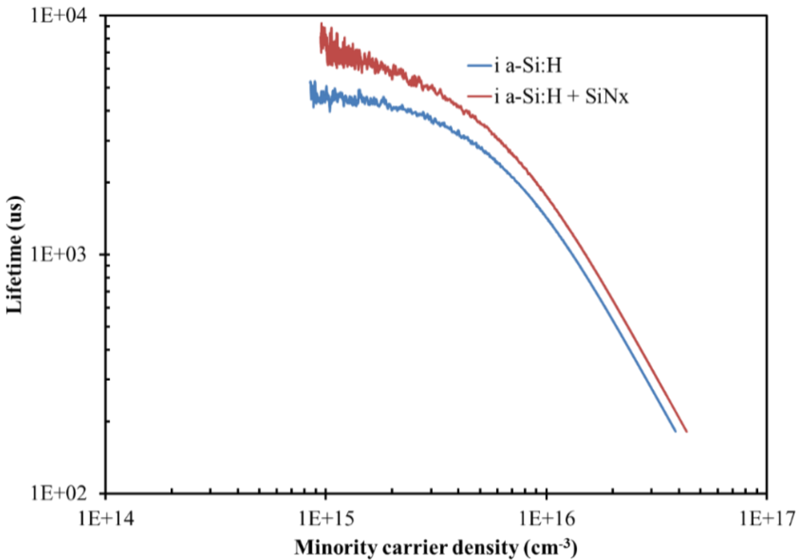

Figure 66: Effective lifetime results

Besides the lower reflection and absorption property of SiNx layer, the stack layer is a valuable candidate for the front surface passivation of SHJ IBC solar cell in terms of high lifetime and low J_0 values. The next step is to observe behavior of stack layer after thermal treatment. For this purpose, four various post-annealing temperature were selected. After thermal treatment, the lifetime measurement was conducted for each. The ageing study was conducted on the thermally treated samples under cleanroom environments for 45 days. The aging and post-annealing study was combined together as shown in Table 19.

Table 19: Results for post-annealing and ageing studies

T_{ann} (˚C)	t_{ann} (min)	Before Annealing τ (ms)	τ (ms)	After 14 days τ (ms)	After 1 Month τ (ms)	After 45 days τ (ms)
200	15	7.05	4.26	3.8	3.6	3.6
200	30	7.05	6.34	5.5	5.5	5.5
200	45	7.05	6.05	5.0	4.5	3.2
220	15	3.53	2.3	2.2	2.2	2.0
220	30	3.53	3.1	2.7	2.6	1.9
250	15	3.53	2.96	2.5	2.5	2.1
250	30	3.53	3.4	3.3	3.2	3.2
300	30	3.02	1.9	1.7	1.7	1.6

Results show that after post-annealing of the samples, the effective lifetime values were decreased especially the sample annealed at 300ºC. The decrease after post-annealing can be related with either thermal treatment or ageing of the layers. At this point, the ageing study showed that the effective lifetime values were fixed after 1 month in cleanroom atmosphere and it is valid for the most of the samples.

The i a-Si:H/SiNx stack layer was yield in promising lifetime results including ageing and it was decided as a front surface passivation layers.

4.2.2. Rear side passivation

The second study was determination of emitter patterning technique for the fabrication of SHJ IBC solar cell. For the study, 3-4 ohm.cm resistivity n-type FZ wafers were used as a substrate. The technique worked in this study is etching of i/p^+ a-Si:H layer resulting opened areas on Si surface and re-passivation of the etched areas

by i/n^+ a-Si:H by forming BSF region on the rear side. For this purpose, two wet chemical etchants were used; (i) buffered HF (BOE): HNO_3: H_2O and (ii) BOE: H_2O_2.

The experimental sequence was designed as shown in Figure 67 for each wet chemical etchant. The first, i/p^+ a-Si:H layers were deposited both side of the wafers. Then deposited layers were removed away by the etchant. After cleaning of wafers, the i/n^+ a-Si:H layers were deposited on the both sides. After each deposition, the effective lifetime and PL images were measured to check quality of passivation and to control etching profile by PL images.

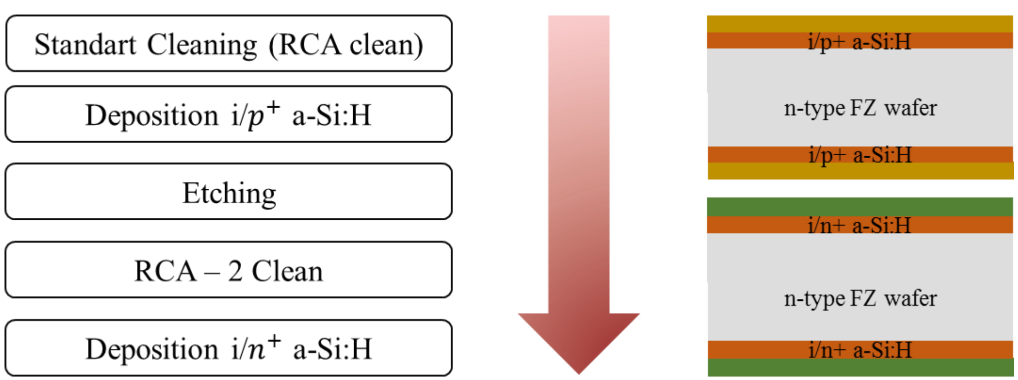

Figure 67: Experimental sequence and device structure

In the first run, the etch rates were calculated for the various concentration of buffered HF by measuring the thickness of a-Si:H layer and the re-passivation quality of ethed areas was checked via coating with i/n^+ a-Si:H layers. Before ethcing of i/p^+ a-Si:H layer, the effective lifetime was 3.2ms. The results belonging to re-passivation of the sample are shown in Figure 68.

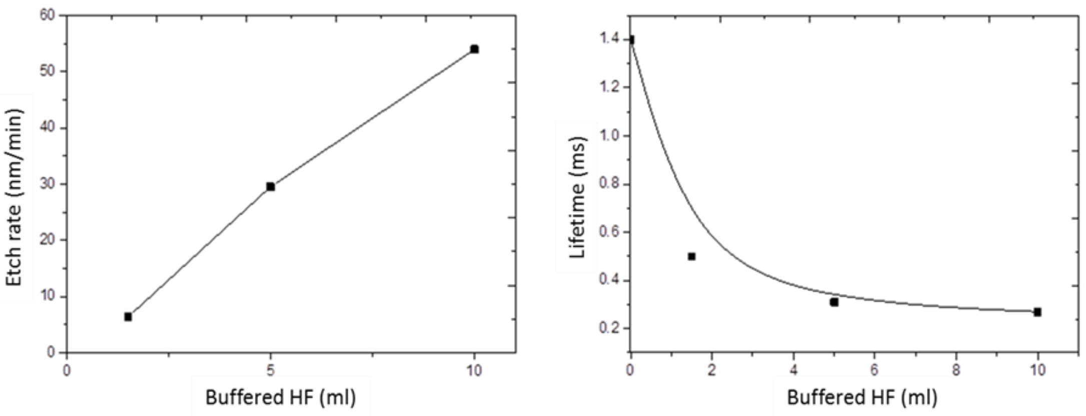

Figure 68: Correlations between BOE and etch rate, effective lifetime

Results show that increasing buffered HF concentration leads to a rise on the etch rate where the lifetime results acts inversely proportional to concentration. The lowest etching rate (8nm/min) was yielded in 450 µs lifetime after passivation by i/n$^+$ a-Si:H layer as the highest value of the experiment set. The lowest concentration was selected and time depending etching study was performed via selected etching. Effects of various etching time on the passivation quality was investigated. From the calculated etch rate, the i/p$^+$ a-Si:H layer should be etched around for 18 minutes. For this reason, duration times were selected as 10, 15, 20 and 25min to observe transition from unsufficient etching to overetched region. After i/p$^+$ a-Si:H layer deposition, the effective lifetime was 3.2ms. After etching and re-passivation of the sample, lifetime measurement and PL images were taken. The lifetime calibrated PL images are shown in Figure 69.

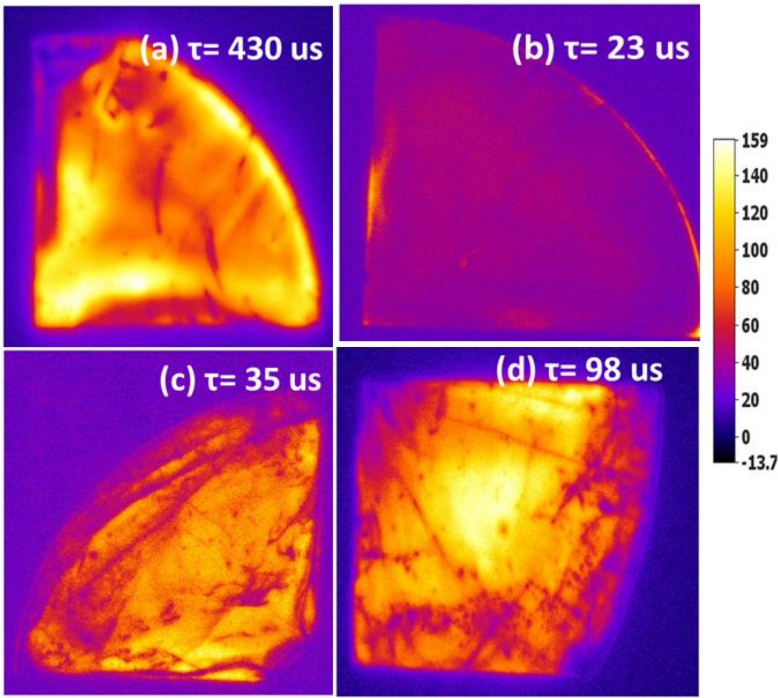

Figure 69: Calibrated PL images of repassivated samples after (a) 10min (b) 15min (c) 20min (d) 25min etching

The results show sharp decrease on the lifetime for the higher etching time. Moreover, the general passivation quality of the etched area was comparatively low with respect to achieved on front surface passivation. In the Figure 69-a, It can be concluded that the formerly deposited a-Si:H layer could not be etched in 10 min as expected. When the passivation region was not etched totally, the former passivation was not killed by etching. However for 20 min etched sample, it was clearly seen that the sample could not be passivated by i/n$^+$ a-Si:H layer. At this point several experiments were designed to understand reason of the passivation problem. Surprisingly, it was found that the passivation quality of the etched areas could be improved by surface cleaning methods, which needs relatively high wet chemical oxidation temperatures (>70ºC). On the sample exposed to Piranha, RCA-1 and RCA-2 cleanings after totally etching of i/p$^+$ a-Si:H layer, the effective lifetime results were exceeded 3ms via i/n$^+$ a-Si:H deposition. However the nature of cleaning processes, it oxidizes the a-Si:H layer and etches the emitter region resulting in degradation of effective lifetime results. Therefore the utilization of oxidizing agent is crucial in terms

of maintain the passivation of emitter region. The cleaning processes were restricted below 35ºC. RCA-1was selected as cleaning process due to effective removal of organic residues. In fabrication procedure, photolithography steps were inserted to pattern rear side and the RCA-1 solution is effective on cleaning of residues belonging to photoresists. Due to the lack of re-passivation quality of BOE: HNO_3: H_2O solution, the alternative mixtures were investigated for patterning of i/p$^+$ a-Si:H layer. At this stage, a wet chemical etching approach was introduced for the purpose of BOE: H_2O_2 patterning. As discussed earlier, the main difference between these two etchants is that the first one has electrochemical whereas other has chemical etching mechanism. For the electrochemical etching of a-Si:H layer, the reaction mechanism depends strongly on concentration of BOE resulting in low passivation values.

From experimental view of using BOE: HNO_3: H_2O solution, it is hard to control etch rate due to the correlation between etch rate and ageing or conditioning of solution. To identify ageing effect on the etching mechanism, an experiment was designed. The fresh BOE: HNO_3: H_2O solution was prepared and after each 1 hour initially i/p$^+$ a-Si:H substrates were etched and passivated via i/n$^+$ a-Si:H deposition. The results are listed in Table 20. From these results, the quality of etching in terms of passivation was obviously poor and unstable through various ageing time.

Table 20: Results for ageing study

Ageing Time	Fresh solution	After 2 hours	After 4 hours	After 6 hours	After 8 hours	After 24 hours
Effective lifetime (µs)	375	450	725	60	60	600

To identify the etching quality in terms of resulting passivation, various BOE concentrations were used. For each concentration, the etch rate was also calculated and the resulting effective lifetimes were measured including calibrated PL images. Initially i/p$^+$ a-Si:H layer deposited samples that have 3.7ms effective lifetime were used . The samples were etched via BOE: H_2O_2 solution following RCA -1 cleaning.

Samples were re-passivated by i/n+ a-Si:H layer after cleaning process. The final step was the measurement of effective lifetime values. The effective lifetime, etch rates and calibrated PL images are listed in Table 21.

Table 21: Reuslts for various concentration of BOE

Concentration of BOE: H_2O_2	Etch rate (nm/min)	Lifetime results after repassivation (ms)	Calibrated lifetime images	Color scale
1: 5 (15 min etching)	1.2	4.3		2000 1800 1600 1400 1200 1000 800 600 311.8
1: 10 (30 min etching)	0.6	4.0		
1: 30 (40 min etching)	0.45	2.1		
1: 100 (60 min etching)	0.25	3.2		
1: 300 (125 min etching)	0.15	2.2		

Results showed that the etch rate of solution is directly proportional to concentration of BOE. However, depending on concentration, the longer etching

duration was needed for total removal of i/p$^+$ region which exceeding 30min of etching. In terms of applicability to solar cell application, longer etching times are not desired. Moreover, the longer etch duration means that the longer exposure time of photoresist to wet chemical solution which results in compatibility problem of photoresist with the chemical solution.

The effective lifetime results showed that the excellent passivation could be reached via higher concentration of BOE. The calibrated lifetime images also support the effective lifetime results with fairly uniform passivation through whole surface.

To identify improvement achieved by the new solution, Transmission Electron Microscopy measurements were done for the samples etched via BOE: H_2O_2 (1:5) and via BOE: HNO_3: H_2O solutions. The results are shown in Figure 70, respectively.

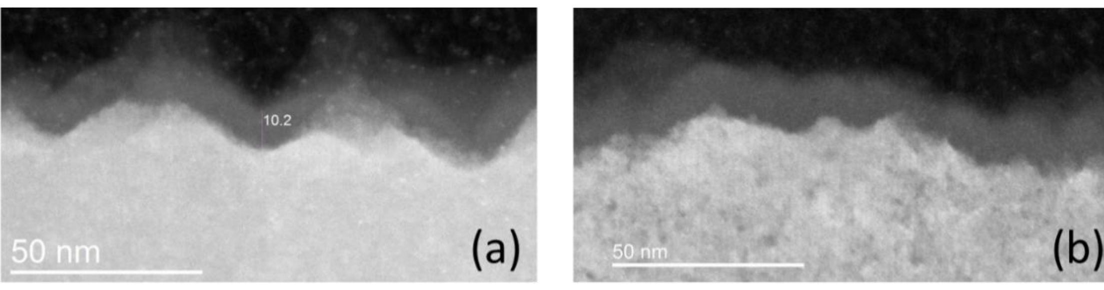

Figure 70: TEM resutls for (a) sample etched by BOE: H_2O_2 (b) BOE: HNO_3: H_2O

From TEM images, the roughness of the surface could be seen clearly. However, on the sample etched by the buffered HF: HNO_3: H_2O solution (Figure 70 b), the porous like surface is observed, which results undesired situation in terms of passivation quality. The comparison of various etchants is shown in Table 22.

Table 22: Comparision of etchants

Etchant	Resist compatibility	Etch rate	Passivation
BOE: HNO_3 : H_2O (1.5:500:200)	OK	Not stable	LOW
BOE : H_2O_2 (1: 10)	OK	Stable	HIGH
BOE : H_2O_2 (1:5)	OK	Stable	HIGH

To sum up the experiments done up to now, the new chemical etchant was introduced with promising effective lifetime results compared to other one. Moreover, BOE: H_2O_2 with concentrations 1:5 and 1:10 were selected for solar cell fabrication since the highest passivation qualities were achieved with these solutions. Before starting fabrication of SHJ IBC solar cells, the last step was to check the re-passivation quality of selected etchant with patterning via photolithograph as process steps schematically shown in Figure 71.

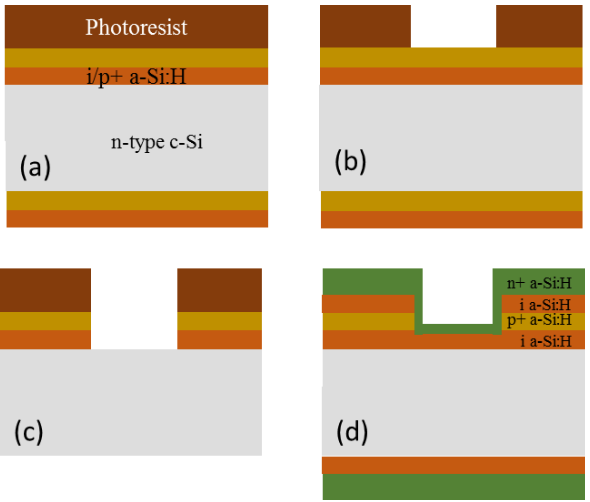

Figure 71: Shematic representation of process steps

Formerly cleaned FZ n-ype Si wafers were passivated by i/p$^+$ a-Si:H layer on both side. Then, i/p$^+$ a-Si:H layers were patterned by BOE: H_2O_2 with photolithography. After resist strip process by acetone and isoproponal alchol, the samples were also treated by RCA-1 clean at 35°C. At this point, the PL images of etched sample was taken to identify the patterning quality of the etchant. The PL image is shown in Figure 72.

Figure 72: PL image of etched area

The profile of etched areas are clearly seen in Figure 72. After removal of oxide via HF: HCl treatment, i/n$^+$ a-Si:H layer was deposited double sides of sample. The PL images and effective lifetimes were measured. The callibrated PL images are shown in Figure 73.

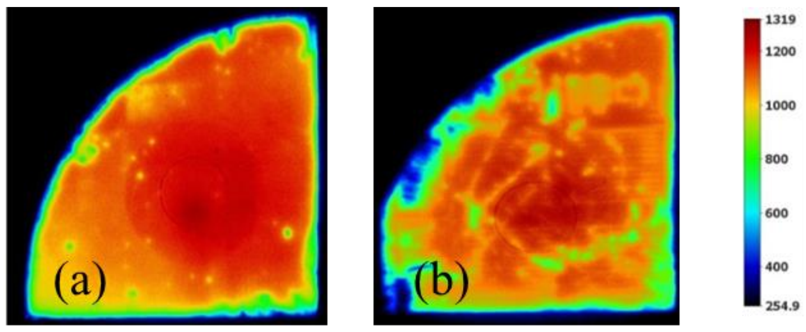

Figure 73: After i/n$^+$ deposition on the etched samples by BOE: H_2O_2 at concantration of (a) 1:5 and (b) 1:10

The results of calibrated PL images were breathtaking in terms of the uniform re-passivation on the etched areas. It was hard to detect patterned areas because of relatively high effective lifetime values. The effective lifetime results are shown in Figure 74.

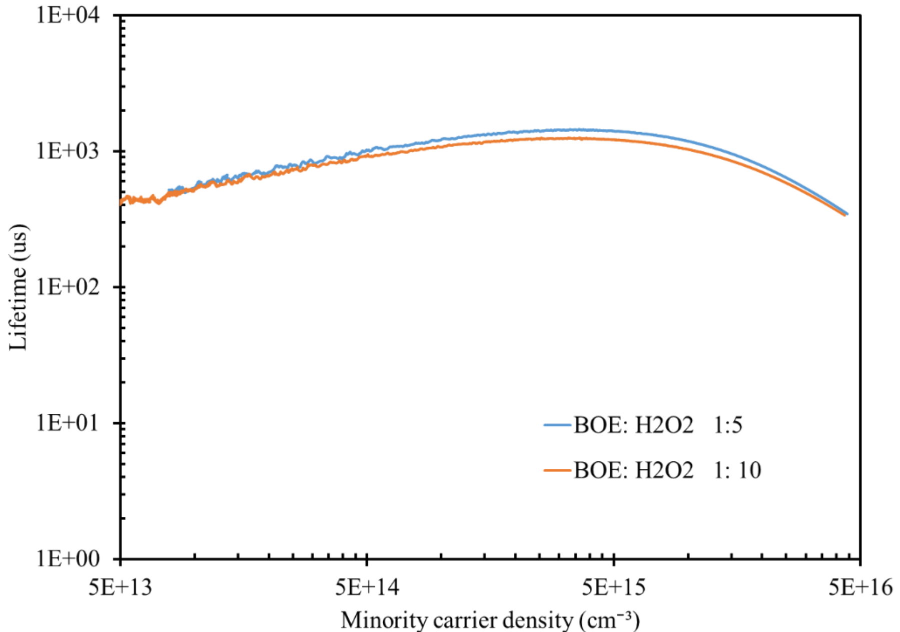

Figure 74: The effective lifetime results of BOE: H202 for various concentrations

The BOE: H_2O_2 etchant with concentration of 1:5 was yield in a better perfomance in terms of effective lifetime after repassivation. For this reason, the etchant was integrated to solar cell fabrication process as the emitter etching technique. The fabrication processes of SHJ IBC solar cell is shown in Figure 74. The process flow was started with deposition of front surface passivation (i a-Si:H/SiNx stack) and emitter on the rear side resulting in an effective lifetime higher than 3ms. Then, emitter was patterened via BOE: H_2O_2 (1:5) to remove i/p+ a-Si:H layer as shown in Figure 75 (b). At this stage, the front surface was protected by covered photoresist. The BSF region was deposited to whole rear side (Figure 75(c)). The BSF region was patternned to block shunt between junction via sencondary photolitghrophy step. TMAH was the etchant used for i/n^+ a-Si:H layer patterning where TMAH is one of the selective

etchants on p-doped region. This means that the etching reaction is stopped when it reaches to p^+ a-Si:H layer. The final step is deposition of ITO and Cu and patterning of metal contacts by photolitgrophy step.

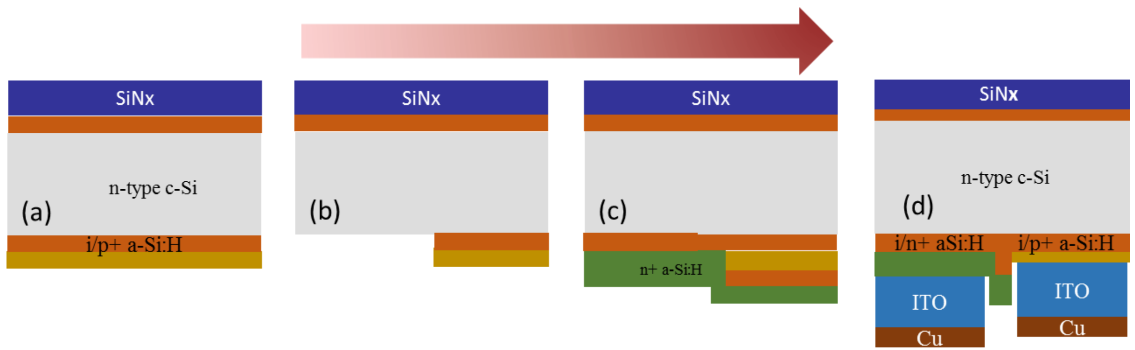

Figure 75: Fabrication flow of SHJ IBC solar cell

During the fabrication flow, the calibrated lifetime images were taken to check the quality of passivation. Figure 76-a shows the calibrated lifetime image after front surface passivation and emitter formation and Figure 76-b shows right after passivation of etched areas via i/n+ a-Si:H layer.

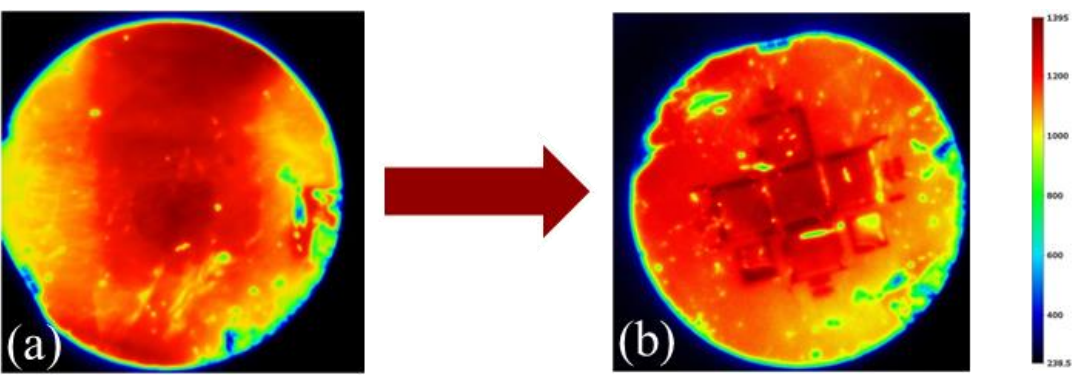

Figure 76: Calibrated PL images after (a) front and rear side passivation and (b) re-passivation

Results showed that uniform passivation of patterned areas were achieved with effective lifetime higher than 1.5ms. Later, mentioned process flow was followed and $2x2cm^2$ SHJ IBC solar cells were fabricated. The results of solar cells are listed in Table 23.

Table 23: The SHJ IBC solar cell results

Sample	V_{oc} (mV)	J_{sc} (mA/cm^2)	FF (%)	ɳ (%)
The best of 5	701	35.8	71.9	18.1
Average of 5	693	35.5	70.4	17.3

The achieved highest efficiency was 18.1 % with the mentioned emitter etching method on the chemically polished sample without any surface texturing. The J-V curve of the efficient solar cell is shown in Figure 77.

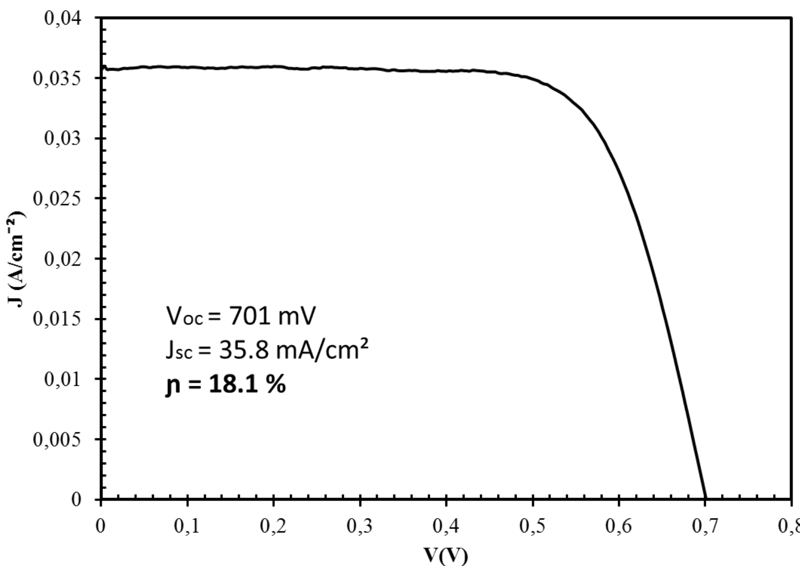

Figure 77: The efficient solar cell J-V graph

The emitter etching method was introduced to fabrication process of SHJ IBC solar cell with providing high surface passivation. However, the cell results showed that the FF values were comparatively low. Since, the method has not been combined with surface texturing to achieve higher JSC values, relatively high efficiency could be reached as a further improvement on the etching method.

CHAPTER 5

CONCLUSION

Raise in energy demand leads the research area to focus on alternative energy sources all over the world. One of the strongest candidates on alternative energy sources is solar energy, particularly photovoltaics which has the opportunity to convert sun light directly to electricity. Due to the sharp decrease on production cost of Si wafer, the solar energy market is manipulated by Si based solar technologies. Among all Si based technologies, SHJ solar cell has become a favorite in terms of higher efficiency opportunity and low thermal budget.

Recent developments on SHJ solar technology are based on increasing passivation quality of a-Si:H layer and integrating IBC concept to SHJ solar cells. In this thesis, the main objectives were to obtain enhanced surface passivation resulting higher V_{OC} values and to introduce a novel approach to IBC concept which is called *the wet chemical etching method*.

In GÜNAM, the effect of wet chemical cleaning methods on the solar cell parameters was investigated and 13.8% relatively efficiency gain was attained by only getting clean surface on SHJ solar cells. The pyramid rounding process was optimized in terms of optical loss and electrical improvements. The optimized rounding process was inserted to standard fabrication sequence of SHJ solar cell with exceeding 10.6% efficiency. The impact of Hydrogen termination before deposition of a-Si:H layer were studied and optimized. The highest efficiency obtained by SHJ

type solar cells (without i a-Si:H layer) is 11.84% under optimized surface preparation techniques.

For standard SHJ solar cells, the key point behind the excellent surface passivation is based on the nature of a-Si:H, which has the opportunity to obtain high V_{OC} values by passivation of dangling bonds by Hydrogen atoms. From this point of view, the deposition parameters of intrinsic a-Si:H were optimized and 11.0% efficient SHJ solar cell was fabricated. The effect of post-annealing treatment was studied both on AZO layer and on solar cell. It is concluded that the critical annealing temperature is 220°C and above that temperature, conductivity of AZO decreases significantly. After optimization of post-annealing and I a-Si:H deposition conditions, the highest efficiency in GÜNAM was recorded as 12.48% efficiency on 4 cm^2 cell area and 15.84% efficiency on 0.9 cm^2 cell area with 544mV V_{OC}, 32.87mA/cm^2 J_{SC} and 68.08% FF. After the study conducted in this thesis, the design of i chamber was upgraded and plasma box was inserted to chamber. After renovation of the chamber, the experiments conducted on the passivation quality showed that the record effective lifetime value is exceeding 3.2ms with 7nm i a-Si:H depositions on both side of FZ n-type Si wafers.

In Imec i^2 module group, the passivation quality of i a-Si:H/SiN_X stack layer was studied for the purpose of SHJ IBC solar cell front side coating. The highest effective lifetime obtained by i a-Si:H/SiN_X is 7.05ms. The ageing study was conducted on i a-Si:H/SiN_X stack layer. Besides the higher passivation quality of of i a-Si:H/SiN_X stack, it showed quite stable behavior in ageing study in terms of effective lifetime. The highest effective lifetime obtained by ageing 45 days in cleanroom atmosphere is 5.5ms. For the formation of junction on the rear side, wet chemical etchants were compared with respect to passivation quality of etched areas. Moreover, the wet chemical etching method by BOE: H_2O_2 was introduced with giving relatively high surface passivation on the rear side of solar cell The BOE: H_2O_2 etchant was optimized in terms of re-passivation quality resulting 4.3ms effective lifetime by deposition of i/n+ a-Si:H on both side. After optimization, the etching method was augmented to SHJ IBC solar cell fabrication. The SHJ IBC solar cells were fabricated

with the introduced etching technique on $4cm^2$ and 18% efficiency, 701mV V_{OC}, $35.8mA/cm^2$ J_{SC} and 72.0% FF was achieved without any surface texturing.

REFERENCES

[1] *World energy outlook 2015*. (2015). Paris: Organization for Economic Co-operation and Development (OECD/IEA).

[2] *World energy outlook 2009*. (2009). Paris: Organisation for Economic Co-operation and Development.

[3] *The End Of Fossil Fuels.* (n.d.). Retrieved December 19, 2016.

[4] Dempsey, J., & Ewing, J. (2011). Germany, in Reversal, Will Close Nuclear Plants by 2022. Retrieved December 19, 2016

[5] Chaisson, E., & McMillan, S. (2008). *Astronomy today*. (6th ed.). San Francisco: Pearson Addison-Wesley

[6] Nelson, J. *The physics of solar cells*. London: Imperial College Press. 2003.

[7] Sah, C. *Fundamentals of Solid State Electronics. Fundamentals of Solid State Electronics*. 1991

[8] Chapin, D. M., Fuller, C. S., & Pearson, G. L. (1954). A New Silicon p-n Junction Photocell for Converting Solar Radiation into Electrical Power. Journal of Applied Physics, 25(5)

[9] "*Fraunhofer ISE Photovoltaics Report*," 2016.

[10] National Renewable Energy Laboratory (NREL) Home Page. (n.d.). Retrieved December 19, 2016, from http://www.nrel.gov

[11] Bloomberg new energy finance & pv.energytrend.com

[12] Monga, Tanmay. *Development of Thin Heterojunction Solar Cells with High Open Circuit Voltage*. Thesis, 2015.

[13] R.E. Bird, R.L. Hulstrom, L.J. Lewis, *Terrestrial solar spectral data sets, Solar Energy*, Volume 30, Issue 6, 1983, Pages 563-573

[14] Luque, A., & Steven, H. *Handbook of photovoltaic science and engineering*. (2nd ed.). A John Wiley and Sons, 2011.

[15] Okuda, K., Okamoto, H., & Hamakawa, Y. Amorphous Si/Polycrystalline Si Stacked Solar Cell Having More Than 12% Conversion Efficiency. *Japanese Journal of Applied Physics,22*(Part 2, No. 9), 1983.

[16] Hamakawa, Y. New types of high efficiency solar cells based on a-Si. *Applied Physics Letters,43*(7), 644, 1983.

[17] De Nicholas, S. M. *A-Si:H/c-Si heterojunction solar cells: back side assessment and improvement*. Thesis, 2015.

[18] Taguchi. M., Yano, A., Tohoda, S., Matsuyama, K., Nakamura, Y., Nishiwaki, T., Maruyama, E. (n.d.). "*24.7% Record Efficiency HIT Solar Cell on Thin Silicon Wafer*." IEEE Journal of Photovoltaics, 1-4.

[19] Taguchi, M., Yano, A., Tohoda, S., Matsuyama, K., Nakamura, Y., Nishiwaki, T., Maruyama, E. 24.7%; Record Efficiency HIT Solar Cell on Thin Silicon Wafer. *IEEE Journal of Photovoltaics,4*(1), 96-99, 2014.

[20] World's Highest Conversion Efficiency of 26.33% Achieved in a Crystalline Silicon Solar Cell. (n.d.). Retrieved December 19, 2016, from http://www.nedo.go.jp/english/news/AA5en_100109.html

[21] Wolf, S. D., Descoeudres, A., Holman, Z. C., & Ballif, C., *High-efficiency Silicon Heterojunction Solar Cells: A Review*. Green,2(1), 2012.

[22] Hattori, Takeshi. *Ultraclean Surface Processing of Silicon Wafers: Secrets of VLSI Manufacturing*. Berlin: Springer, 1998

[23] Kern, Werner. "*The Evolution of Silicon Wafer Cleaning Technology*." Journal of The Electrochemical Society 137.6,1990.

[24] Kern W. & Puotinen D A. *Cleaning solutions based on hydrogen peroxide for use in silicon semiconductor technology*. RCA Rev. 31:187-206, 1970

[25] Reinhardt, Karen A., and Werner Kern. *Handbook of Silicon Wafer Cleaning Technology*. Norwich, NY: William Andrew, 2008

[26] C. Solar and C. C. Limits, "Solar cell conversion-efficiency limits 5.1," pp. 1–12.

[27] S. M. Iftiquar, Y. Lee, M. Ju, N. Balaji, and S. K. Dhungel, "Fabrication of Crystalline Silicon Solar Cell with Emitter Diffusion , SiNx Surface Passivation and Screen Printing of Electrode," 2005.

[28] S.R. Chitre, Proceedings of the 13th IEEE International Photovoltaic Specialists Conference, Washington D. C., 1978, pp. 152–154

[29] Stegemann, Bert, Jan Kegel, Mathias Mews, Erhard Conrad, Lars Korte, Uta Stürzebecher, and Heike Angermann. "Passivation of Textured Silicon Wafers:Influence of Pyramid Size Distribution, A-Si:H Deposition Temperature, and Post-treatment." Energy Procedia 38 (2013): 881-89. Web.

[30]Angermann, H.; Rappich, J. Wet-Chemical Conditioning of Silicon Substrates for a-Si:H/c-Si Heterojunctions. In: van Sark W, Korte L, Roca F. [Eds.]: Physics and Technology of Amorphous-Crystalline Heterostructure Silicon Solar Cells. Berlin: Springer, 2011 (Engineering Materials). p. 45-94

[31]Mcintosh, Keith R., and Luke P. Johnson. "Recombination at Textured Silicon Surfaces Passivated with Silicon Dioxide." Journal of Applied Physics 105.12 (2009): 124520.

[32] M. J. Kerr, J. Schmidt, A. Cuevas, and J. H. Bultman, J. Appl. Phys. 89, 3821, 2001.

[33] Gerischer, H.; Allongue, P.; Costa Kieling, V. The Mechanism of the Anodic Oxidation of Silicon in Acidic Fluoride Solutions Revisited. Ber. Bunsen-Ges. 1993, 97, 753−757

[34]Song, Guanghua. Method for cleaning textured silicon wafer. Sunpreme, LTD., Sunvaley, CA (US), assignee. Patent US2013/0252427A1. 26 Sept. 2013.

[35] Meerwijk, Joost. Analysis of Electronic Transport in HIT Solar Cells. Thesis. Netherland, Delft University of Technology, 2012.

[36] Moreno, M., Domínguez, M., Ambrosio, R., Torres, A., Torres, A., Rosales, P., & Itzmoyotl, A. Amorphous, Polymorphous, and Microcrystalline Silicon Thin Films Deposited by Plasma at Low Temperatures. Crystalline and Non-crystalline Solids, 2016.

[37] Cho, Y., Hsu, C., Lien, S., Wuu, D., & Hsieh, I. (2013). Effect of Hydrogen Content in Intrinsic a-Si:H on Performances of Heterojunction Solar Cells. International Journal of Photoenergy,2013, 1-6.

[38] Mews, M., Schulze, T. F., Mingirulli, N., & Korte, L. (2013). Hydrogen plasma treatments for passivation of amorphous-crystalline silicon-heterojunctions on surfaces promoting epitaxy. Applied Physics Letters,102(12), 122106.

[39] Horowitz, G. (2015). Validity of the concept of band edge in organic semiconductors. *Journal of Applied Physics,118*(11), 115502.

[40] Mönch, W., *Semiconductor surfaces and interfaces*. 3rd ed. Springer Series on Surface Science Vol. 26. 2001, Berlin: Springer. 548

[41] Pysch, D. (2011). *Assembly and analysis of alternative emitter systems for silicon solar cells*. München: Verl. Dr. Hut.

[42] Cameron, D. (n.d.). Plasma enhanced chemical vapour deposition of thin carbon films. Retrieved December 19, 2016.

[43] Stanley, Mishael Ebere. Impact of Emitter Dopant Gradient on Amorphous/Crystalline Silicon HIT Cell Performance. Thesis. Técnico Lisboa, 2014.

[44] Çiftpınar, Hande. Elective Emitter Formation Via Single Step Doping Through Laser Patterned Mask Oxide Layer For Monocrystalline Silicon Solar Cells. Thesis. Turkey, Middle East Technical University, 2014

[45] Street, R. A. Hydrogenated Amorphous Silicon. Cambridge: Cambridge UP, 1991.

[46] Street, R. A. (1982). Doping and the Fermi Energy in Amorphous Silicon. Physical Review Letters,49(16), 1187-1190.

[47] Vanecek, M., Kocka, J., Stuchlik, J., Kozisek, Z., Stika, O., & Triska, A. (1983). Density of the gap states in undoped and doped glow discharge a-Si:H. Solar Energy Materials,8(4), 411-423.

[48] Staebler, D. L., & Wronski, C. R. (1977). Reversible conductivity changes in discharge-produced amorphous Si. *Applied Physics Letters,31*(4), 292.

[49] Sze, S. M. Physics of Semiconductor Devices. New York: Wiley-Interscience, 1969

[50] Colinge, Jean-Pierre, and C. A. Colinge. Physics of Semiconductor Devices. Boston: Kluwer Academic, 2002.

[51] A. Descoeudres , Z. Holman , L. Barraud , S. Morel , S. De Wolf and C. Ballif ">21% efficient silicon heterojunction solar cells on n- and p-type wafers compared", IEEE J. Photovoltaics, vol. 3, no. 1, pp.83 -89 2013.

[52] A. I. Hertanto. "Back Amorphous-Crystalline Silicon Heterojunction Photovoltaics Fabrication Methodology". Thesis. 2010.

[53] Haller, I. (n.d.). Selective Wet and Dry Etching of Hydrogenated Amorphous Silicon and Related Materials. Journal of The Electrochemical Society J. Electrochem. Soc., 2042-2042.

[54] Bearda, T., Sivaramakrishnan Radhakrishnan, H., Granata, S., Van Nieuwenhuysen, K., Govaerts, J., Depauw, V., Dönerçark, E., Sharlandziev, I., & Choulat, P. (2015, January). Process development for heterojunction IBC cells on thin silicon foils bonded to glass. In European PV Solar Energy Conference-EUPVSEC.

[55] Gondek, Christoph, Marcus Lippold, Ingo RÃ¶ver, Klaus Bohmhammel, and Edwin Kroke. "Etching Silicon with HF-H2O2-Based Mixtures: Reactivity Studies and Surface Investigations." The Journal of Physical Chemistry C 118.4 (2014): 2044-051.

[56] Eom, Dae-Hong, Ky-Sub Kim, and Jin-Goo Park. "Passivation and Etching of Wafer Surfaces in HFâ□“H 2 O 2 â□“IPA Solutions." Japanese Journal of Applied Physics 41.Part 1, No. 10 (2002): 5881-886.

[57] O'Sullivan, Barry. Method for Fabricating Heterojunction Interdigitated Back Contact Photovoltaic Cells. Imec Vzw, assignee. Patent US9337380 B2. 10 May 2016.

[58] Özkol, Engin.Modeling and Optimization of PECVD Processes and Equipment Used for Manufacturing Thin Film Photovoltaic Devices. Thesis. Turkey, Middle East Technical University, 2015.

[59] Hilali, M. M. (2005). Understanding and Development of Manufactural Screenprinted Contacts on High Sheet-Resistance Emitters for Low-Cost Silicon Solar Cells. USA / Georgia University.

[60] M. Meuris, S. Arnauts, I. Cornelissen, K. Kenis, M. Lux, S. DeGendt, P. Mertens, I. Teerlinck, R. Vos, L. Loewenstein, M. Heyns, and K. Wolke, “Implementation of the IMEC-clean in advanced CMOS manufacturing,” in 1999 IEEE International Symposium on Semiconductor Manufacturing Conference Proceedings, pp. 157–160, 1999.

[61] AK 1000 inline | Meyer Burger technology AG.” http://www.meyerburger.com, accessed on 11/08/2014.

[62] “System 100 pro cluster/ cassette tool.” http://www.oxfordplasma.de/systems/100clus.htm, accessed on 09/08/2014.

[63] R. A. Sinton, A. Cuevas, and M. Stuckings, “Quasi-steady-state photoconductance, a new method for solar cell material and device characterization,” pp. 457–460, 1996. 10.1109/PVSC.1996.564042.

[64] T. Trupke, R. A. Bardos, M. C. Schubert, and W. Warta, “Photoluminescence imaging of silicon wafers,” Applied Physics Letters, vol. 89, p. 044107, July 2006

[65] H. Angermann, W. Henrion, M. Rebien and A. Röseler, Wetchemical preparation and spectroscopic characterization of Si interfaces, Appl. Surf. Sci. 235, p. 322-339 (2004)

[66] S. G. Kwon, W. Y. Jeong and J. H. Wang, No damage and high selective cleaning technology for very large scale integrated circuit, ITFIND, p. 1-33 (2004).

[67] Wolf, S. D., & Kondo, M. (2007). Abruptness of a-Si:H⁄c-Si interface revealed by carrier lifetime measurements. Applied Physics Letters,90(4).

[68] Kong, H., Yang, P., & Chu, J. (2011). Processing Parameters and Property of AZO Thin Film Prepared by Magnetron Sputtering. Journal of Physics: Conference Series,276.

APPENDIX A

BAND DIAGRAM

SHJ solar cells could be also formed on p type c-Si substrate with matching materials with different band gaps as illustrated in Figure 78.

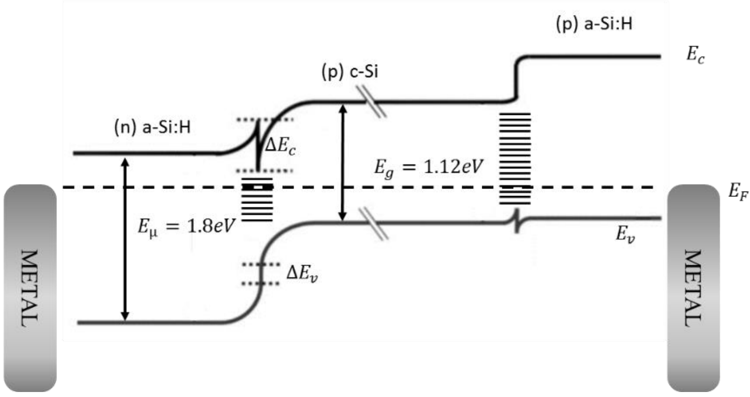

Figure 78: Band diagram for SHJ solar cell on p type c-Si substrate

The barrier formed for the holes at a-Si:H (n region) and c-Si interface with the height of ΔE_C is called as spike. Electrons are accumulated at the spike and drifted either by tunneling through the barrier via trap-assisted tunneling or by thermionic emission. Furthermore, secondary barrier is formed for holes at the valance band of other interface.